On the Design of a Low Cost High Performance Traction Motor with Ferrite Magnets

Mohammad Kimiabeigi

A thesis submitted for the degree of
Doctor of Philosophy

School of Electrical and Electronic Engineering

Abstract

Permanent magnet motors with rare earth magnets are amongst the best candidates for high performance applications such as automotive. However, due to their cost and risks relating to security of supply, alternative solutions such as ferrite magnets have recently become popular. In this thesis the two major design challenges of using ferrite magnets for a high torque density and high speed application, namely their low remanent flux density and low coercivity, are addressed. It is shown that a spoke type design may overcome the torque density challenge due to a simultaneous flux concentration and reluctance torque possibility. Furthermore, the demagnetization challenge can be overcome through careful optimization of the rotor structure, with the inclusion of non-magnetic voids on the top and bottom of the magnets. To meet the challenges of the high speed operation an extensive rotor structural analysis has been undertaken, during which electro-magnetic as well as manufacturing tolerances are taken into account.

In this thesis, the impact of the motor stack length and level of magnetic saturation on the demagnetization risk are studied based on 3-Dimensional Finite Element (3D FE) simulations and a proposed lumped circuit model. It is shown that reducing the stack length can significantly enhance the demagnetization resistance, with the effect being more pronounced for designs with a higher level of magnetic saturation. To benchmark the practicality of the concept, a previously presented high performance ferrite based design is modified by using a 30% weaker grade of ferrite magnet whilst shortening the stack length. It is shown that the demagnetization withstand capability of the design was significantly enhanced and exceeded the short circuit requirement with a good safety margin.

The fir tree based spoke type rotor comprises of two sections: a) the ferromagnetic rotor pole to provide the path for the magnetic flux, and b) the non-magnetic rotor support to provide the structural integrity. In this thesis, the Multiphysics and cost implications of the rotor support material, as part of a high performance ferrite magnet traction motor, are analysed, and an optimal selection with respect to those criteria is proposed. The performance of the design based on the proposed rotor support material is validated by electromagnetic and structural testing of three sets of customized prototypes. Based on the analysis, the proposed rotor support material was shown to, significantly, boost the cost competitiveness of a low cost ferrite motor for a high volume production.

As an alternative design to the proposed fir tree based rotor, a magneto-structurally optimized single piece rotor topology targeting the same EV application requirements is designed and compared against the fir tree based rotor performance. It is shown that an optimally designed single piece rotor design can meet about 80% of the power density of a fir tree rotor design at the cost of ~3 percent lower efficiency. Furthermore, the single piece rotor design may have better demagnetization resistance during severe faults. With regards to the performance per manufacturing costs, it was discussed that the single piece rotor design may match the fir tree solution, and the competitiveness may boost for designs with less severe structural requirements such as those with lower top speed requirement.

With regards to the stator design, distributed and concentrated windings may have both advantages and disadvantages when considering manufacturing cost, slot fill factor, the contribution factor of reluctance torque and parasitic effects. Furthermore, the trend toward high speed operation of the traction motors may increase the AC loss effects in the windings, contributing to the motor deficiencies and risk of thermal failure. In this thesis, the performance of a high speed ferrite motor with a distributed and concentrated wound stator, and with regards to torque and power performance as well AC loss effects is assessed. The thermal capability of the windings under peak torque conditions and cyclic loading, as well as the intermittent and continuous performance of the full scale prototype design based on the proposed distributed aluminium wound stator is presented.

The theoretical findings have been supported by a series of electromagnetic, thermal and structural testing of a custom built small scale prototype as well as a final full size prototype. The electromagnetic torque and power density is evaluated based on static and full dynamic testing, while the demagnetization withstand capability has been validated using current injection method. The structural testing includes an over-speed rotor spinning at 18000 rpm, as well as a fatigue testing under numerous cyclic loading. The thermal test validations include the evaluation of the aluminium windings temperature rise under the peak load, the reliability assessment under the cyclic load variation, and, finally, an investigation of the intermittent and continuous electromagnetic performance as well as windings temperatures of a fully assembled prototype.

To conclude, a comparison of the proposed ferrite traction motor against the industrially available state of the arts is provided, based on which the merits of the PhD thesis findings and the competitiveness of the disclosed design in terms of the performance per cost is highlighted.

<u>Acknowledgment</u>

TABLE OF CONTENTS

Chapter 1 : INTRODUCTION

Combustion engine cars emit pollution, endangering the environment while fossil fuel abundance is limited which influence the price as well as political matters [1, 2]. As a result, more environmentally friendly methods of energy harvest and/or energy conversion have been the topic of industrial research for some time [1-5]. On the energy conversion side, an electric motor has an efficiency of above 90% in comparison to the conventional combustion engines with typical efficiency range of below 30%, which alone indicate the advantages of moving towards electric cars.

There are different topologies of electric motors [6]: Permanent magnet (PM) based, [7], Induction based Motors (IM), [8], and Reluctance based Motors (RM), [9, 10]. Furthermore, there are different schemes to drive an electric motor most suitably according to the application requirement and the motor physics [11-14]. The history of motor design dates back more than a century, intelligent drives to few decades [15], and use of intelligent drives in automotive application is hardly more than two decades, where only in the last ten years large companies have been investing heavily on developing advanced electric propulsion systems in their cars [16, 17, 18].

The competiveness of a fully electric vehicle, apart from all its structural designs which is in common with a conventional non-electric car, is in the performance and cost of the embedded electric propulsion unit, [19], which includes: Battery, Drive, and Motor, while mechanical transmission may also be significantly adapted for a more optimal system performance and cost. This is the area where the focus of research has been placed in different research centres and universities around the world, aiming to understand the state of the art and build higher performance materials, [20, 21], system and component topologies, [22, 23, 24], and more efficient drives/ power management, [25, 26].

This PhD is based on a project with collaboration from Tier 1 automotive industry **[Funded by Innovate UK/ Evoque-E under Grant 110130]** to achieve the objectives described above, with specific attention paid to the multi-physical design of the electric motor. The technical side of this project faces and replies to the following challenges:

➢ Rare-earth magnets provide excellent contribution to high performance, however they form the biggest share of the motor price, with also a volatile price, and supply concentration mainly in China, [27, 28]. As a result in this thesis, a traction motor using

alternative permanent magnet material, namely ferrite magnets, will be designed and evaluated.

➢ The Ferrite based motors have rarely been applied or profoundly studied for automotive application, [17], thereby form a challenging and novel research topic.

The challenge of designing with rare-earth magnets is to obtain a multi-physically optimal topology with minimal magnets volume which can cope with the strict requirements such as:

- A compact/ high torque density design which can deliver the demanding torque in a small available volume [29].

- Magnets with suitable ingredients/grades [27], shapes, topologies [23], alongside with other design provisions, such as innovative winding layouts [30], to withstand against demagnetization at high temperature, field weakening operation and during short circuit faults, the conditions which naturally occur in an automotive application.

- For a high speed design, in order to increase the power density and the top speed rating of the vehicle, a suitable retaining of the magnets and rotating parts is required [31], while this provision must not dilute the electromagnetic performance.

- Finally, the design needs to be thermally efficient under the continuous and transient operating cycles, [32].

With Ferrite based motors, most of the challenges associated with the rare-earth magnets hold and might be significantly pronounced, this due to the weaker magnetic characteristics, (remanent flux density and intrinsic coercivity) of these magnets compared to the former, [33,34].

➢ Despite their dominant use as the winding material, the copper is associated with heavy weight, high cost, and concerns for recyclability. In this thesis, the feasibility of using aluminium instead of copper is assessed. In this regard, some electromagnetic and thermal implications such as DC and AC losses will be addressed. Furthermore, the peak and continuous performance as well as the reliability of a full scale prototype motor based on aluminium windings will be tested.

Prototype construction and testing are undertaken for early assessments of some high risk design aspects such as demagnetization properties of Ferrite magnets, aluminium windings, and rotor structural integrity at high speeds. This phase creates a valuable opportunity to benchmark and validate the theoretical assumptions and discover and fix any unattended details with regards to selection of materials and manufacturing process.

1.1 Overview of the thesis

This thesis discusses the major design challenges involved with a ferrite and aluminium based electric motor for a fully electric traction application. With regards to the rotor, a promising configuration is first selected, chapter 3, which is based on the electromagnetic criteria such as capability to provide high airgap flux concentration, high saliency, resistance against demagnetization, as well as the structural robustness against centrifugal forces at high speed. Based on the selected topology, two sub-categories, the so-called fir tree, chapters 3, 4, and 5, and single piece rotor, chapter 6, configurations have been addressed with more details. On this basis, the electromagnetic characteristics such as torque and power density, demagnetization, efficiency map, as well as structural characteristics such as the stress distribution and fatigue limitations have been investigated. Furthermore, throughout the analyses, the considerations for a high volume manufacturing have been discussed and addressed. With regards to the stator and windings design, a detailed comparison of the distributed and concentrated winding topologies, as well as the implications of wires type and layout on the DC and AC joule losses have been studied, Chapter 7. Based on these analyses, the pros and cons of using aluminium wires, as well as its implication on the design performance have been discussed and clarified.

Following the above pattern, the chapters' layout is as follows:

Chapter 2 provides a literature review on the state of the art traction motor designs with rare earth and ferrite magnets, and addresses the design challenges associated with a low cost high performance ferrite based design for a traction application.

Chapter 3 addresses the challenges involved with a high performance ferrite magnet based design and explains the electromagnetic and structural design procedure of a proposed fir tree based spoke type rotor.

Chapter 4 provides an in depth analysis into 3-dimensional demagnetization behaviour of the fir tree based design, and explains the effects of the stack length and deviation between the 2-dimensional analysis and the 3-dimensional real life performance.

Chapter 5 provides a more detailed investigation of the rotor support material and manufacturing techniques as a detrimental factor in reducing the cost of the proposed fir tree based design in Chapter 3. On this basis, a multi-disciplinary comparison between the state of the art technology, copper beryllium, and the proposed austenitic steel material is provided.

Chapter 6 introduces an innovative single piece rotor configuration as an alternative to the fir tree design in previous chapters. On this basis, a comparison of the electromagnetic and structural performance of the two rotor designs, based on simulations and prototype measurements, is provided.

Chapter 7 addresses the stator and windings design associated with the ferrite motor in the previous chapters. A comparison of the concentrated and distributed winding options, as well as aluminium vs. copper (in terms of DC and AC loss) is provided.

Chapter 8 provides the prototype testing as a further means to validate the theoretical findings in the previous chapters. This includes a comprehensive range of electromagnetic (static and dynamic), structural (over speed and fatigue) and thermal (winding reliability and continuous operation) testing to evaluate the torque and power density as well as structural and thermal capability of the proposed ferrite motor designs.

Chapter 9 summarizes the achievements and conclusions of this thesis, and addresses the areas for future investigations.

1.2 Contribution to knowledge and published work

This thesis has contributed to the following theoretical and practical achievements:

1. A high performance low cost fir tree based ferrite motor has been, successfully designed. This design, overcomes the critical design challenges with poor grade ferrite magnets such as minimizing the demagnetization risk, achieving high torque and power densities, and providing structural strength for high speed operations. The disclosed design provides a similar peak power density as the Nissan leaf motor, with only one-third of the active material cost.

2. A novel single piece spoke type rotor has been designed, which outperforms the existing state of the arts, [35], with more than 60% active material cost saving.

3. The design in this thesis demonstrates a successful exploitation of aluminium windings as a viable and reliable alternative to copper windings. It is suggested that despite the higher losses, the aluminium may result in lighter and cheaper traction motors, while the performance may become more competitive for high speed application.

4. Both the fir tree and the single piece rotor designs in this thesis are, currently, under investigation for the use in the future Jaguar Land Rover electric vehicles.

This PhD thesis has led to the following patents and publications:

<u>Patents</u>

- "Single piece spoke type rotor for electric vehicle applications," by **M. Kimiabeigi**, R. Long, A. Michaelides, filed Jan 2016.

- "Rotor structural means for high speed ferrite traction motor," by **M. Kimiabeigi** and J. Widmer and filed Jan 2016.

<u>Journal papers</u>

- **M. Kimiabeigi**, J. D. Widmer, R. Long, Y. Gao, J. Goss, R. Martin, T. Lisle, J.M. Soler Vizan, A. Michaelides, and B. Mecrow, "High performance low cost electric motor for electric vehicles using ferrite magnets," IEEE Trans. Ind. Electron., vol. 63, no. 1, pp. 113-122, Jan. 2016.

- **M. Kimiabeigi**, J. D. Widmer, R. Long, Y. Gao, J. Goss, R. Martin, T. Lisle, J.M. Soler Vizan, A. Michaelides, and B. Mecrow, "On selection of rotor support material for a ferrite magnet spoke type traction motor," IEEE Trans. Ind. Applications., vol. 52, no. 3, pp 2224-2233, May/ June 2016.

- **M. Kimiabeigi**, J. D. Widmer, N. Baker, *et al*., "3D Modelling of Demagnetization and Utilization of Poorer Magnet Materials for EV/ HEV Applications," IEEE Trans. Energy. Convers, vol. 31, no. 3, pp. 981-992, April 2016.

- J. Widmer, R. Martin, and **M. Kimiabeigi**, "Electric vehicle Traction Motors without rare earth magnets," Sustainable Materials and Technologies (Elsevier), Feb 2015.

- **M. Kimiabeigi**, R. Long, J. D. Widmer, *et al*., "Comparative Assessment of Single Piece and Fir Tree Based Spoke Type Rotor Designs for Low Cost Electric Vehicle Application," IEEE Trans. Energy. Convers, Feb 2017, DOI: 10.1109/TEC.2017.2662579.

Peer reviewed conference papers

- **M. Kimiabeigi**, J. Widmer, R.S. Sheridan, R. Harris, A. Walton "Design of high performance traction motors using cheaper grade of materials", IET International Conference on Power Electronics, Machines and Drives (PEMD), 2016.

- **M. Kimiabeigi** and J. Widmer, "On the Winding Design of a High Performance Ferrite Motor for Traction Application", International Conference on Electrical Machines (ICEM), 2016.

International Exhibitions

- **M. Kimiabeigi**, J. Widmer, A. Michaelides, Low cost high performance ferrite motors with aluminium windings, Advanced E-Motor Technology-IQPC conference, Frankfurt 2015.

- **M. Kimiabeigi**, J. Widmer, A. Michaelides, Low cost high performance ferrite motors with aluminium windings, Future Powertrain Conference, Birmingham 2015.

- **M. Kimiabeigi**, J. Widmer, A. Michaelides, Evoque-E High Speed Ferrite Motor, LCV, Millbrook, 2015

- **M. Kimiabeigi**, J. Widmer, A. Michaelides, Academic Involvement in the Evoque-E Project, Innovate UK Global Conference, London 2015.

- **M. Kimiabeigi**, J. Widmer, A. Michaelides, Low cost high performance ferrite motors with aluminium windings, Advanced E-Motor Technology-IQPC conference, Berlin 2016.

In this chapter a summary of the state of the art rare earth and ferrite permanent magnet motors for traction, and the advantages and disadvantages associated with each design are discussed. On this basis, the major design criteria such as power density, demagnetization withstand capability, and efficiency as well as the design parameters influencing each, are identified. The findings in this chapter form the basis for designing a reliable ferrite motor that can meet the demanding criteria of a low cost - high performance traction application.

2.1 Traction motor design with rare earth magnets

Permanent magnet motors may provide higher power density than alternative motor solutions owing to the use of energy dense rare earth magnets. Hence, they are the most popular choice for high efficiency applications with limited packaging space, such as automotive [18], [36-38]. Amongst different topologies, the interior permanent magnet (IPM) type is preferred due to its resistance against demagnetization, and possibilities for flux focusing and reluctance torque; improving the torque density as well as increasing the constant power speed range (CPSR) [24], [39-42]. Different magnet topologies in the rotor may be selected for different requirements and performance, the most common options being: single layer V-shape as in Toyota Prius [36], double layer V-shape as in Chevrolet Spark [43], Triangular as in Lexus or Nissan leaf [44] and [38], PM assisted synchronous reluctance (PMASynR) as in BMW i3 [45], and recently spoke type as in [46].

Figure 2-1 shows the rotor topologies in the different Toyota EV traction versions. As shown, few rotor topologies ranging from horizontal to V-shape and later triangular shape buried magnets have been practiced. With regards to the stator, an 8 pole 48 slot configuration with single layer distributed winding has been applied to all models. A summary of the major design specificatuions as well as the output torque and power is given in Table 2-1.

The efficiency map of the Toyota 2010 model, combined motor and inverter, is shown in Figure 2-2, [36], where a peak efficiency in the vicinity of 95% has been achieved. Further details of the Toyota EV designs including the manufacturing aspects, controller and power electronics, and thermal assessments have been disclosed in [32], [47-49].

Figure 2-1: Rotor topology in different Toyota EV designs, [17], [36].

Table 2-1: Design specifications of different Toyota EV and HEV models, [17], [36].

	Peak Torque (Nm)	Base, Top RPM	Peak power (kW)	Active Mass* (kg)	Magnet mass(kg)	DC link voltage/ Peak AC Current (V, A)
Prius 2004	400	1200, 6000	50	34	1.2	650 V
Camry 2007	270	2500, 14000	70	24	0.9	650 V, 430 A
Lexus 2008	300	2000, 10000	110	27	1.4	650 V, 430 A
Prius 2010	207	2800, 13500	60	21	0.8	500 V, 250 A

*Active material includes stator and rotor laminations as well windings and magnets.
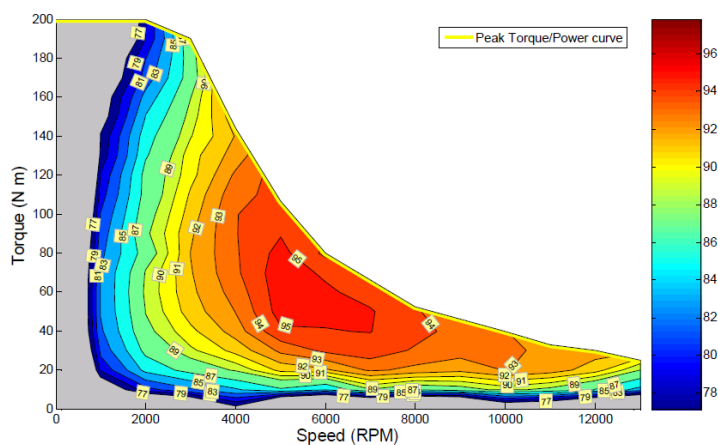
Figure 2-2: Prius 2010, Motor-Inverter combined efficiency, [36].

The Nissan leaf (2010) motor design topology and components are shown in Figure 2-3. The rotor has a triangular magnet topology similar to the Toyota Lexus 2008, likewise the stator

is based on a 48 slot- 8 pole configuration and a single layer distributed winding. The cooling system includes an aluminium die-cast frame, Figure 2-3(c). Some of the design specifications and the output torque and power are summarized in Table 2-2. An efficiency map including the losses in the motor, inverter and cables is reported in [38], Figure 2-4.

(a)
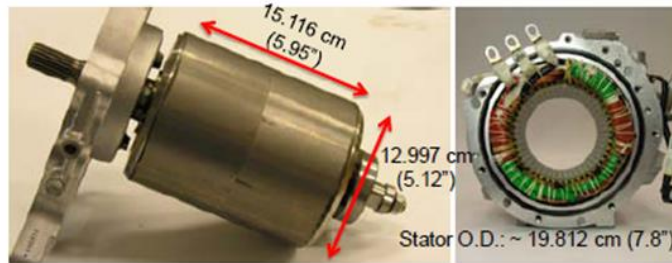
(b)
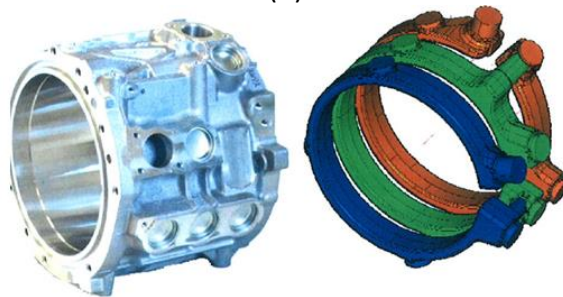
(c)

Figure 2-3: Nissan Leaf motor design schematics, a) stator, conductors, and rotor (left to right), b) rotor and wound stator (left to right), c) cooling frame and cooling channels (left to right), [38].

Table 2-2: Nissan leaf motor design specifications, [17].

	Peak Torque (Nm)	Base, Top RPM	Peak power (kW)	Poles, Slots	Active mass (kg)	Magnets mass (kg)	DC Link Voltage/ Peak AC Current (V, A)
Nissan leaf 2010	280	2730, 10390	80	8,48	30.4	2	403 V peak, 600 A peak (4 sec)
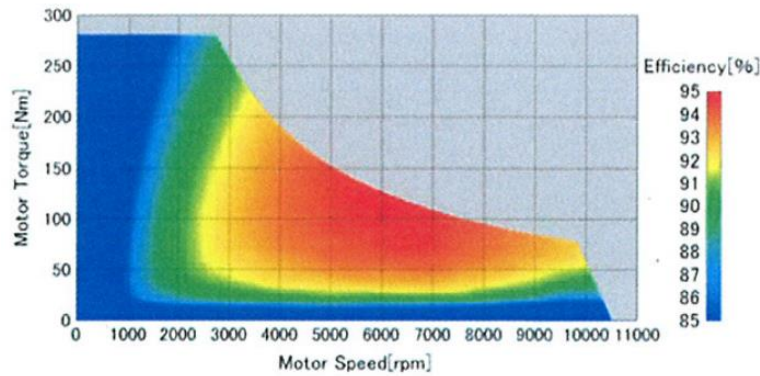
Figure 2-4: Efficiency map of the Leaf power train including motor, inverter and AC cables.
[38].

An exploded view of the 85 kW EV traction motor in the Chevrolet spark is shown in Figure 2-5, [50]. The rotor is consisted of 10 poles with double layer V-shape magnet topology, and the stator is comprised of 60 slots with a distributed hairpin winding lay out, Figure 2-5(b). The application of a hairpin winding may, significantly, enhance the thermal capability of the motor due to the lower DC resistance of the windings, as well as better thermal heat transfer coefficient (due to the less insulation between the wires); some of these improvements have been indicated in [50].

(a)   (b)
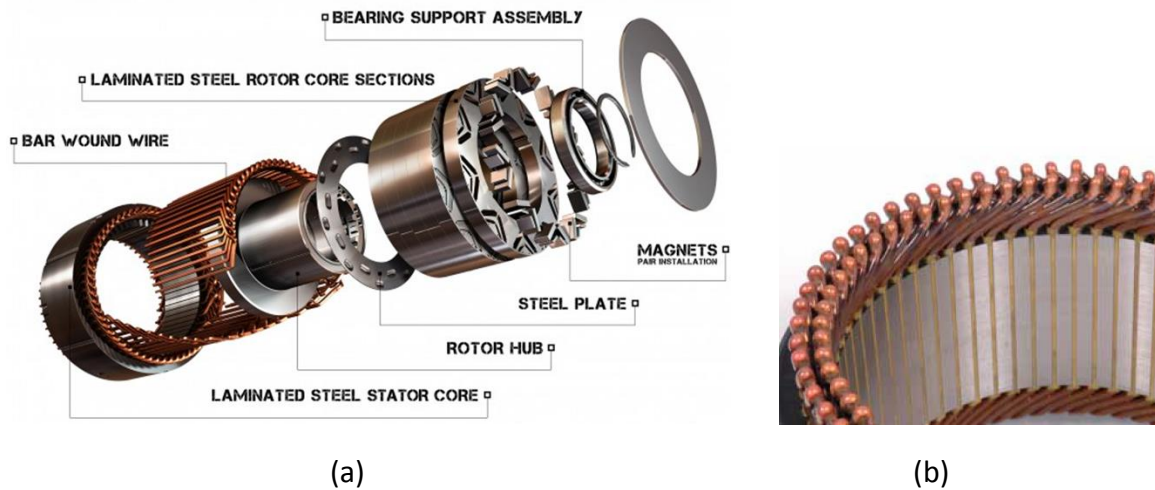
Figure 1: Chevrolet Spark, 2013, motor design components. (a) Exploded view. (b) Hairpin windings [50].

An illustrative picture of the 125 kW BMW i3 model traction motor rotor design is shown in Figure 2-6, [45], where the selected arrangement of the flux barriers is claimed to enhance the saliency and the power density of the motor.
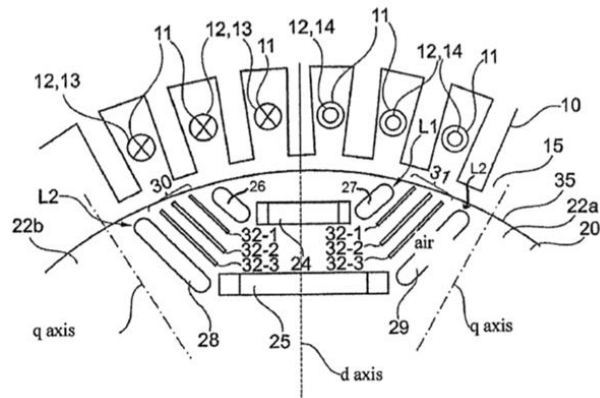
Figure 2-6: An illustration of BMW i3 traction motor rotor design [45].

Despite the high performance of the rare earth magnet based traction motors, the associated cost with these materials, in particular Neodymium (Nd) and Dysprosium (Dy) elements, is high and unstable, [27], [28], [51], Figure 2-7. Furthermore, as about 90% of the world resources are, currently, explored and mined in China, [27], there are some geopolitical motivations to research and apply alternative materials. To minimize the rare earth materials, approaches such as maximising the reluctance torque contribution in an IPM design, [42], using magnet-free designs such as induction, synchronous reluctance or switched reluctance motors, or designs with ferrite magnets can be employed. A detailed review of such techniques has been reported in [52].
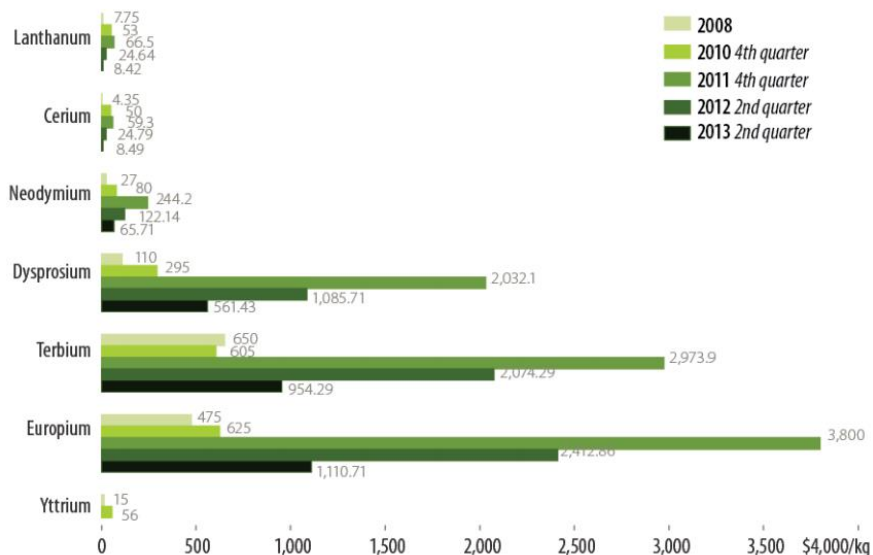
Figure 2-7: Rare Earth Oxide Prices, 2008-2013 (US $/kg), [51].

2.2 Traction motor designs with ferrite magnets

Despite their relatively poor magnetic characteristics, the Ferrite magnets have recently been studied for the high power density applications such as wind energy, [53] Figure 2-8(a), industrial motors, [54] Figure 2-8(b), as well as automotive. Some of the top grades suited to these applications have been summarized in Figure 2-9 [20]. In this section a summary of the traction motor deigns based on ferrite magnets and the associated design challenges is provided.

(a)   (b)
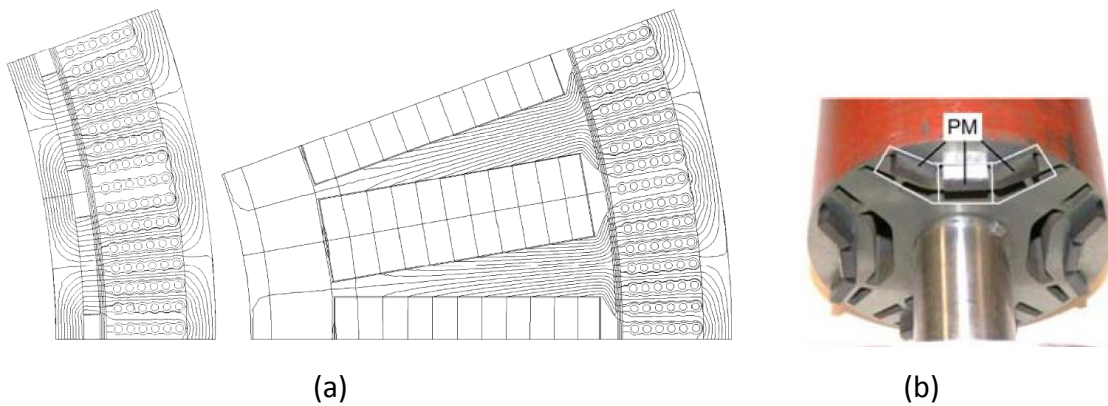
Fig 2-8: Examples of high performance ferrite based machines designs. a) Wind generator comparing NdFeB to ferrite based designs, [53]; b) A synchronous reluctance Ferrite assisted for industrial application [54].
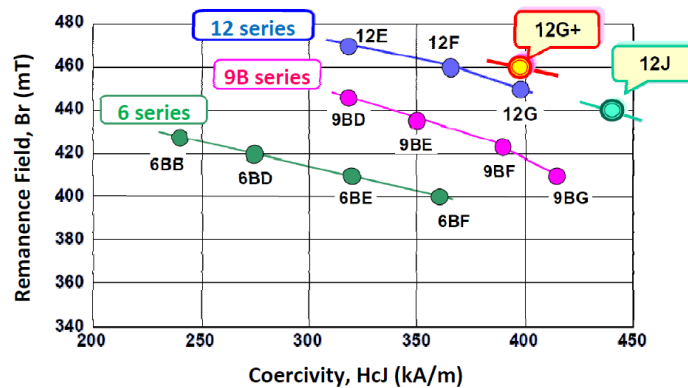
Figure 2-9 Comparison of different top grades of Ferrite magnets [20].

2.2.1 POWER DENSITY

Due to the relatively poor remnant flux density, B_r, of the ferrite magnets, the associated designs need to employ topologies with high flux concentration and/ or high degree of saliency to maximise the torque and power density. On this basis, most state of the art designs have employed an IPM rotor topology. In [40], Figure 2-10(a), a low speed, high

torque density, three layer, U-shape PMASynR topology benefited from both reluctance torque and flux concentration. In [55], Figure 2-10(b), a low speed, high torque density, three layer, V-shape PMASynR design was presented and compared against the Toyota Prius performance. In [23], a conceptual synchronous Ferrite-assisted reluctance motor, with 55 kW peak power and 14 krpm top speed has been studied, Figure 2-10(c). The demagnetization risk of this design was improved by increasing the pole number from 4 to 6. Another example of high torque density rotor topologies includes the LC shape [56], Figure 2-10(d), where an LC type design was demonstrated as a low cost alternative to an existing rare earth traction design with a similar torque density.

A viable rotor design to satisfy the high torque density requirement is the spoke magnet topology [34, 35], [57, 58]. In [34], Figure 2-11(a), a 55 kW and 14 krpm spoke type ferrite magnets with a distributed winding has been designed, and validated. In this design, a water cooling through the external frame in combination with the oil spray on the end coils is applied which contributed to an excellent continuous power capability. With regards to the structural design, the rotor is composed of two parts including the magnetic rotor poles which provide the magnetic path for the flux, and a non-magnetic rotor support, which provides the rotor integrity based on a fir-tree feature, [59]. In [35], Figure 2-11(b), a spoke-type ferrite rotor motor prototype for EV application with 60 kW and 11000 rpm top speed has been disclosed. The design is based on a 16 pole rotor and 9 phase concentrated coil in the stator, where the integrated inverter topology resulted in a compact and a high response design. With regards to the rotor structure, it benefits from a simple single piece rotor topology which consists of flux barriers to avoid excessive magnet leakage through the rotor yoke.

In [59], Figure 2-11(c), a 18 kW, 10 pole 12 slot spoke-type ferrite rotor with concentrated winding stator and top speed of 7 krpm, has been reported. Based on the invented rotor topology in this design, the saliency and, thus, the field weakening capability have been enhanced.

In [60], Figure 2-11(d), a 6 pole 9 slot ferrite based spoke type design is disclosed in which the airgap flux density is improved by applying the flux concentration concept and maximal allocation of Ferrite magnets into the available rotor space. The rotor is composed of a single piece structure, but the structural performance such as the peak stress levels has not been addressed by the authors. In [58], Figure 2-11(e), the effect of increasing the magnet layers in a spoke-V type topology on the torque density, and demagnetization has been studied.

Based on the analyses, a double layer lay out was found to combine high performance and low cost.

In [33], Figure 12(a), a direct drive in-wheel motor with an outer rotor topology is modified by replacing the NdFeB magnets by about 6 times larger ferrites for 26% increase of rotor diameter. The design, however, suffers some demagnetization risk in the field-weakening range. Another example of an external rotor with buried ferrite magnets is provided in [61], Figure 2-12(b) where due to the layered structure, the design benefits from a high saliency and constant power speed ratio (CPSR).

Few high torque density dual stator topologies and axial flux designs have been reported in [62], [63], Figure 2-13. In [62], Figure 2-13(a), a 60 kW dual stator topology was compared against the Toyota Prius 2010 HEV design in terms of torque density and efficiency, and was demonstrated as a low cost alternative. In [63], Figure 2-13(b), a similar design with a coreless rotor and a stator made of soft magnetic composite material (SMC) was studied and shown to surpass the Toyota Prius design in terms of performance per cost. However, both designs in [62] and [63] require further structural improvements to cope with the high speed requirements, i.e. circa 14,000 rpm.

(a)   (b)   (c)

(d)
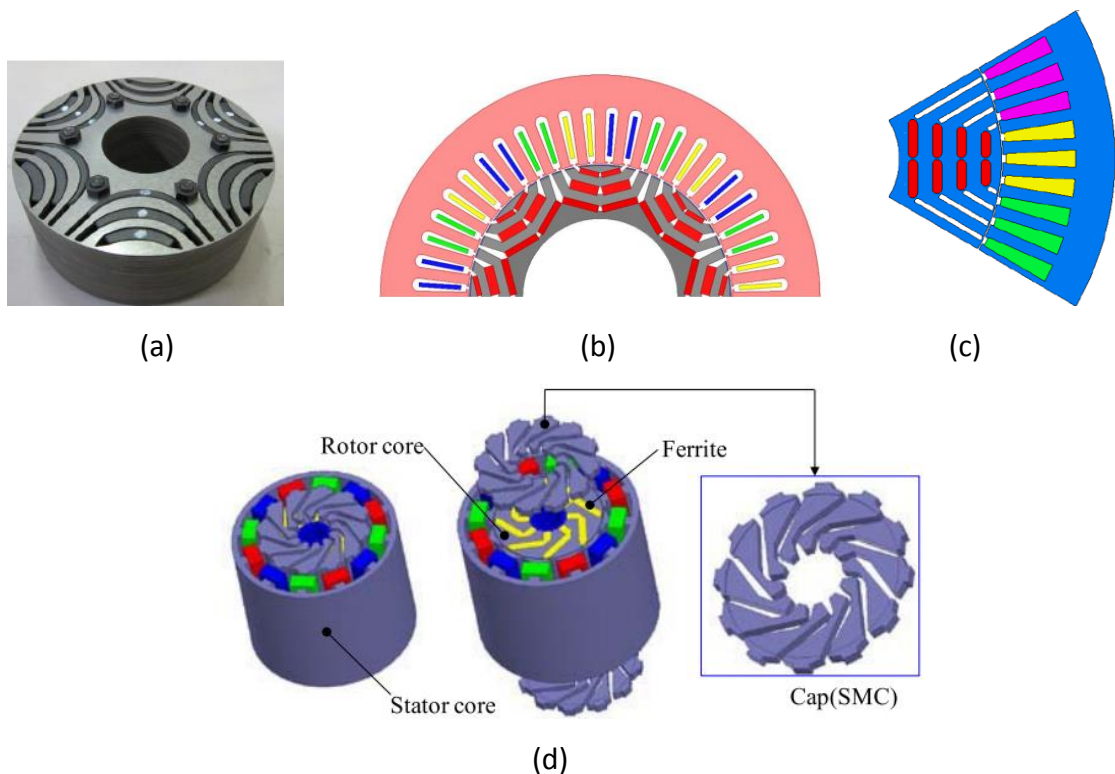
Figure 2-10: Examples of Ferrite-based IPM rotor topologies in the vehicle traction application. (a) U shape [40], (b) V shape [55], (c) U shape with horizontal magnets [23]. (d) LC shape [56].

(a)   (b)   (c)

(d)   (e)
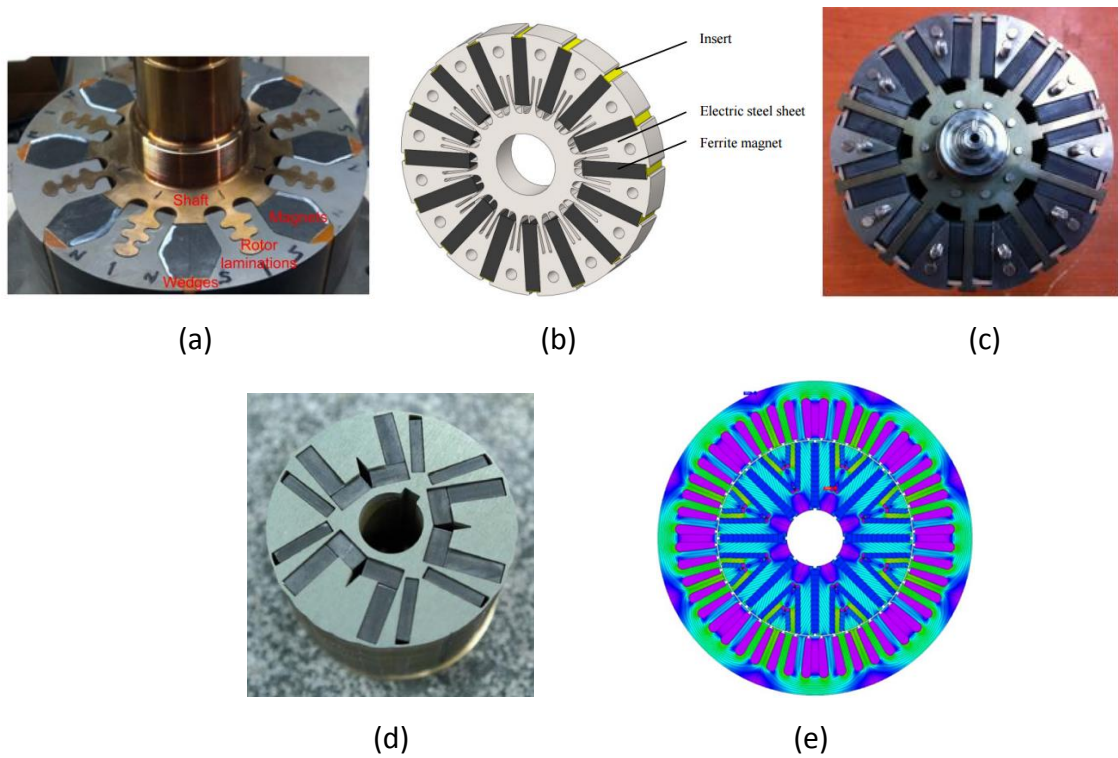
Figure 2-11: Ferrite spoke type rotors for the vehicle traction application. (a) Fir tree based rotor [34]. (b) Single piece rotor [35]. (c) Wing type spoke rotor [57], (d) Innovative high volume ferrite spoke [60]. (e) Multi-layer V shape and spoke [58].

(a)   (b)
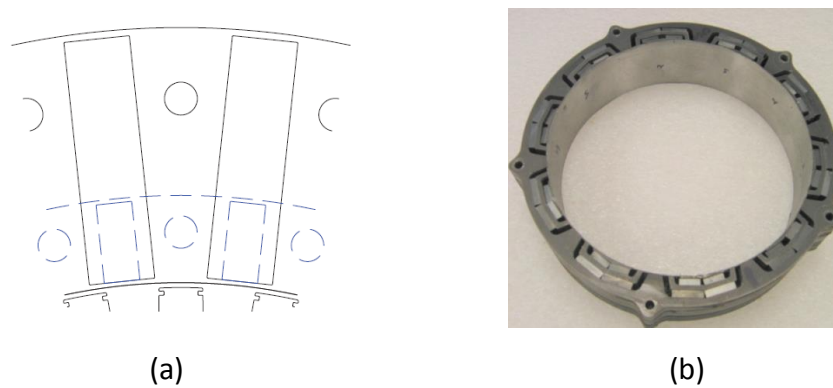
Figure 2-12: Examples of external rotor designs with ferrite magnets for in-wheel traction. (a) Comparison of larger volume of ferrite magnet replacing the NdfeB [33]. (b) An innovative two layer design with saliency [61].
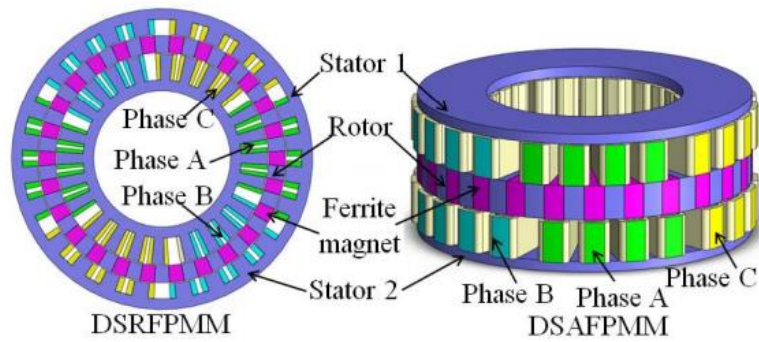
(a)
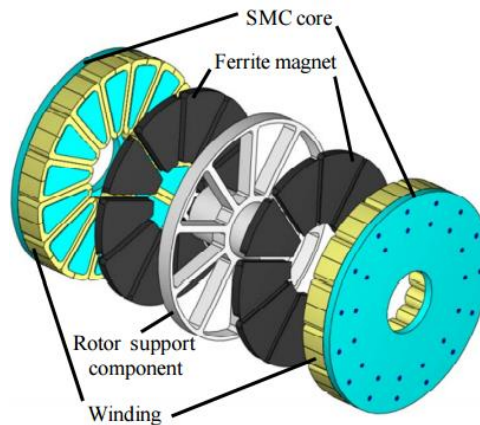
(b)

Figure 2-13: Innovative high torque density traction motor designs with ferrite magnets. (a) Dual stator topology [62]. (b) Axial flux motor with coreless rotor [63].

2.2.2 DEMAGNETIZATION

Due to the low coecivity of the ferrite magnets and, in particular, their susceptibility at lower temperatures, Figure 2-14, [64], they are vulnerable to the demagnetization risk during the field weakening and short-circuit conditions. To overcome this, different features of the rotor design need to be carefully considered. In [65], the effect of the temperature on different characteristics of the ferrite based traction motors, including the higher risk of demagnetization at lower temperatures has been demonstrated. In [40] the demagnetization withstand capability was enhanced by tapering the flux barriers toward the airgap and increasing the magnets thickness. In [66] it was shown that in a spoke type topology the embedding of the magnets into the rotor and allocating a top cavity on top of the magnets can mitigate the demagnetization risk. In [57] a similar concept has been employed in a novel radially-split magnet topology and the demagnetization was tested under the peak torque and 20˚ advance angle operation. In [34] the demagnetization was

studied at the maximum current and advance angle for the peak power operation and 105 ˚C magnet temperature, where the demagnetization risk was mitigated by reducing the number of turns as well as thickening the magnets. In [23] the demagnetization risk has been mitigated by reducing the ampere turns per pole via increasing the number of poles.

In case of the surface mounted magnet designs, the demagnetization risk might become higher due to the more exposure of the magnets to the armature reaction field, [67]. In these cases, the risk can be, partly, mitigated by a close temperature monitoring of the magnets as the risk is reduced at higher temperatures, Figure 2-15; alternatively, the stator leakage inductance can be enlarged by reducing the tooth tip ratio or using magnetic wedges.

Due to the complexity of the modelling, most of the papers have only studied the 2-dimensional (2D) demagnetization behaviour [68], [69], [40], [70], [71], [72], Figure 2-16. In this respect, some have used Finite Element models to identify and mitigate the demagnetization risk by optimization of the design topology [40], [71], whilst others have used fast analytical techniques to diagnose and prevent demagnetization during the motor operation, [68], [69], [70]. 3D FE studies have tended to focus on the end winding leakage calculations, for example [73], [74], and have provided accurate analytical expressions which may be incorporated into the 2D equivalent circuit of an electrical machine. Even though, several papers such as [73], [75], [76], analytically, or [77], numerically (using FE), have derived and described the impact of 3D parameters on the performance of electrical machines, their modelling is often limited to the derivations of the airgap flux density, BEMF and torque, while the 3D effect of the stack length variation on the demagnetization performance has not been, specifically, addressed.
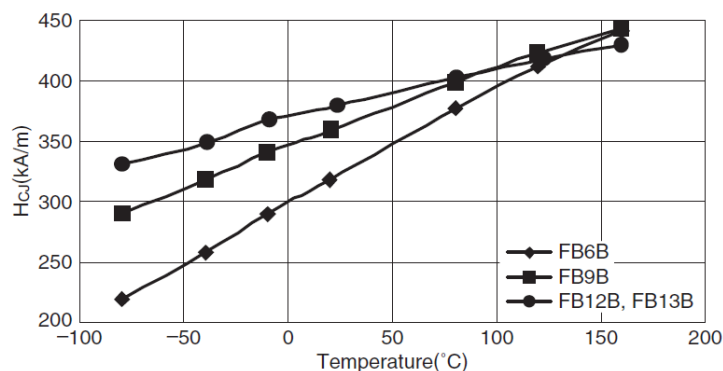
Figure 2-14: Coercivity and its temperature dependency for some typical high grade ferrite magnets, [64].

17
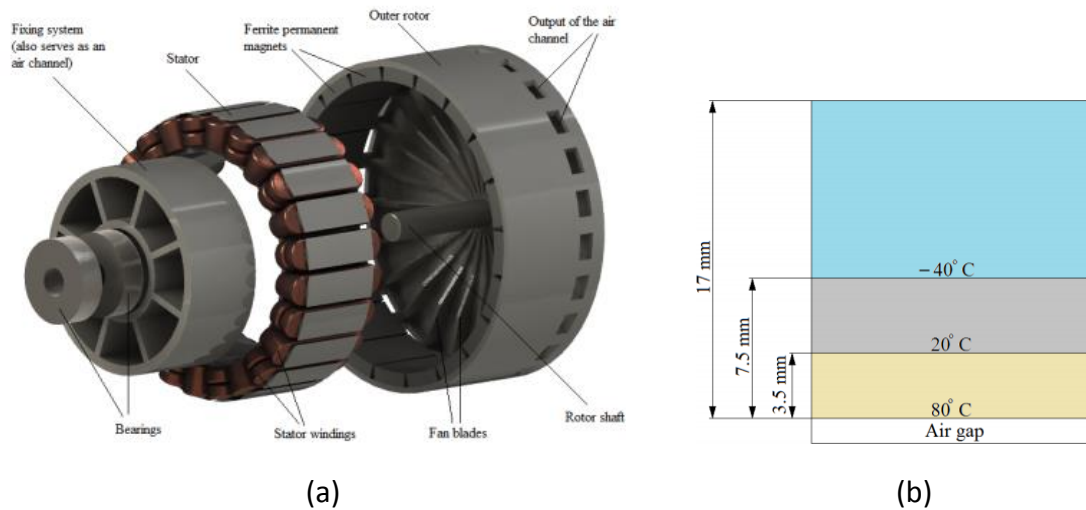
Figure 2-15: A 50 kW surface mounted ferrite design, and the required temperature levels in the magnets to avoid demagnetization [67]. (a) Topology. (b) Required temperature levels.
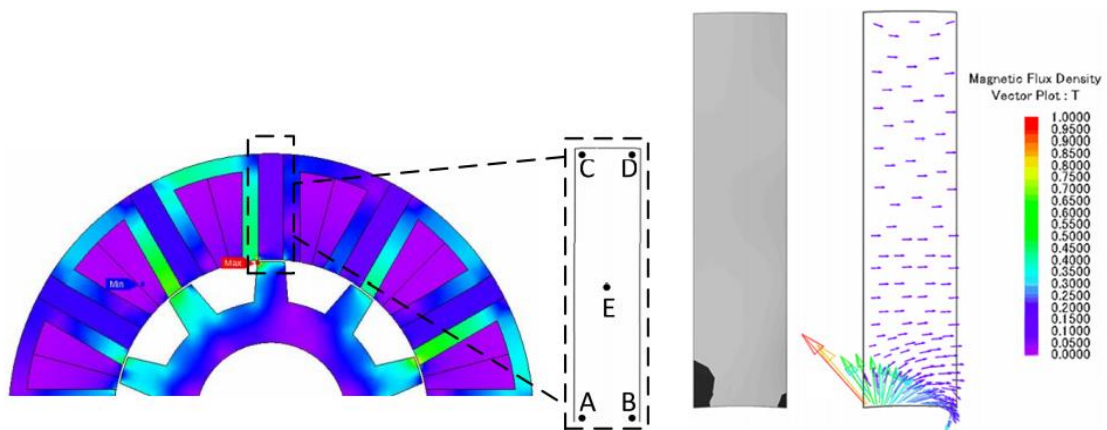
Figure 2-16: Illustration of a partial demagnetization in a flux switching ferrite based traction motor, [72].

2.3 Structural considerations with the high speed

Since the power is the product of the torque and speed, by increasing the speed one can reduce the torque requirement and, thereby, reduce the size of the motor. A high speed motor design approach can be, particularly, helpful in case of less power dense rare earth free motor types such as the traction motor designs with ferrite magnets.

On the other hand, one must consider the possibility of an additional transmission cost, as increasing the speed necessitates a higher ratio of the gearbox, coupling the motor to the vehicle wheels. Another challenge associated with a high speed motor design, is the rotor

bending at the critical speeds, [31], [78], some examples by ORNL, [79], are brought in Figure 2-17.
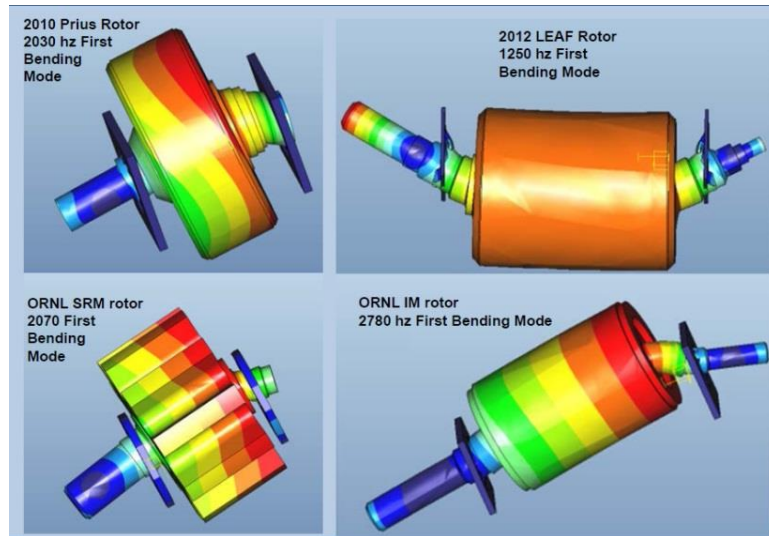
Figure 2-17: Illustration of critical speed bending at high speeds [79].

(a)   (b)
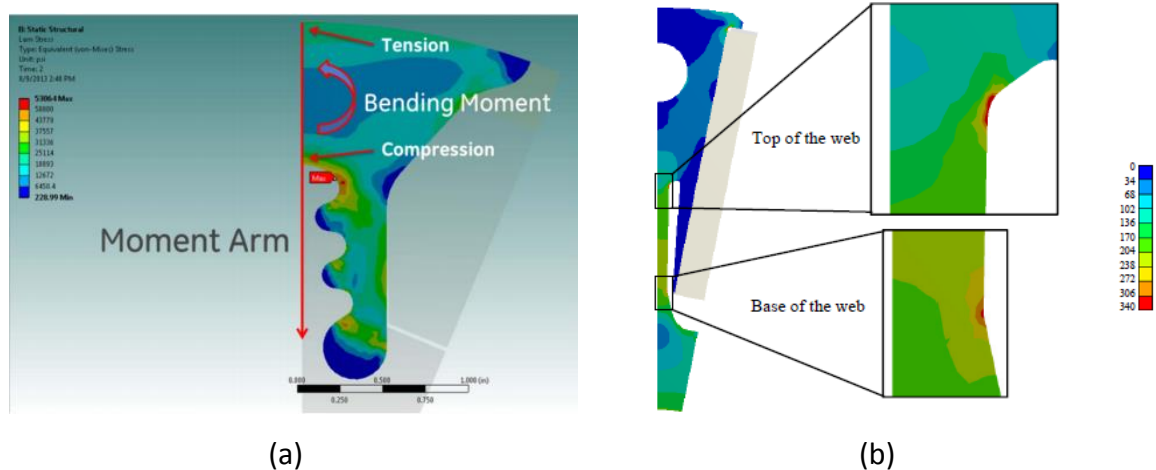
Figure 2-18: Illustration of the rotor peak stress distribution during high speed operation.
(a) Spoke type with fir tree design, 14,000 rpm top speed [34]. (b) Spoke type with single piece rotor, 11,000 rpm to speed [35].

Another limiting factor in designing high speed motors is to ensure that the stress due to the centrifugal forces does not exceed the yield strength of the selected rotor material, [34,35], [79-81].

With regards to the spoke type rotor topology, one configuration allows the rotor to be composed of two parts, Figure 2-11 (a): a) the rotor poles made of ferromagnetic laminations which provide the magnetic flux path, and b) the rotor support made of a non-

magnetic and sufficiently strong material which holds the rotor poles and provide the rotor integrity via a fir-tree feature. Another viable spoke type topology includes a rotor comprised of a single piece lamination stack, Figure 2-11 (b). In this configuration, the appropriate flux barriers must be designed to avoid an excessive permanent magnet flux leakage through the rotor yoke, as well as providing a sufficient structural integrity for the operation at high speeds. Figure 2-18, [34, 35], illustrates the distribution of the mechanical stress in the two examples of high speed spoke type ferrite traction motors, where the locations with the highest level of stress are indicated with red colour.

While the single piece rotor topology may be advantageous over the fir-tree based type in terms of the design simplicity and having fewer components, the latter may be preferred due to its superior performance both magnetically (due to less magnet leakage through the rotor yoke) and structurally, as a result of which higher power density and efficiency, as well as higher rotor top speeds may become achievable.

In the case of the fir tree based rotor design, a special attention must be paid to the rotor support material. In the existing state of the art [34], the rotor support is made of copper beryllium. Beryllium is an Alkaline earth metal with a high strength and a low mass density (only 1.85 times that of water) and results in excellent structural and formability of the associated alloys including copper beryllium, [82]-[85]. However, this element is, relatively, scarce in the earth crust, with the US accounting for about 65% of the resources and 90% of the global production in 2014, [83]. Furthermore, the mining and production of Beryllium alloys might be associated with some health and environmental hazards, [84], [85].

Although few designs based on both aforementioned spoke rotor topologies have been tried, no detailed investigation on the choice of the rotor support material in the fir tree topology, and no comparison of the two designs in terms of performance and cost have been reported to date.

Finally, the fatigue life of the rotor structure is determined based on the speed range variation and the number of operating cycles in that speed range. As a result, calculations and testing must ensure that the rotor will endure the entire life time of the vehicle with a safety margin included, [81].

2.4 Stator and windings

With regards to the stator and windings for a ferrite based traction motor, both

concentrated (CW), [35], [56], and distributed (DW), [34], [40], [55], [86], windings can be applied. On this basis, the concentrated option reduces the costs (due to the simplicity of the manufacturing and the possibility of having a modular stator, Figure 2-19, [36, 37], which often come at the cost of lower saliency and lower contribution of the reluctance torque. Furthermore, with a concentrated winding with a modular stator core, a greater slot fill factor can be achieved, as a result of which the DC winding loss is mitigated and the power density may be enhanced, [87], [88]. Several papers have compared the performance of concentrated and distributed windings applied to IPM motors, amongst which most have addressed the extra core and magnet losses as well as acoustic noise and vibration due to the additional Magneto Motive Force (MMF) harmonics associated with the concentrated windings, [87], [89], [90]. In [91]-[94], the torque-speed performance of a distributed winding is reported to be superior to that of a concentrated winding, in both constant torque and constant power regions, due to the higher saliency ratio.

Another important aspect of traction motors, especially those with high top speed rating, is to mitigate the AC loss in the windings. In [95], a one dimensional analytical model of the AC loss in a distributed winding has been proposed and proved with only 5% inaccuracy when compared against FE modelling. In [96], Figure 2-20, the proximity effect in several combinations of parallel and series wire connections and for a concentrated wound traction motor have been studied, and shown that without a transposition, [97], the losses in a bundle of parallel wires may concentrate in few individual wires, leading to hot spots and a possible motor failure. In [98], the extra time harmonics due to PWM switching were shown to pronounce the proximity and skin effect losses, while in [99], a computationally efficient method to calculate the skin and proximity losses which, also, account for the temperature effects has been proposed.

The choice between the star and delta connections for a three phase winding motor might result in some parasitic effects caused by the 3rd order flux harmonics. In [100], it is shown that in an induction motor (IM) the 3rd harmonic flux due to the magnetic saturation may result in extra core losses, while it is commented that the delta connection might affect these losses via cancelation of the 3rd order harmonics. Furthermore, several papers have investigated the drive advantages via switching between the star and delta connections, [101], [102], (due to the voltage per coil differences between the two connections). However, no paper has provided a comparison between the two winding schemes with regards to the AC losses.
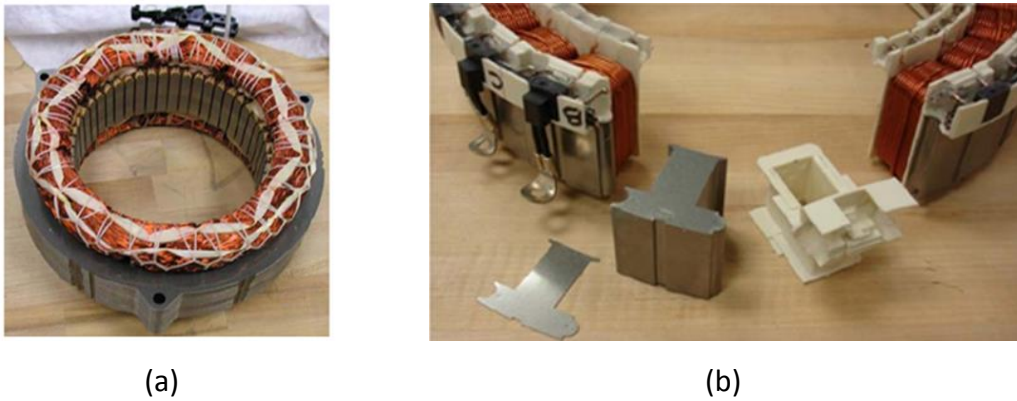
Figure 2-19: Comparison of a non-modular vs. modular stator. (a) Prius 2010 [36]. (b) Honda Accord 2005 [37].
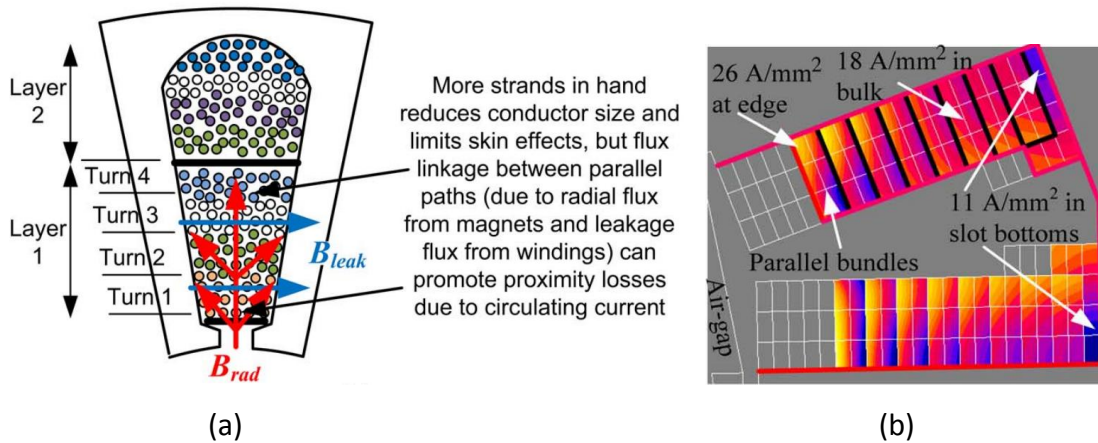
Figure 2-20: Illustration of AC winding losses, [96]. (a) Flux leakage in the slot. (b) Increased current densities due to proximity effects.

In terms of the winding material, copper is dominantly used and preferred to aluminium, mainly due to its higher electrical conductivity which may assist to achieve higher efficiencies and better continuous performance. However, few research studies, [103], [104], have suggested that aluminium wires may result in lighter and cheaper products, with the performance becoming more competitive, at higher frequencies. In [104], it is suggested that an electric motor with a compressed aluminium winding may achieve similar joule losses and power performance as a conventionally wound copper winding.

2.5 Conclusion

In this chapter, a review of the state of the art permanent magnet traction motors using rare earth magnets and, in particular, the low cost alternative ferrite magnets has been provided. The major challenges associated with the ferrite based designs, such as the power

22

density, the demagnetization withstand capability, an appropriate rotor structural design to stand the high centrifugal forces at high speed, and the winding AC losses have been addressed. On this basis, the viable topologies for a high performance low cost traction motor design with ferrite magnets and the existing gaps in the literature, such as a detailed study of the pros and cons associated with the spoke type rotor topologies and the relevance of the 3D demagnetization effects have been identified, which will be investigated in the following chapters.

Chapter 3 : HIGH PERFORMANCE FERRITE MOTOR DESIGN FOR TRACTION APPLICATIONS BASED ON A FIR TREE SPOKE TYPE ROTOR

3.1 INTRODUCTION

This chapter addresses and combines the major challenges involved with the design of a high performance ferrite based motor in a systematic way, including: the methods to achieve high power density, demagnetization withstand capability, and rotor integrity at high speeds. First the preference of the spoke type topology over the main alternative, the PMASynR U-shape and V-shape, is investigated. A spoke type design resulting from a multi-physics based optimization is then presented. The electromagnetic performance of this design, with a major focus on the demagnetization withstand capability and the associated key design parameters, is studied. Furthermore, the optimization of the structural design and the fir tree feature with an attention to the electromagnetic performance (i.e. the torque maximization and the demagnetization mitigation) as well as a low cost manufacturing is explained.

The structural analysis in this chapter has been done in collaboration with Tata Steel, UK, during which the design trends and the boundary conditions imposed by the electromagnetic analysis have been iterated with the structural finite element analysis using the Abaqus FEA.

The contents of this chapter have led to the following publications and exhibitions:

- **M. Kimiabeigi**, J. D. Widmer, R. Long, Y. Gao, J. Goss, R. Martin, T. Lisle, J.M. Soler Vizan, A. Michaelides, and B. Mecrow, "High performance low cost electric motor for electric vehicles using ferrite magnets," IEEE Trans. Ind. Electron., vol. 63, no. 1, pp. 113-122, Jan. 2016.
- J. Widmer, R. Martin, and **M. Kimiabeigi**, "Electric vehicle Traction Motors without rare earth magnets," Sustainable Materials and Technologies (Elsevier), Feb 2015.

- **M. Kimiabeigi**, J. Widmer, A. Michaelides, Low cost high performance ferrite motors with aluminium windings, Advanced E-Motor Technology-IQPC conference, Frankfurt 2015.

- **M. Kimiabeigi**, J. Widmer, A. Michaelides, Low cost high performance ferrite motors with aluminium windings, Future Powertrain Conference, Birmingham 2015.

- **M. Kimiabeigi**, J. Widmer, A. Michaelides, Evoque-E High Speed Ferrite Motor, LCV, Millbrook, 2015

▪ **M. Kimiabeigi**, J. Widmer, A. Michaelides, Academic Involvement in the Evoque-E Project, Innovate UK Global Conference, London 2015.

3.2 Design and Analysis

3.2.1 Packaging and Specification

The main requirements of the ferrite based electric motor, specified as part of an all-electric vehicle project, are summarized in Table 3-1. The available motor package including the shaft, housing and cooling is a cylinder with a volume of less than 14 liters, but the aspect ratio, the ratio of outer diameter to the axial length, is flexible. The available volume and required power density is demanding and almost identical as the rare-earth based design in Nissan leaf [38]. For the ferrite magnet, the grade FB9B is chosen [64]; the remanent flux density, B_r, and coercivity, H_{cj}, are given in Table 3-1.

Throughout this chapter, the peak current (the maximum transient current available from the inverter) is equal to 425 A, rms, and is set as 1 per unit. Furthermore, the required peak torque value of 270 Nm is set as 1 per unit, and is defined as the maximum average transient torque that is achieved based on 1 per unit peak current.

Table 3-1
Design requirements for the Ferrite based traction motor.

Volume (include. end winding; exclude. housing)	9.5 liter
Peak torque	270 Nm
Peak power	80 kW
Base to top speed ratio	3000 rpm : 15000 rpm
Minimum available DC link voltage	400 V
Maximum winding temperature	180 ˚C
Available water cooling options	Only via outer stator frame
Demagnetization withstand capability	Under 3-phase short circuit
Ferrite, FB9B, B_r at 20˚C/ H_{cj} at 20˚C	0.44 T/ 370 kA/m
Ferrite, Ceramic, Br at 20˚C/ Hcj at 20˚C	0.38 T/ 260 kA/m
Stator and rotor laminations, SURA M270-35A at 20˚C [105]	Min Yield: 90% x 450 MPa Min Tensile: 80% x 565 MPa Young's Modulus: 185 GPa Fatigue limit: 45-55% Tensile

3.2.2 PMASynR vs. Spoke Type Topology

Due to the low remanent flux density of the ferrite magnets and the high power density requirement, Table 3-1, the magnet torque needs to be enhanced by the flux focusing technique and/or exploitation of the reluctance torque. One topology allowing this is the PMASynR topology, with 2 or more layers of magnets. An optimized 3-layer U-shape PMASynR is therefore designed, where the stator is comprised of a distributed winding with a slot per pole and phase equal to 1 to maximize the reluctance torque contribution. A rotor with eight poles is selected; this relatively high pole number is chosen in order to reduce the ampere turn seen by each magnet during the short circuit fault, thus reducing the demagnetization risk. However as is shown in Figure 3-1(a), by having a high pole number the available space for the magnets is too limited to allow magnets to be placed in the inclined layers. This means that the opportunity for a torque increase via the flux concentration is lost. To highlight the impact of number of poles on demagnetization and torque density, Figure 3-1 compares the 8-pole design with a 4-pole design in which the inclined layers offer sufficient space to allow magnets to be fitted, with the layers suitably tapered toward the airgap. The demagnetization proximity for the two designs at the worst rotor position are illustrated where 160% of the peak current (approximating the peak short circuit current) is applied in the negative d-axis direction, while the red colour indicates the areas prone to demagnetization; it is shown that, whilst the 8-pole design is safe from demagnetization the 4-pole design is heavily at risk.

(a)   (b)
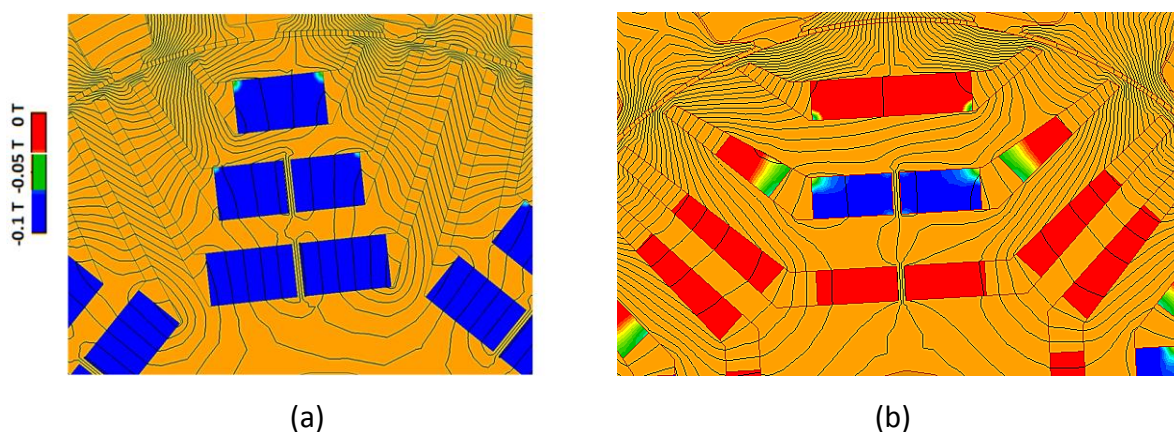
Figure 3-1: Demagnetization proximity, PMASynR U-shape designs with ferrite magnets.
(a) 8-pole design. (b) 4-pole design.

The torque vs. speed characteristic of the 8-pole design is calculated and shown in Figure 3-2; it can be noted that for the available volume the optimized design may not fulfil

the required peak torque at the low speeds and, with a larger deficit, the required constant power range from the base to the top speed. To highlight that it is the weak ferrite magnets which result in the lower than required performance, they are substituted with strong NdFeB magnets (Br equal to 1.2 T at 20˚C and H_{cj} equal to 1000 kA/m at 100˚C), with no other change in the design. The torque vs. speed characteristic is again shown in Figure 3-2; it can be seen that, in contrast to the design with ferrite magnets, the 8-pole design with the rare-earth magnets is able to satisfy and exceed the constant torque and constant power range requirements.
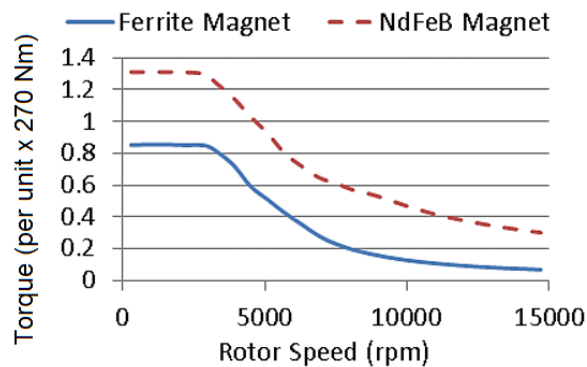
Figure 3-2: Torque-speed performance of 8-pole PMAsynR design with ferrite and NdFeB magnets.

Another viable rotor topology is a three layer V-shape design, similar to that reported in [55]; in this topology, as an advantage over the U-shape alternative, the flux concentration with a high pole number configuration can still be achieved. However, it can be shown that, for a U-shape and, more significantly, a V-shape PMASynR topology, to obtain a high ratio of reluctance torque and to avoid excessive saturation of the rotor material, the rotor mass and the associated stress at high speeds will significantly be increased. To mitigate the rotor structure stress at high speeds, the rotor posts and bridges have to be accordingly widened, which in turn leads to excessive flux leakage and torque loss. On this basis, although a three layer V-shape design may fulfil the required torque density at low to medium speed range (such as in [55]), it may not fulfil the high power density requirement in Table 3-1.

In comparison to a PMAsynR, the spoke type rotor design provides more space for magnets per given motor outer diameter (OD) thus allowing a higher number of poles without compromising the flux concentration effect; in addition, with this topology, significant reluctance torque can still be achieved. The topology also allows for demagnetization control via appropriate design of rotor pole tips and appropriate magnet

27

placement between the poles. Finally, unlike the PMASynR solution which is based on a single piece rotor lamination, in a spoke type topology the posts and bridges may be fully eliminated by employing a two part fir-tree based rotor structure; as a result, the speed and power density of the spoke type design can significantly be increased without a compromise on the flux leakage and performance.

Based on a multi-physics based optimization, Figure 3-3, performing several iterations between the electromagnetic and structural FE design packages, an optimal spoke type design with a distributed winding (slots per pole and phase, q, equal to 2) has been achieved. The design cross section is shown in Figure 3-4, and some key dimensions are reported in Table 3-2. Some of the major steps during the design optimization procedure, see Figure 3-3, can be summarized as follows: a) The number of poles has been maximized to reduce the stress, via reduction of mass per pole, and demagnetization risk, via reduction of ampere turns per pole, Figure 3-3 (b). The maximization of the pole number has been limited by the switching capability of the IGBT inverters, which, in this thesis, has been equal to 1.25 kHz for the fundamental voltage waveform, [106], as a result of which a 10 pole design has been obtained; b) The magnets radial height has been maximized (limited by the rotor mass and the maximum stress allowed based on the structural analysis) to maximize the torque and power density; c) The circumferential width of the magnets was maximized (limited by the available space for the fir tree inclusion and the deviation from optimal ripple torque) to reduce the demagnetization risk; d) The open and rectangular slot configuration is chosen to maximize the torque density and to allow for the use of wires with rectangular cross section (to increase the slot fill factor and minimize the winding loss); e) During the analytical phase of the design, the transfer heat coefficient from the coils to the cooling housing is set to 100 kWm^{-2}, which is based on the past empirical findings for the similar size traction motors employing a water cooling in the external housing, [107].

The rotor of the design in Figure 3-4, is comprised of 5 axial sections, facilitating the rotor assembly, and enabling the skew. The rotor support is made of non-magnetic steel due to its optimal structural properties and low costs, while the rotor poles are made of the same material as the stator laminations to improve the raw material utilization and achieve further cost savings.

It should be noted that in Figure 3-3, only some of the fundamental optimization steps have been reported; the more detailed design considerations such as demagnetization and the rotor structural design have been discussed in the following sections.
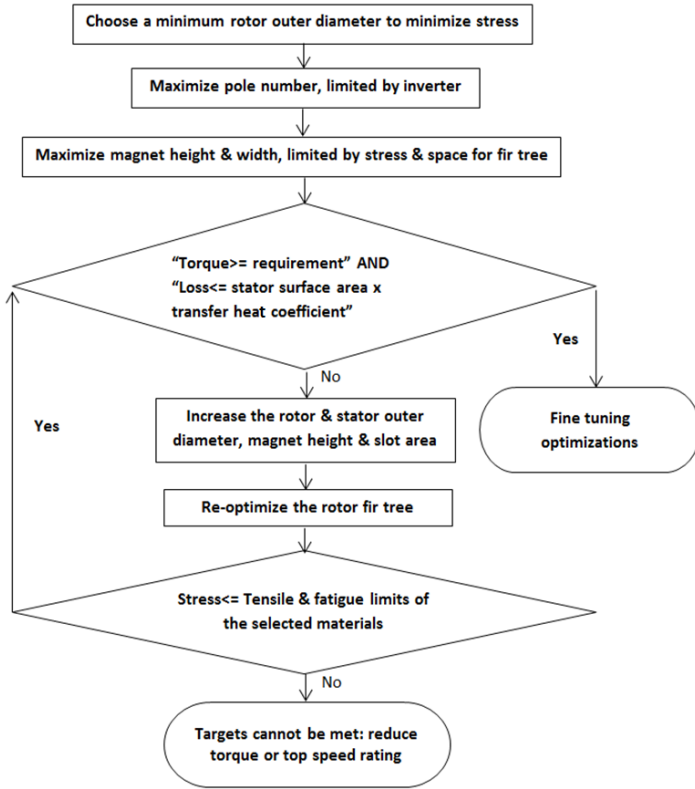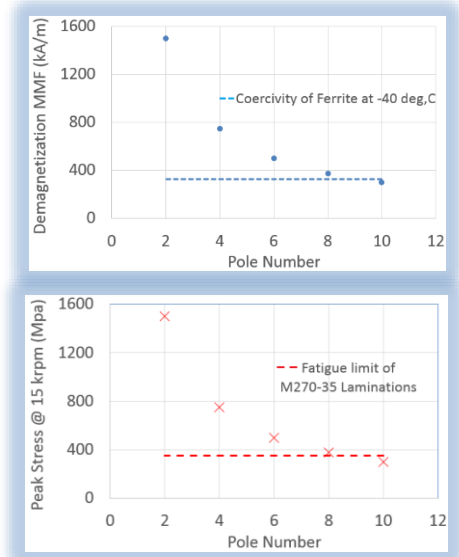
Figure 3-3: (a) Design optimization algorithm of the spoke type design. (b) Influence of the number of poles on the demagnetization and rotor stress.
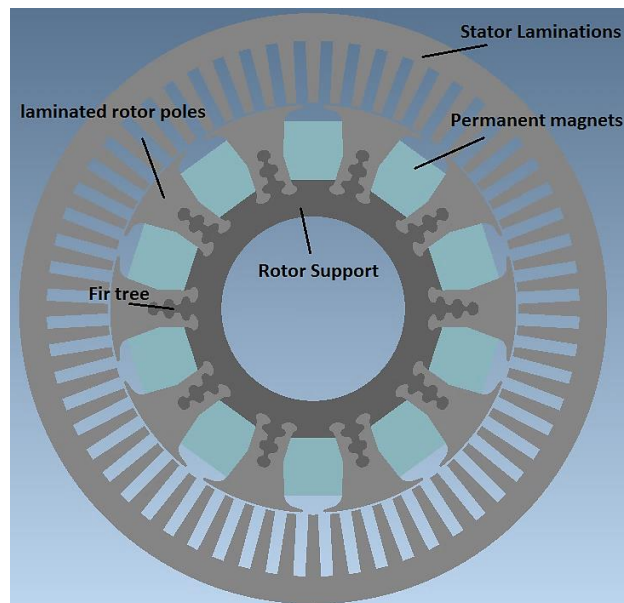
Figure 3-4: A cross section of the optimized spoke type design.

Table 3-2
Major dimensions of the spoke type design.

Stator outer diameter (mm)	205
Rotor outer diameter (mm)	140
Stack length (mm)	195
Airgap (mm)	0.5

3.2.3 Electromagnetic Analysis

3.2.3.1 Electromagnetic torque and efficiency map

The peak transient torque waveforms of the spoke type design corresponding to the base and top speed are shown in Figure 3-5, where the torque and corresponding power fulfil 100% of the requirement values in Table 3-1. To reduce the ripple torque, each rotor slice is shifted by 1.2 degree, as a result of which the ripple is reduced by factor of 2~3, while the average torque is reduced by 4%, as shown in Figure 3-5.
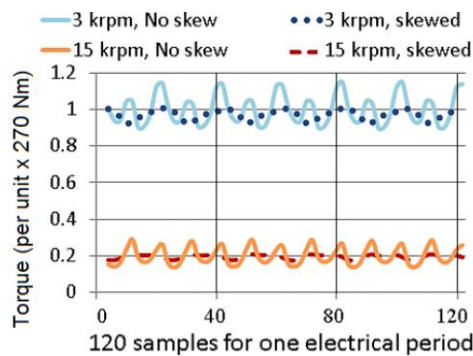
Figure 3-5: Peak transient torque waveforms at base and top speed, with and without skew.

The windings loss (assuming copper wires with 45% fill factor) and the iron loss, including stator and rotor laminations, for the peak torque/ power operation vs. speed are shown in Figure 3-6(a); the per unit values are with reference to the maximum power output of the motor, i.e. 80 kW. It should be noted, that due to the high electrical resistivity of the ferrite magnets, these magnets do not contribute to any loss, regardless of the operational conditions; furthermore, the eddy current loss in the rotor support is negligible (equal to, only, 0.0001 per unit at the worst operating condition) owing to the distributed winding and the low rate of flux variation in the support region. As shown in Figure 3-6(a), for the maximum torque operation, the winding loss dominates the iron loss for, almost, the entire speed range.

To assess the total loss and efficiency at different operating conditions, the efficiency map as well as two representative key operating points (i.e. the points at which the motor

frequently operates: one corresponding to the urban driving, and one corresponding to the highway cruising, both in line with the Range Rover Evoque-E vehicle specifications, [108]) are shown in Figure 3-6(b). It can be realized that the efficiency of the design at both of the key operating points is above 95%, which is comparable to the state of the art designs with the rare earth magnets, [36]. Furthermore, it can be shown that the iron loss exceeds the winding loss and becomes dominant at lower range of torque and higher range of speed, including the key operating points in Figure 3-6(b). The major reasons behind the achieved level of high efficiency can be summarized as: a) high airgap flux density due to the flux concentration, which results in less required armature current and winding loss for a given power, b) lossless ferrite magnets in rotor, c) distributed winding, d) despite the open slot configuration the width of the slot relative to the magnets is, rather, small owing to the high winding distribution factor.

(a)

(b)
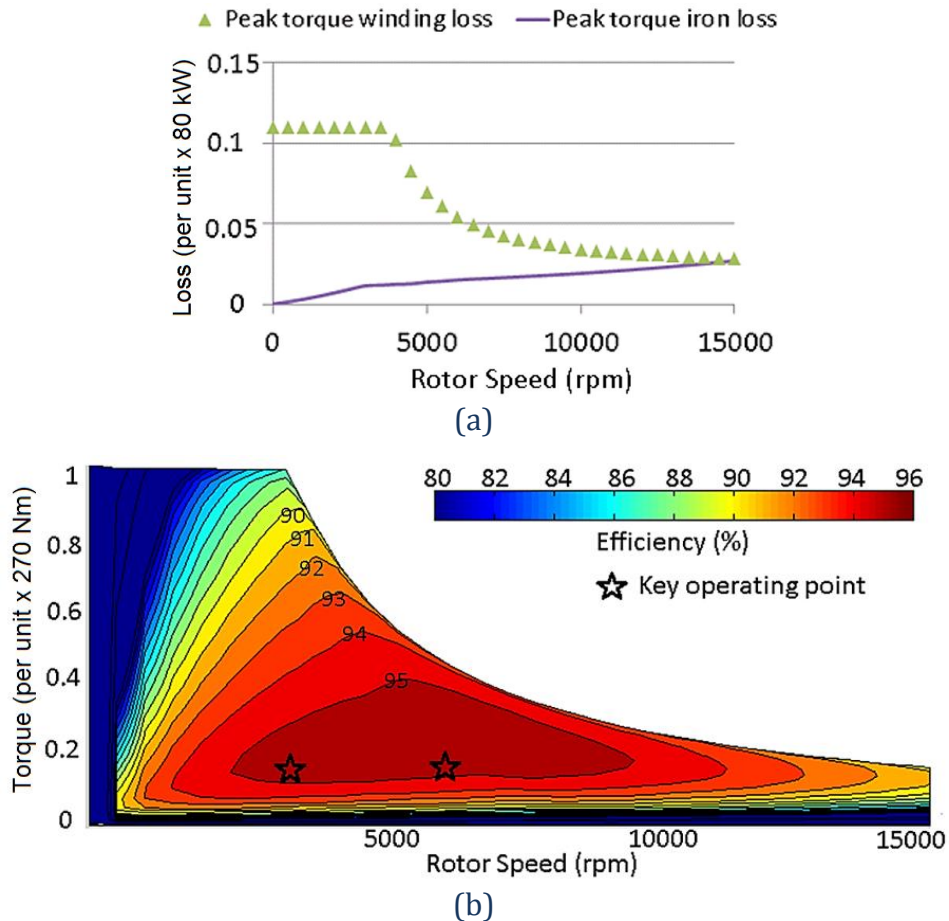
Figure 3-6: Loss and efficiency map of the proposed spoke design. (a) Winding and iron loss for peak power operation. (b) Efficiency map.

3.2.3.2 Demagnetization

Ferrite magnets have approximately one fifth to one third of the coercivity, H_{cj}, of the rare earth magnets; for example a value of 330 kA/m in FB9B Ferrite at -40˚C compared to 900-1600 kA/m in NdFeB magnets at 100˚C. Furthermore, in an EV application with a high constant power to speed ratio, such as presented in the current thesis work, currents almost as large as the peak current, i.e. 1 per unit, may be applied in the negative d-axis due to the high current advance angles applied at higher speeds. Even more critically, during a short circuit fault negative d-axis currents with larger amplitude than the peak current can develop, against which the magnets need to be able to retain their full magnetic properties.

To avoid demagnetization in the presented spoke design, several design aspects have been observed: a) the number of poles is maximized following the explanation in Chapter 3.2.2; b) the magnets are given adequate thickness in the circumferential direction to increase the magnetic reluctance in the d-axis; and c) the rotor ferromagnetic pole tip on top of the magnets (in a semi-open bridge configuration) is given adequate radial thickness and circumferential extension to encourage and bypass the stator d-axis fields during the extreme field weakening or short circuit faults.

A design solution whose merit is less apparent in the rare-earth magnet based designs, but which is crucial in the case of ferrite magnets, is to assign a non-magnetic void not only to the top, as proved effective in [66], but also to the bottom of the magnets as shown in Figure 3-7(a) for a rather simplified model (the semi-open bridge in the actual design is approximated by a radially thinner full-bridge). These voids provide a leakage path for both the d-axis armature fields and the magnet flux. The voids enable the armature and magnet to form two decoupled magnetic circuits whereas, were no voids allowed for, they would form a series coupling as a result of which the magnets would have to face the strong and negative fields from the armature and therefore higher risk of demagnetization. To highlight the suitability and necessity of this approach, in Figure 3-7(b) the bottom void, and in Figure 3-7(c) both top and bottom voids have been removed; furthermore, in Figure 3-7(d) the bridge thickness is increased from 1 mm to 2 mm as an attempt to compensate the void removal. The demagnetization proximity is illustrated for a 160% peak current applied in the negative d-axis (resembling the peak short circuit current), where red zones illustrate the areas that will be demagnetized. As shown, removing the voids (Figures 3-7(b) and 3-7(c)) significantly deteriorates the ability of the magnets to withstand demagnetization, while doubling the bridge thickness only provides marginal improvement (Figure 3-7(d)).

Furthermore, while thickening the bridge (e.g. Figure 3-7(d)) significantly deteriorates the torque capability of the motor due to excessive leakage during the normal operation, the provision of non-magnetic voids would have negligible impact as is demonstrated in Figure 3-8; this shows how the assisting role of the latter come into effect only during the rise of strong and negative d-axis fields. With regards to Figure 3-8, it should be noted that the demagnetized regions in Figure 3-7 have not been accounted for in the torque-speed calculation.

In the case of the proposed design in Figure 3-4, the aforementioned voids are accommodated via the non-magnetic rotor support at the bottom, and the non-magnetic wedge at the top; both with appropriate thicknesses inspired from Figure 3-7. The inclusion of wedge also mitigates the risk that fragments of magnetic material are able to enter the airgap region. To fully assess the design, a 3-phase short circuit, initiated with the motor operating at base speed and at peak regenerative torque, is simulated in FE. The resulting currents are displayed in Figure 3-9 (fault occurring at t=4 msec), indicating the peak short circuit current occurring in Phase A and equal to 1.6 times the rated peak current. The field strength (H) and flux lines corresponding to the most extreme rotor position are displayed in Figure 3-10. Here, the maximum field strength in the magnet is close to the bottom surface and is about 300 kA/m, which is 10% lower than the H_{cj} of ferrite magnets at -40˚C. Furthermore, following the earlier explanation of the impact due to the inclusion of the voids, the field strength is largest near the airgap and rotor pole tips on top and bottom of the magnet but decays radially in the voids approaching the magnet's top and bottom surface. The magnet flux can be seen to leak primarily through the void beneath the magnet, while the armature flux leaks partially through the rotor pole tips and more significantly through the top and bottom voids.
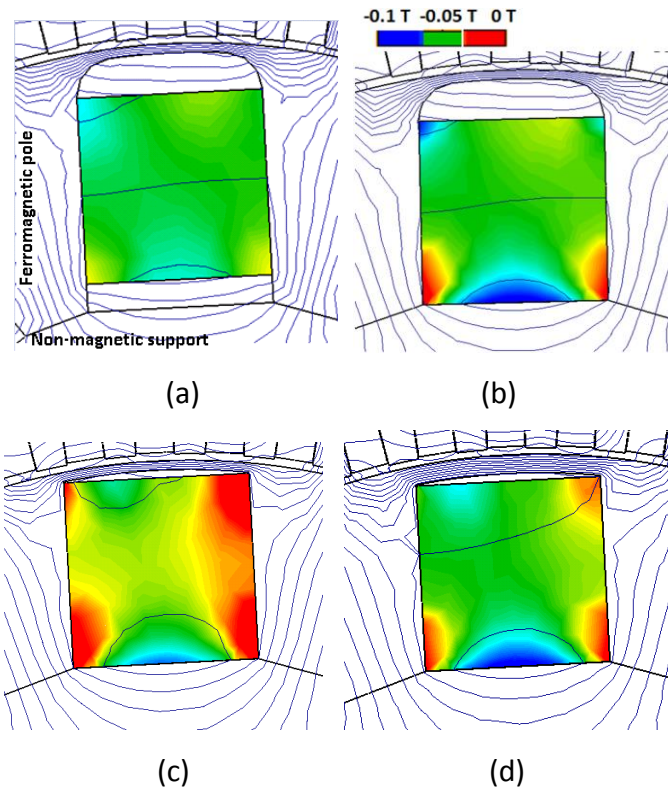
Figure 3-7: Demagnetization proximity. (a) 1 mm bridge, 4 mm and 3 mm top and bottom air voids. (b) 1 mm bridge, 4 mm top air void, no bottom air void. (c) 1 mm bridge, no air voids. (d) 2 mm bridge, no air voids.
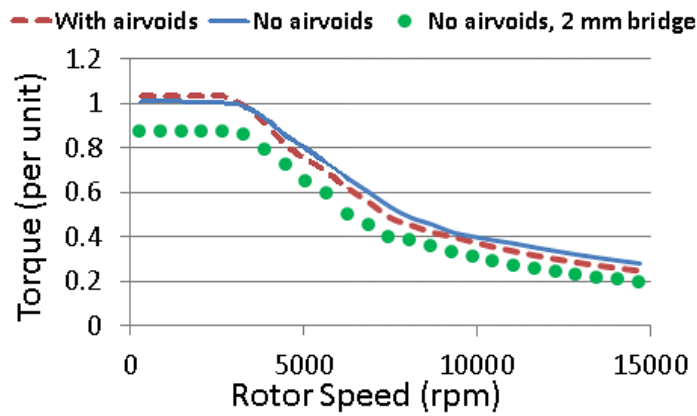
Figure 3-8: Torque-speed comparison for designs with/ without air voids and different bridge thicknesses (the effect of demagnetization on the torque is excluded).
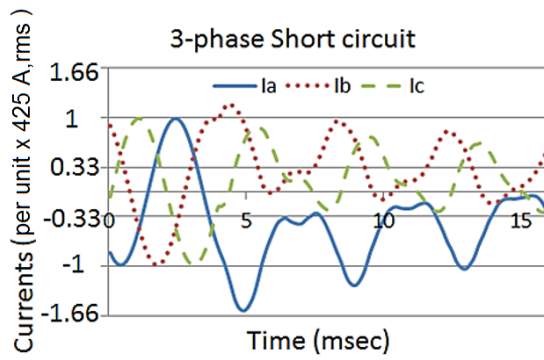
Figure 3-9: 3-phase short circuit currents.
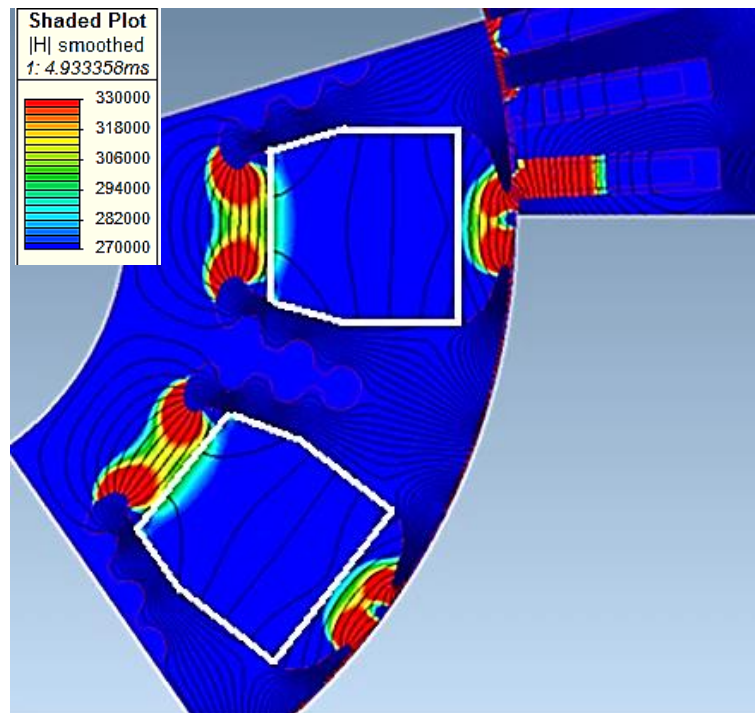
Figure 3-10: Field strength (A/m) distribution during 3-phase short circuit.

Finally, the impact of the inclusion of a stator tooth tip on demagnetization has been studied. It has been observed to have an impact comparable to the rotor bridge, both in terms of providing limited protection against demagnetization as well as resulting in a torque loss.

3.2.4 Rotor Structural Analysis

To hold the rotor poles and magnets to the non-magnetic rotor support at high speeds, a so-called fir-tree connection was adopted, Figure 3-4. It can be shown that the torque density of the spoke design is proportional to the radial height of the magnet, which itself is limited by the increase of mass in the rotor pole and magnets and thus the stress in the rotor

pole segments and support. To meet the torque requirement in Table 3-1, by achieving the required magnet height in Figure 3-4, several fir-tree configurations have been investigated through 2D elastic-plastic FE structural analysis. This analysis has included an optimization against the excessive rotor plastic deformation and the radial expansion at maximum working speed (15,000 rpm), as well as against fatigue failure due to rotor speed changes. To design against the fatigue failure, the analysis aims at an infinite fatigue life for the most severe rotor operating cycle, i.e. a fatigue stress range resulting from the largest rotor speed variation possible (between 0 rpm and 15,000 rpm) for the entire life time of the vehicle.

Figure 3-11(a) shows an early design (only half of a pole segment is shown due to symmetry) in which a high number of fir tree teeth have been chosen to efficiently distribute the mechanical loading. In addition, two circular cavities have been incorporated in the upper part of the pole to reduce the pole mass and thus the stress at high speeds. As indicated in Figure 3-11(a), a number of design variables were examined during the optimization to minimize the stress concentrations at high speed: a) increasing the radius of the bubble cut-out connecting to the upper-most fir-tree tooth and smoothing the curvature, b) reducing the height of the lower fir-tree teeth, and c) enlarging the radius and smoothing the curvature of the bottom fir-tree shoulder.

The stress distribution in the initial design, Figure 3-11(a), is obtained by FE and is shown for the maximum working speed of 15 krpm in Figure 3-12. It can be observed that: a) The maximum stress in the rotor pole is almost evenly distributed with the maximum occurring at the top of the bubble cut-out indicating a need to further enlarge the corresponding bubble radius, and b) Stress on the support is significantly higher than on the poles, thus requiring a stronger material, for which 316 stainless steel with 3% work hardening is selected (this option is about 5 times cheaper than copper beryllium chosen in [46]). Meanwhile, the peak loading occurs in the fir-tree bottom shoulder which requires larger radius and further smoothing.
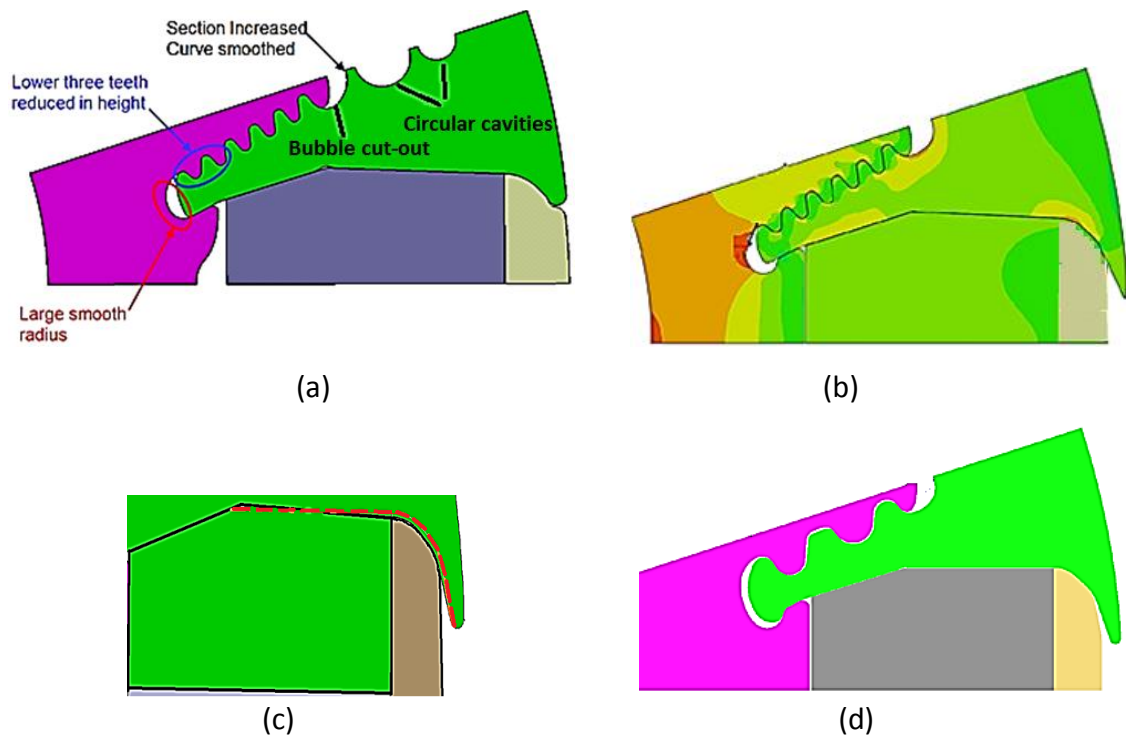
Figure 3-11: Evolution of the rotor structural designs. (a) Initial design. (b) Top cavities removed. (c) Parallel vs. tapered face magnets. (d) Number of teeth reduced.

The two circular cavities in the pole segment of the fir tree design in Figure 3-11(a) were found to deteriorate the magnetic performance by reducing the magnet torque (due an increase in the reluctance in front of the magnets) and also via a reduction in the reluctance torque, this being due to a reduction of the q-axis inductance. Furthermore, it was realized that a careful extension of the rotor pole tips could enhance the demagnetization withstand capability. As a result, in the subsequent design iteration, Figure 3-11(b), the cavities are removed, and the pole tips extended, while fir-tree geometry improved accordingly to reduce the maximum stress levels.

To enhance the manufacturability, however, the number of fir-tree teeth is reduced from 6 to 3 in a later design; there was concern that a large number of small teeth would be sensitive to small variations in manufacturing tolerances. Furthermore, through parts procurement, it was realized that the required manufacturing tolerances for the relatively complex ferrite magnet geometry were difficult to achieve. Through a simplification of the geometry, having a simpler shape with parallel magnet faces instead of tapered ones, as is shown in Figure 3-11(c), better dimensional tolerances could be achieved. As a result, the final design, Figure 3-11(d), was based on several modifications to accommodate both the reduced number of fir tree teeth and the extra loading on the pole segment as a result of eliminating the tapering of the magnet faces. The stress distribution for the final fir-tree

design at the maximum working speed of 15 krpm is shown in Figure 3-13. As shown, by modifying the rotor structural design from Figure 3-12 to Figure 3-13, the peak stress is reduced by about 15% in the pole segment and 24% in the rotor support.
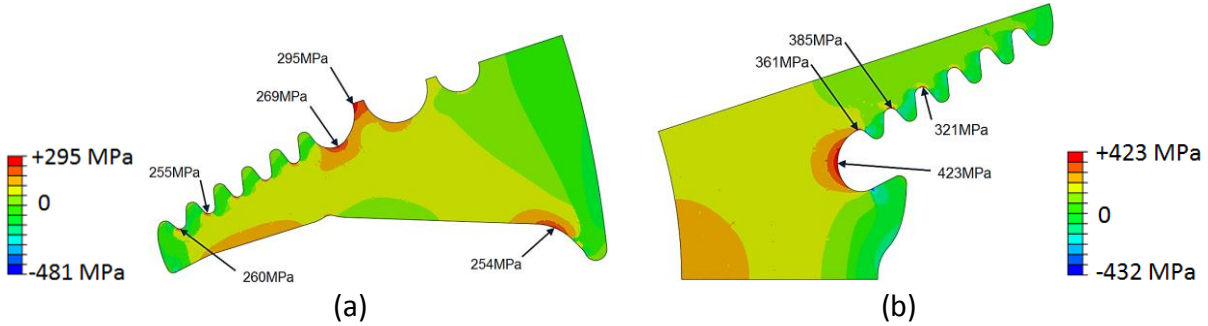
Figure 3-12: Stress distributions at 15 krpm, initial fir-tree design. (a) Rotor pole. (b) Rotor support.

It should be noted that, despite the similarities of the fir tree topology of Figure 3-13 to that in [46], the former benefits from about 30% lower stress in the pole segment and 50% lower stress in the rotor support at a same top speed; the difference is majorly due to the optimization guidelines described and followed in this chapter. As a result, in the disclosed design, a substantially cheaper rotor support material has been employed, while, for a similar level of fatigue and product life time, higher speeds and power densities can be achieved.
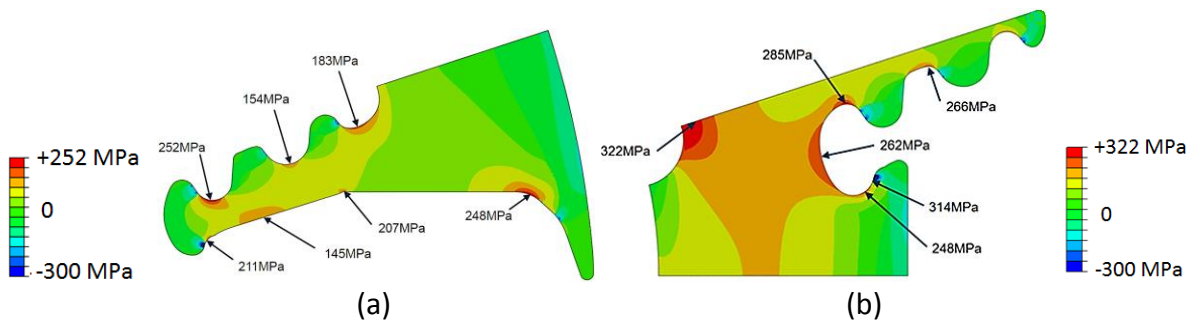
Fig 3-13: Stress distributions at 15 krpm, final fir-tree design. (a) Rotor pole. (b) Rotor support.

3.2.5 Manufacturability for High Volume Production

Due to the two-part rotor structure of the proposed design, the required geometrical tolerance of the fir tree (as a joint between the rotor support and the rotor pole) must be, finely, respected to avoid interference fitting problems during the assembly processes. As a result, to facilitate the assembly process for the mass production, the rotor parts should be

checked against the specified geometrical drawings during the parts manufacturing procedure and as part of the quality control stage.

The necessity for a high quality manufacturing process might imply a certain cost increase when comparing the proposed two-part rotor design against the single piece alternatives, such as [35]; however due to the higher torque density of the two-part rotor topology (owing to the less electromagnetic leakage than that in the single piece alternative), and due to the fact that the aforementioned manufacturing and quality control costs may be, significantly, reduced for a high volume production (as opposed to one off or low volume production), it is expected that the proposed ferrite rotor design will maintain its favourability in terms of the performance per cost.

3.3 Conclusion

In this chapter, an optimized ferrite magnet based motor design for a high power density EV application was presented. From different rotor topologies, the spoke type is explained to be the best suited, due to a simultaneous potential for obtaining high torque density, high demagnetization withstand capability, and a robust rotor structure for high speed operation. The resistance against demagnetization is optimized via a combination of techniques, namely: having a high number of poles; shaping and extending the rotor pole tip; widening the magnets; and most significantly, by incorporating the non-magnetic voids on the top and bottom of the magnets. The required torque density was achieved by maximizing the radial height of the magnets, enabled through an extensive optimization of the fir-tree design. The detailed optimization of the rotor structure resulted in substantially lower stress levels compared to the state of the art, based on which a product cost reduction can be envisaged, while an opportunity rise for further increase of the top speed and power density. The disclosed motor design is claimed to surpass the state of the art in terms of performance (power density, demagnetization withstand capability, and rotor integrity) and cost. Finally, this chapter has provided a better understanding of the interactions between the electromagnetic, structural and manufacturing issues involved within a cost effective industrial product.

3.4 Acknowledgement

Chapter 4 : STACK LENGTH IMPACT ON DEMAGNETIZATION AND UTILIZATION OF POORER MAGNET MATERIALS FOR EV/ HEV APPLICATIONS

4.1 INTRODUCTION

In this chapter, the 3D effects of the stack length on the demagnetization are investigated. The investigation has been made using 3D FE (assuming non-linear materials), which is performed on a high power density spoke type ferrite motor, the design details of which have been previously presented in Chapter 3. A lumped magnetic circuit model is derived and used to explain the observations from the 3D FE, based on the variation of the magnet load line against the circuit parameters. Using the proposed model, the effects of the stack length and the magnetic saturation are decomposed and explained. The practicality of the concept is benchmarked by comparing two grades of ferrite magnets (one with 30% lower H_{cj} than the other) in terms of the demagnetization resistance and the static torque performance.

The contributions of this chapter are in the following areas:

a) The provided analysis, for the first time in the literature, identifies and explains an important relation between the stack length and the permanent magnets demagnetization performance within an electric motor application.

b) Following a detailed proof and explanation of the phenomenon, which has been a source of deviation between the simulation results and the prototype testing, Chapter 8, the concept is, further, viewed as a potential measure to exploit cheaper grade of magnets for high performance low cost traction motor applications. On this basis, some first principle design assessments and validations for both low power (HEV) and high power (EV) designs have been provided.

c) Finally, the 3D concept has been formulated using a simple but practical reluctance based coefficient, which can be incorporated into any existing design optimization program, resulting in a more accurate estimation of the demagnetization behaviour, and achieving cheaper and higher performing motor designs.

The contents in this chapter have led to the following publication:

- **M. Kimiabeigi**, J. D. Widmer, N. Baker, *et al.*, "3D Modelling of Demagnetization and Utilization of Poorer Magnet Materials for EV/ HEV Applications," IEEE Trans. Energy. Convers early access publications, vol. 31, no. 3, pp. 981-992, April 2016.

4.2 Original EV Motor Design and Motivation for Study

The analyses in this chapter are related to the ferrite motor design disclosed in Chapter 3, with the design specifications summarized in Tables 3-1 and 4-1. A one-tenth model of the design, applying half axial symmetry, and including only two coils belonging to one of the phases is shown in Figure 4-1.

(a)	(b)
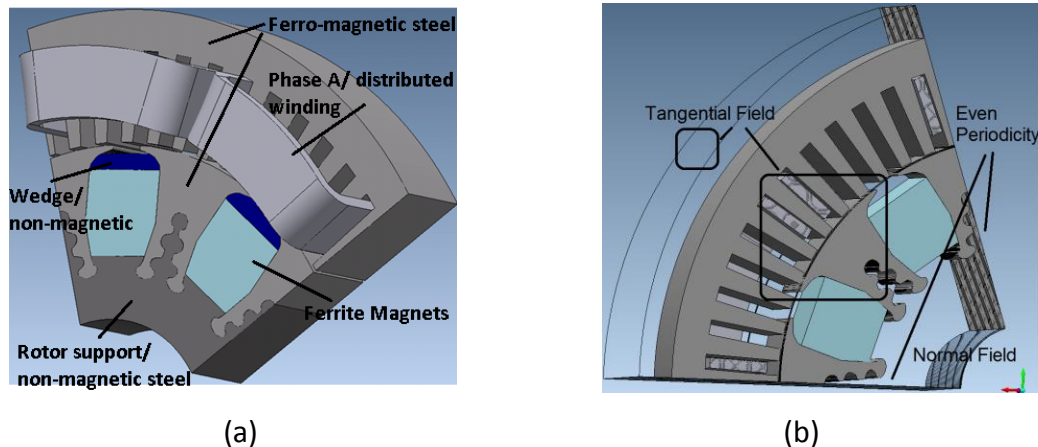
Figure 4-1: (a) 3D model of the reference motor design, with one-tenth of the original length. (b) Boundary conditions.

To simplify early prototype build and test set-up, a prototype with same 2D profile but one-fifth of the stack length has been constructed. During test, Chapter 8, it was observed that the demagnetization withstand capability of the short length prototype is significantly better than the 2D FE predictions (which assume an infinitely long machine). As a result in this chapter, to validate the effects of the stack length on demagnetization, an in-depth 3D analysis has been presented. It was intended that this study would improve understanding of demagnetization in ferrite based motor designs as this is one of the major obstacles in their use for traction application.

With regards to the FE analysis in this chapter, the laminations are assumed to be isotropic, neglecting the effects of the laminations gaps (insulation thickness) on the axial flux component. On this basis and using the 98% available stacking factor value for the laminations, an additional 0.39 mm axial airgap in either side of the rotor stack can be envisaged, which is expected to diminish the axial flux component in the laminations, and adding to the leakage. The boundary conditions of the 3D model have been illustrated in Figure 4-1(b).

4.3 Influence of Stack Length on Demagnetization

4.3.1 3D FE modelling

To quantify the effect of the stack length on the demagnetization performance, a large current (400% of the peak inverter current, I_{pk}, Table 3-1) has been injected in the negative d-axis position, and the stack length has been varied from the design value of 195 mm to 39 mm (1/5th axial length). The field strength, H, observed in the magnets for a number of different stack lengths was studied, and the results are shown in Figure 4-2. The red areas are those where the H field is greater than the intrinsic coercivity of the FB9B grade Ferrite magnet at 20˚C, and therefore complete demagnetization may be expected. Furthermore, to better understand the end effects the demagnetization at both the end face, i.e. the face closest to the end windings, and the middle stack face, i.e. the face farthest from the end windings, are simulated and both shown in Figure 4-2. It should be noted that the choice of 400% I_{pk} as the basis for analysis, which is much larger than the simulated three phase short circuit current of 160% I_{pk}, Figure 3-9, is partly to improve the visibility of the comparisons (which, also, includes, the study of the effects due to the magnetic saturation), and partly to address the more severe conditions such as asymmetric single phase short circuits, [69].

From Figure 4-2, it can be observed that the field strength inside the magnets is significantly reduced as the stack length decreases. Whilst for the 195 mm stack length design, a significant portion of the magnets is at risk of full or partial demagnetization, for the 39 mm stack length the risk is reduced to zero. Furthermore, on the end face the circumferential edges of the magnets are always at risk of demagnetization, almost regardless of the stack length of the design; however, as the axial depth of the end face demagnetized region is very limited (about 1 mm), this region will not have a noticeable impact on the overall performance. Finally, it should be noted that the 3D FE results converge to 2D FE predictions for, relatively, long stack lengths, in this case the 3x39 mm stack length and beyond.

The phenomenon in Figure 4-2 can be partly explained due to the 3D variation of the magnetic reluctance, and partly based on the magnetic saturation effects; both of these effects are addressed analytically in the following sections. To support the analytical modelling, the flux vectors and flux density in different regions of the 3D model have been plotted (for different stack length models and different current amplitudes) and shown for the 39 mm stack model in Figure 4-3. As can be seen for the periodic 2-pole model in Figure 4-3, during 3-phase short circuit conditions (corresponding to 160% peak inverter current) a

significant portion of the armature field results in slot leakage (indicated as slot leakage flux in Figure 4-3) and therefore does not reach and endanger the magnets in the rotor. However, some portion of the armature field (illustrated as demagnetizing flux in Figure 4-3) passes the airgap and influences the rotor, including the pole tips and non-magnetic regions on top and bottom of the magnets. This field has the potential to cross and reverse the polarity of some parts of the magnets, leading to demagnetization.

The path of the demagnetizing flux is indicated in Figure 4-3. To better assess the reluctance of the stator and airgap (to be used in the next section for the analytical modelling), the flux density in the most flux concentrated region of the yoke (located in the middle of the critical yoke edge in Figure 4-3(b)) and in the airgap, (identified as the critical point in the airgap in Figure 4-3(a)), are calculated and compared for 39 mm and 3x39 mm stack lengths in Figures. 4-4 and 4-5. As can be seen in Figures 4-4 and 4-5, for the low levels of demagnetizing currents i.e. when saturation is negligible, shortening the stack length results in the increase of the flux density in both the stator and the airgap. The source and implication of this phenomenon are discussed in Appendix I.
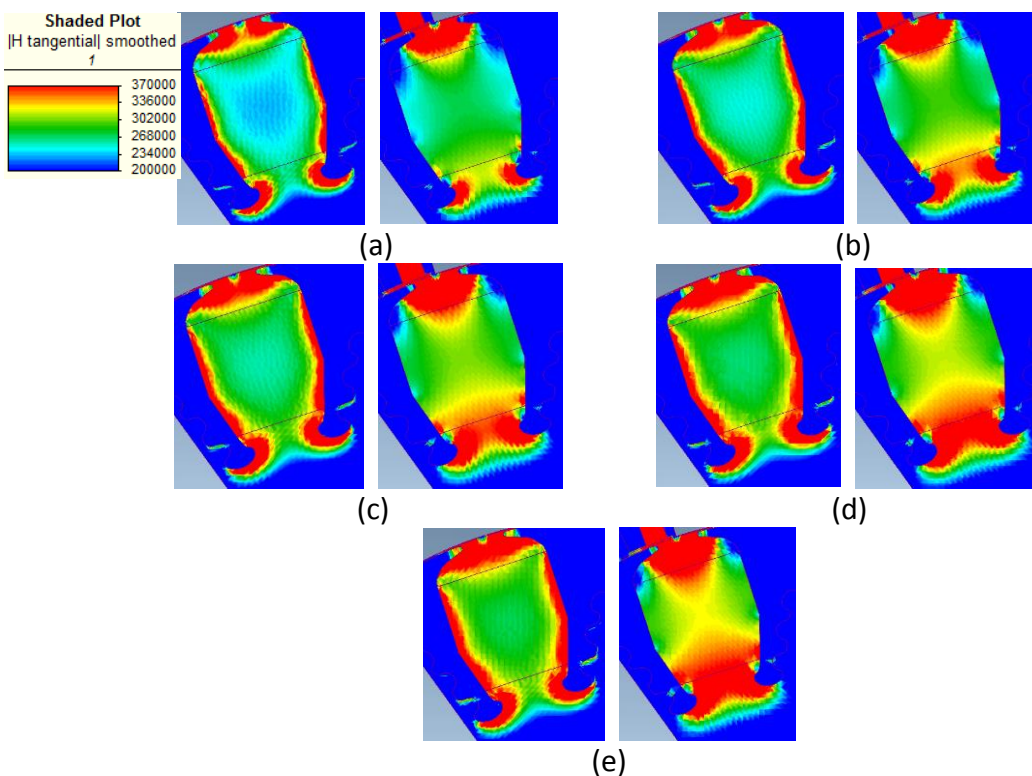
Figure 4-2: H distribution in the FB9B magnets, 400% I_{pk}, models with different stack lengths. (a) 39 mm. (b) 49 mm. (c) 59 mm. (d) 3x39 mm. (e) 5x39 mm. Left column: end faces. Right column: middle stack faces.

(a)   (b)
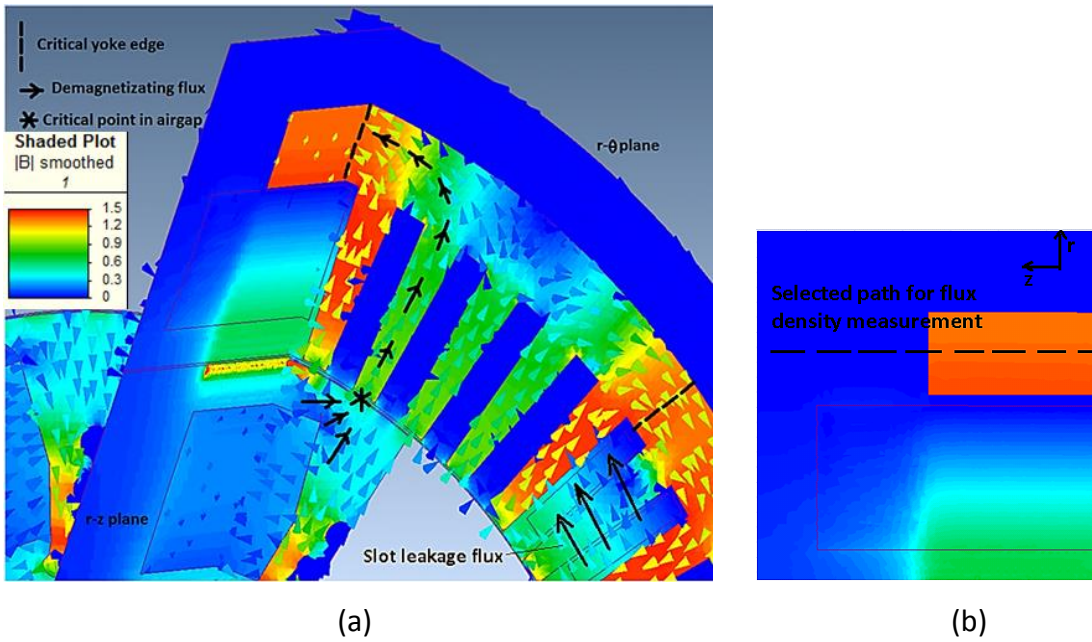
Figure 4-3: 3D flux vector and flux density distribution in 39 mm stack model, under 160% I_{pk}.

(a) Illustration of demagnetizing flux path and representative locations in airgap and yoke for

flux density assessments. (b) Middle yoke selected path line for flux density assessments.

(a)   (b)
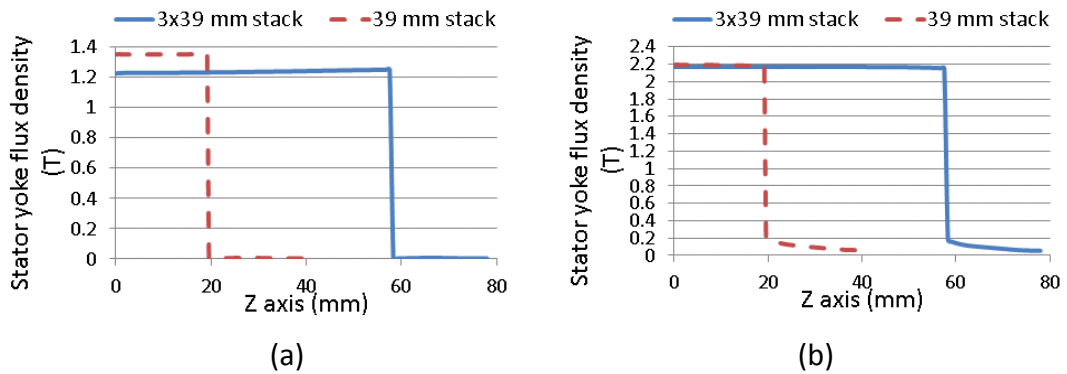
Figure 4-4: Representative flux density in the stator. (a) 160% I_{pk}. (b) 400% I_{pk}.

(a)   (b)
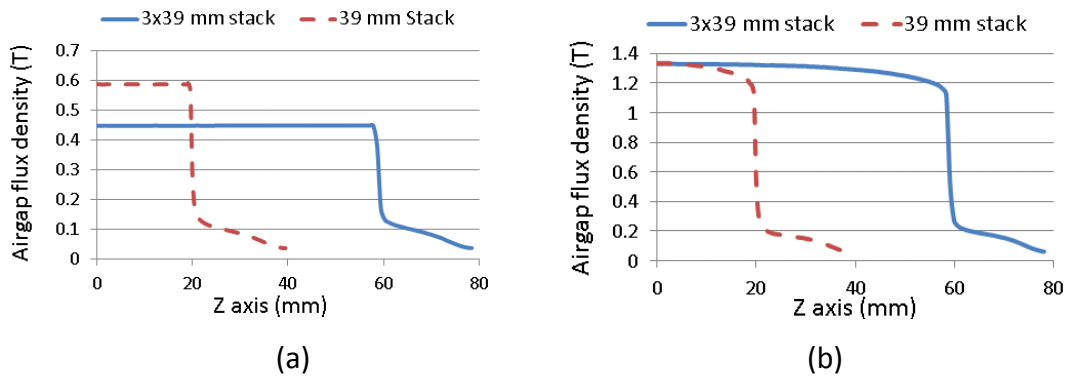
Figure 4-5: Representative flux density in the airgap. (a) 160% I_{pk}. (b) 400% I_{pk}.

45

4.3.2 Lumped circuit modelling

To explain the phenomenon in Figure 4-2, a lumped magnetic circuit consisting of the armature reaction field and the magnets is proposed in Figure 4-6. In this circuit, H_m corresponds to the field strength across the magnet, l_m is the width of the magnet along the magnetization direction, B_m corresponds to the operating flux density inside the magnet, A_m is the surface area of the magnet perpendicular to magnet flux, N is the number of turns in series, i is the armature current peak value, $R_{lamination}$ is the magnetic reluctance of the stator lamination observed by the armature field along the active stack length, $R_{end,\,arm}$ is the equivalent reluctance observed by the end winding field, R_δ is the airgap reluctance associated with the active stack length, $R_{PM,\,Internal}$ is the internal reluctance of the magnet, and $R_{leak,i}$, i=1,2,3 refer to the reluctance associated with the magnet leakage through the non-magnetic regions on top and bottom of the magnets, Figure 4-1, see Chapter 3, and the magnet leakage via the end faces. The reluctance parameters can be generally defined by (4.1), where l is the equivalent length of the flux traveling path, μ_r is the relative permeability of the material, and A is the surface area perpendicular to the traveling path of the flux.

$$R = l/\mu_0\,\mu_r A \tag{4.1}$$
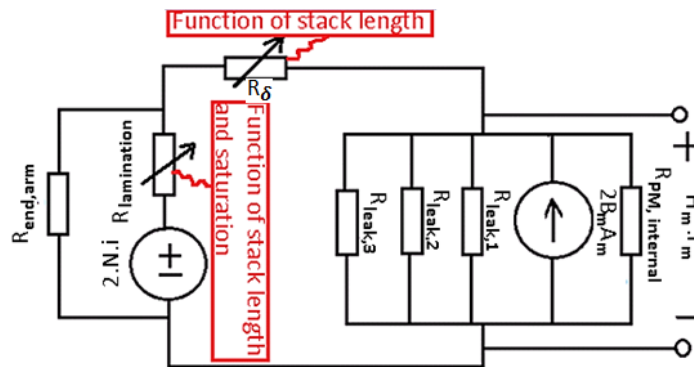
Figure 4-6: Magnetic lump circuit for 3D modelling of demagnetization.

Treating the magnetic circuit and its parameters in Figure 4-6 with an electrical analogy and using Ampere's Law the equations (4.2) and (4.3) can be obtained. Replacing the B_δ (airgap flux density) in (4.3) by H_δ (airgap field) from (4.4), and replacing the H_δ in (4.2) by its extended form, the equation of the magnet load line can be obtained as (4.5), A_δ and l_δ corresponding to airgap reluctance parameters according to (4.1). It should be noted that in (4.5), α_0 and α_1 are the state of the art coefficients based on 2D modelling, while k_0 and k_1

are the additional 3D coefficients that account for the effects of the stack length and the magnetic saturation of the stator laminations.

By assigning appropriate values of length, area, and permeability into the reluctance equation, (4.1), the magnet load line in (4.5) can be obtained for different electromagnetic conditions. The following points proved critical in tuning the circuit parameters according to the 3D FE results from the previous section:

a) The appropriate permeability and equivalent lengths of the stator reluctance, required in (4.1), were imported from the 3D FE calculations.

b) The $R_{end, arm}$ is set to be independent from the stack length and about 34 times larger than the $R_{lamination}$; this ratio being based on the inverse of the end winding to magnetizing inductance ratio, which has been derived for the design with 195 mm stack.

c) It was realized that for the non-saturated conditions, the results from the lumped circuit modelling and the 3D FE simulations match more closely when the $R_{lamination}$ is replaced by $R_{lamination-modified}$ in (iv) derived and explained in Appendix I.

$$2Ni.R_{end,arm}/(R_{end,leak} + R_{lamination}) = H_\delta l_\delta + H_m l_m \tag{4.2}$$

$$B_\delta A_\delta = 2.B_m A_m (R_m/(R_m + R_\delta + R_s)) \tag{4.3}$$

$$R_m = R_{PM,inetrnal}||R_{leak,1}||R_{leak,2}||R_{leak,3} \tag{4.3.1}$$

$$R_s = R_{end,arm}||R_{lamination} \tag{4.3.2}$$

$$H_\delta = B_\delta/\mu_0 \tag{4.4}$$

$$B_m = -k_0\alpha_0 H_m - 2.k_1\alpha_1 N.i \tag{4.5}$$

$$\alpha_0 = \mu_0.A_\delta.l_m/2A_m.l_\delta \tag{4.5.1}$$

$$\alpha_1 = \mu_0.A_\delta/2A_m.l_\delta \tag{4.5.2}$$

$$k_0 = (R_m + R_\delta + R_s)/R_m \tag{4.5.3}$$

$$k_1 = k_0.R_{end,arm}/(R_{end,arm} + R_{lamination}) \tag{4.5.4}$$

Using equation (4.5), the magnet load lines for 39 mm and 195 mm stack lengths are calculated and compared in Figure 4-7. The effect of magnetic saturation is assessed by comparing the short circuit currents with 160% I_{pk} and 400% I_{pk} amplitudes, and assigning appropriate permeabilities imported from the 3D FE simulations. The BH curve is the same as the one applied in Section 4.3.1 and belongs to the FB9B magnets at 20 ˚C.

As can be seen in Figure 4-7, the magnet load line for the 400% I_{pk} and 195 mm stack length, intersects the non-linear part of the BH curve, indicating a partial demagnetization, confirming the 3D FE observation in Figure 4-2(e). By reducing the stack length to 39 mm, the magnet load line is significantly shifted toward the linear section of BH curve, and the demagnetization risk is fully avoided with a large safety factor, again conforming to the 3D FE simulation results in Figure 4-2(a). The major driving parameter behind the aforementioned shift of the magnet load line is the increase of the $R_{lamination}$ value relative to the $R_{end, arm}$ in (4.5.4), which is due to the reduction of A, (4.1) the flux path surface area, as a result of the reduced stack length, Appendix II.

For the short circuit scenario with 160% I_{pk}, and 195 mm stack length, the magnet load line is already in a safe location on the linear part of the BH curve; however, shortening the stack length shifts the load line further inward and provides an even wider margin of safety against the demagnetization. The major driving parameter behind this phenomenon is the increase of the $R_{lamination-modified}$ value relative to the $R_{end, arm}$ in (4.5.4), which is due to the accelerated reduction of A, (4.1), as a result of the reduced stack length, and following the explanation given in Appendix I.

An interesting finding from the analysis in this section and Figure 4-7 is that, although in scenarios with negligible magnetic saturation the demagnetization improvement via shortening the stack length might still be remarkable, the effect can be more significant and better appreciated for saturated designs and conditions. This is due to the lower permeability values of the stator laminations during saturated conditions, which narrows down the gap between $R_{lamination}$ and $R_{end, arm}$ values, thereby magnifying the impact of the stack length variation on k_1 in (4.5.4).

The essential part of the circuit in Figure 4-6 can be summarized into the Magneto Motive Force (MMF) division between the active and non-active (end winding region) of the stator laminations. As shown in this chapter, taking this division into account (for both saturated and non-saturated conditions) may allow for a rapid and reliable assessment of the 3D demagnetization behaviour when changing the motor stack length. Finally, it should be noted that the presented lumped model may, only, represent an overall, and approximate, level of demagnetization, i.e. (in contrast to FE simulations) it may not identify the local demagnetization effects in different regions of the magnet.
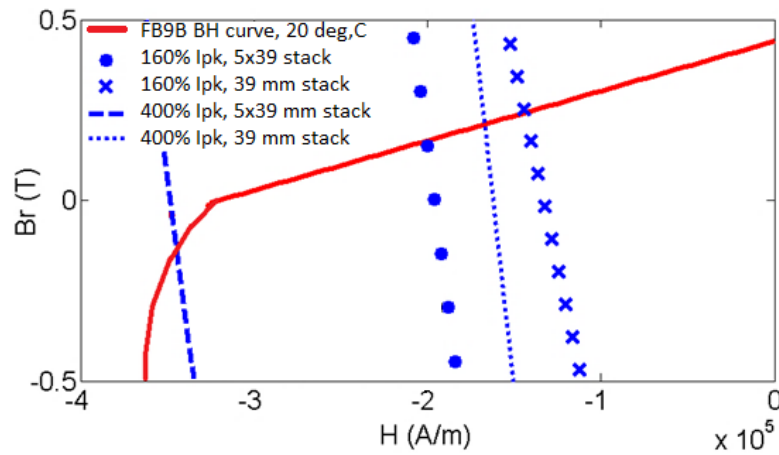
Figure 4-7: Magnet BH curve and load lines for scenarios with different short circuit currents (accounting for saturation) and stack lengths.

4.4 A Practical Application of the Concept

Based on the findings in Section 4.3, some practical design implementations can be imagined. For example, alongside with conventional 2D design methods in improving the demagnetization capability, shortening the stack length might result in considerable enhancement of demagnetization resistance and, therefore, such designs may benefit from cheaper grade of magnets with lower coercivities (this includes cheaper grade of ferrite magnets, and the NdFeB magnets with lower Dy contents). To compensate for the reduced power due to the reduced stack length, the outer diameter of the machine can be increased. A first principle design practice on this basis and using extra weak Ceramic 8 magnets has been provided in Appendix III, where a same power level as a 195 mm stack design, with mitigated risk of demagnetization, has been achieved. To evaluate the effectiveness of the approach (i.e. stack length shortening) on better utilization of weak magnets and with a vision to demonstrate the concept via an existing prototype (which due to the shortened length may be viewed as a HEV rather than an EV traction design), the design in Figure 4-1 is equipped with a cheaper but poorer grade of Ferrite magnet, Ceramic 8, which has about only 70% of the coercevity of the FB9B grade, see Table 3-1. The performance of these two designs, in terms of demagnetization and the static torque, are simulated and compared in the following sections. Furthermore, the influence of changing the stack length on efficiency, power density, and power factor has been, separately, discussed in Appendix IV.

4.4.1 Demagnetization

The field strength across the Ceramic 8 magnets, under demagnetizing currents with amplitudes of 160%, 240% and 400% of the I_{pk} and comparing 39 mm and 195 mm stack lengths, has been simulated using FE 3D, and the results are shown in Figure 4-8. The red and yellow areas correspond to the regions exposed to full or partial demagnetizations, respectively.

(a)　　　　　　　　　　　　　　　(b)

(c)
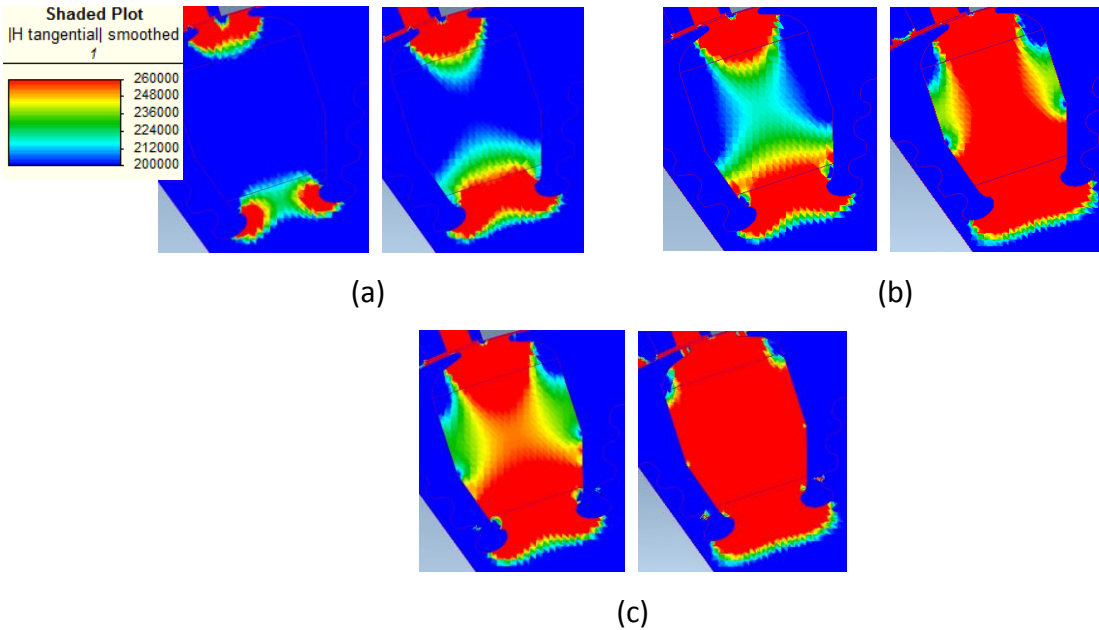
Figure 4-8: Field strength distribution in the Ceramic 8 magnets, for designs with 195 mm stack length (right column), and 39 mm stack length (left column), and under negative d-axis currents with different amplitudes. (a) 160% I_{pk}. (b) 240% I_{pk}. (c) 400% I_{pk}. All results correspond to middle stack faces.
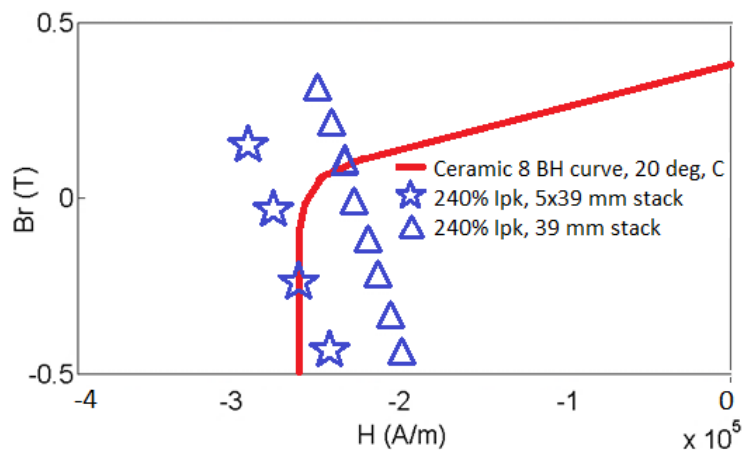
Figure 4-9: Demagnetization assessment using the proposed lumped circuit model, Ceramic 8 magnets, 240% I_{pk}.

As seen in Figure 4-8, following the proof of the concept in Section 4.3, the demagnetization performance is noticeably improved by shortening the stack length. Furthermore, confirming the explanation in Section 4.3, the improvement factor is larger for the larger short circuit currents, which, in case of the model in Figure 4-8, can be best observed for 240% I_{pk}, Figure 4-8(b), where the shortening of the stack length has reduced an 80% risk of demagnetization to less than 20% (the percentage is based on the demagnetized region divided by the full cross section of the magnet). The suitability of the lumped circuit model in Figure 4-6 is assessed by investigating the Figure 4-8(b) scenario, for which a good agreement with the FE 3D simulations has been achieved, Figure 4-9.

4.4.2 Static Torque

To evaluate the power density of the 39 mm stack length design with Ceramic 8 magnets, the static torque of this design using both Ceramic 8 and FB9B magnet grades is simulated and compared using 3D FE, Figure 4-10 (only 20% of the total electric loading is applied to match the prototype testing set-up in Chapter 8) . Comparing the peak torque values in Figure 4-10 it can be realized that despite the 14% higher remanent flux density of the FB9B grade, it only contributes to 4% higher peak torque/ power density. This is majorly due to the saturation of the laminations at the peak torque operating point, and suggests that the use of weaker and cheaper grade of magnets might not, necessarily, compromise the peak torque and power density of the machine.
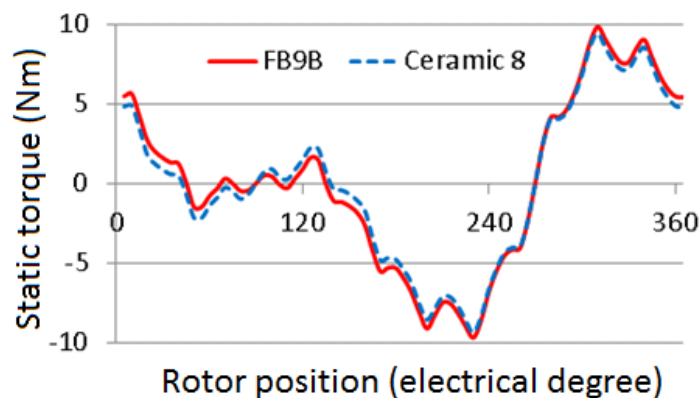
Figure 4-10: Comparison of the static torque for the 39 mm stack length designs using FB9B and Ceramic 8 magnet grades.

4.5 Formulation of the 3D concept

If the equation (4.5) is re-arranged with H_m as a function of B_m, an analytical expression to avoid the demagnetization risk can be obtained as in (4.6). In (4.6), the parameters γ and k_0 include the 3D effects from the stack length and magnetic saturation, while the other parameters, such as magnets width, number of turns and current amplitude are the state of the art parameters that are commonly used to mitigate demagnetization risk. The analytical expression (4.6) can be applied to enhance the conventional design optimization algorithms, while for most magnet grades, the B_{cj} (the magnet operating flux density corresponding to H_{cj}) can be approximated as zero.

$$\gamma. 2N.i/l_m + B_{cj}/k_0\alpha_0 < H_{cj} \qquad (4.6)$$

$$\gamma = R_{end,leak}/\left(R_{end,leak} + R_{lamination}\right) \qquad (4.6.1)$$

4.6 Conclusion

This chapter addressed the 3D demagnetization behavior of a ferrite based spoke type motor for an EV application. Based on a series of 3D FE simulations, analytical modelling, and prototype testing, it was shown that reducing the stack length might mitigate the demagnetization risk due to the increase of the stator laminations reluctance relative to the rather fixed end winding reluctance. Furthermore, it was shown that while the effect can be significant for the non-saturated conditions (due to an accelerated increase of the reluctance vs. stack length reduction), the effect might be, remarkably, pronounced for the saturated conditions due to the lower permeability of the laminations stack. The findings from the analyses have been summarized in a simple analytical expression, which can be applied to design optimization algorithms to mitigate demagnetization risks, and in particular to assist designing based on poorer and cheaper grade of magnets. This chapter has revealed, explained and quantified the impact of the stack length on the demagnetization resistance of the interior permanent magnet motors. Based on the findings, the cheap grade of magnets with poor demagnetization properties (such as the low grade of ferrite magnets) may be better utilized in designs with larger diameter to stack length aspect ratio.

5.1 INTRODUCTION

In this chapter, the high performance ferrite spoke design disclosed in Chapter 3, is, majorly, analysed with regards to an optimal choice of the rotor support material. The analysis includes a comparison of the motor multi-physical performance based on a few viable rotor support materials, in particular different grades of austenitic steels. The aim of the studies is to propose and assess the implications of using austenitic steel, as a cheaper, safer, and more widely available alternative to copper beryllium, suited to the low cost high performance nature of the intended ferrite motor design.

The contents in this chapter have led to the following publication and patent application:

▪ **M. Kimiabeigi**, J. D. Widmer, R. Long, Y. Gao, *et al.*, "On selection of rotor support material for a ferrite magnet spoke type traction motor," IEEE Trans. Ind. Applications, vol. 52, no. 3, pp. 2224-2233, Feb 2016.

▪ "Rotor structural means for high speed ferrite traction motor," by **M. Kimiabeigi** and J. Widmer, Patent application filed Jan 2016.

5.2 Ferrite Based Spoke Type Motor with a Distributed Winding

To cope with the high speed structural requirements of the motor design disclosed in Chapter 3, the rotor is composed of two parts which are joined via a fir tree root, Figure 5-1.
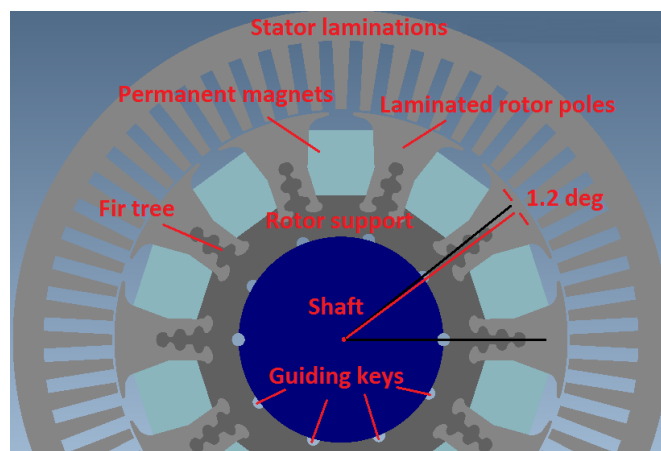

Figure 5-1: Spoke type ferrite motor design, 2D topology.

As a result of the multi-physical optimization in Chapter 3, it has been concluded that a spoke type design at the specified high speed levels need to be composed of a fir-tree and

rotor support structure, to cope with the high structural stress as well as fulfilling the maximum achievable power density (the fir tree design has superior magnetic performance compared to the single piece alternative, due to the less magnet leakage through the rotor yoke). With regards to the fir tree topology, based on the structural optimization, it was realized that the higher number of fir tree teeth, i.e. 6 vs. 3 teeth, results in slightly better structural performance, however the fewer number was, ultimately, selected due to its simplicity for the high volume manufacturing. It should be mentioned that due to the minor differences between the aforementioned numbers of the fir tree teeth in terms of the structural performance, more variations have not been investigated.

The rotor in Figure 5-1 is composed of five axial sections which are skewed in four steps, and according to an adopted pattern of ten guiding keys, Figure 5-1, half of which are distant by an angle equal to $360/P + \alpha/(m-1)$, (P is the pole number, α is the total angle of skew and m is the number of rotor axial sections, i.e. 5), while forming a diametrical symmetry with the remaining five keys (each of the five rotor sections is fitted to the shaft via a diametrical pair of the keys during the assembly, resulting in a complete four step skewed rotor). The aforementioned arrangement prevents the multiplication of the rotor segment parts as a result of the skew, and contributes to a lower manufacturing and assembly costs in a high volume production. Some other distinctive features of the rotor design in Figure 5-1 include the parallel sided magnets on top, which may allow for lower magnet tooling costs.

With regards to the stator, the windings are made of aluminium to save weight and cost, while the wires size and geometry are, optimally, chosen to maximize the slot fill factor, and minimize the AC losses during the high speed operation. A detailed investigation of the windings and comparison of the aluminium and copper in terms of the electromagnetic and loss performance have been provided in Chapter 7.

In the following sections, the influence of the rotor support material on the multi-physical performance and cost of the ferrite motor design in Chapter 3 is studied in details.

5.3 Rotor Support Multi-physical Requirements and Viable Material Options

5.3.1 Structural Considerations

5.3.1.1 Mechanical and fatigue properties

To achieve the optimal fir-tree design in Figure 5-1, a series of structural-magnetic optimizations have been made, using 2D FE tools; the objective was to control the peak

stress below the tensile and fatigue limits of the rotor pole and rotor support materials. A schematic illustration of a tensile stress-strain curve and the associated physical parameters are shown in Figure 5-2.

Some of the early generations of the fir tree design have been presented in Chapter 3, where some optimization outcomes such as increasing the bubble cut-out radius, or adjustment of the circumferential teeth height have been illustrated. Furthermore, based on the stress distributions in the rotor pole and the rotor support of the latest fir tree generation (with 3% work hardened austenitic steel chosen as the rotor support material, Figure 3-13), the maximum stress values in the poles and the rotor support are made to be within the acceptable fatigue limits of their respective materials.
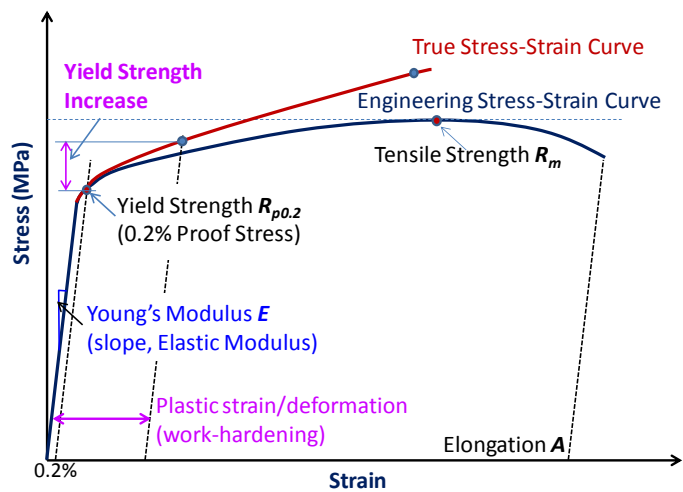
Figure 5-2: Illustration of tensile stress-strain curve.

5.3.1.2 Work hardening and Young's modulus

A metal's effective yield strength often increases after it has been subjected to a certain level of plastic deformation, e.g. 2–5% plastic strain. This is known as work hardening or strain hardening. The mechanism of the work-hardening-induced increase in effective yield strength is illustrated in Figure 5-2. From a structural point of view, work-hardening often brings about the same benefit as selecting a higher-strength material.

Another important mechanical property is Young's Modulus, or Elastic Modulus (E), see Figure 5-2. There is a little difference among steels of various kinds, having a Young's modulus value range of 185 – 210 GPa at room temperature. On the other hand, aluminium alloys have a much lower Young's modulus of ≈70 GPa; finally the copper beryllium can be ranked between the steels and aluminium, having a Young's modulus of ≈128 GPa.

Figure 5-3 shows the effects of Young's modulus and yield strength of various rotor support materials on another important rotor structural parameter, namely the radial expansion. High-speed rotor radial expansion will have a direct impact on a motor's operating rotor-stator air-gap. In the current study, radial expansion levels of a number of different rotor support materials, including austenitic 316L (non-work hardened and 3% work hardened) and a higher-strength Nitronic 50 stainless steel, a strong aluminum alloy 2024-T3, and finally copper beryllium were evaluated by finite element (FE) analyses. The speeds between 15 krpm to 18 krpm account for the 20% over speed requirement.

As can be seen in Figure 5-3, due to their lower Young's modulus, both aluminium (to higher degree) and copper beryllium (to lower degree) rotor supports would produce higher radial expansion levels than those of stainless-steel supports. Among stainless-steel rotor supports, radial expansions are similar until the rotor speed reaches about 16.5 krpm, when non-work-hardened 316 stainless steel starts to yield and cause the rotor radial expansion to increase sharply. Between the higher-strength Nitronic 50 and the work-hardened stainless steel 316L (with 3% plastic strain), there is very little difference in terms of rotor radial expansions. In fact, a more detailed examination indicates that the 3% work-hardened 316L produces a slightly lower rotor radial expansion than that of a Nitronic 50 rotor.
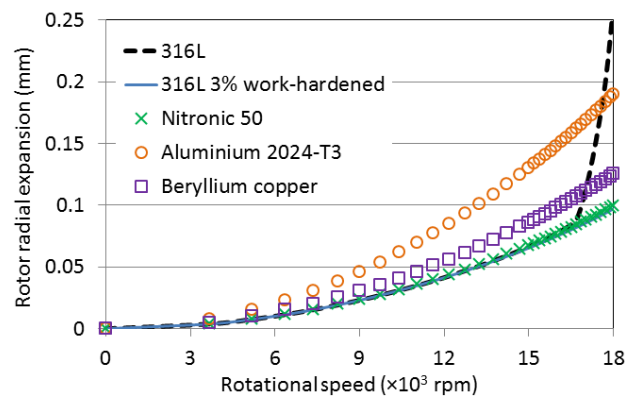
Figure 5-3: Comparison of rotor radial expansions for various rotor support materials.

5.3.1.3 Potential issues with work hardened stainless steels

The strength increase due to work hardening is not always stable, especially if the material is to be exposed to elevated temperatures. In addition, work-hardening may lead to changes in other aspects of the material, such as in microstructure and in other physical and magnetic properties. One potential issue with work-hardening of austenitic steels is the risk of regaining some magnetism. This is due to partial transformation of austenitic phase into

martensite as a result of plastic deformation, [109]. The level of regained magnetism depends on the steel grade, plastic strain levels and, ultimately, on the chemical composition and homogeneity of the material, [110].

For the current rotor design and based on the plastic deformation and fatigue endurance requirements, a rotor support material with minimum yield strength and fatigue limit (fully-reversed cyclic loading) of, respectively, 290 MPA and 270 MPa is needed. The yield strength limit is based on the strain calculations in the materials and the requirement to avoid permanent deformation under zero to 18 krpm over-speed requirement; Figure 5-3 illustrates an example of an excessive plastic deformation in the non-work hardened 316L steel rotor support due to its insufficient yield strength. Furthermore, the indicated fatigue limit is based on the cyclic stress variation in the rotor support under normal operational range of speed, i.e. zero to 15 krpm, and according to the number of cycles to failure data of the material, [81], it ensures a rotor life time longer than the expected life time of the vehicle.

These requirements are slightly above the capability of non-work hardened 316L steel. The UTS and yield strength of some grades of austenitic steels, with and without work-hardening, are summarized in Table 5-1, [111]. Furthermore, in Figure 5-4 the magnetic permeability of these grades for different levels of work hardening is shown, [112], where a homogenous material composition has been assumed. From Table 5-1 and Figure 5-4, it can be realized that: a) In the case of 302 and 304 austenitic steels by small to medium levels of work-hardening (up to 40%), the mechanical property of the steel can, significantly, be improved, while no regain of magnetism is expected; b) In the case of 316L grade, while the mechanical property can, significantly, be improved by work-hardening, the martensitic phase conversion is quite negligible, even for very high levels of work-hardening.

Table 5-1

Change of UTS and yield strength vs. work hardening, [111].

	Percentage of work hardening					
	0	10%	20%	30%	40%	50%
302 SS						
Tensile	642	745	842	952	1049	1159
Yield	255	628	738	828	925	1014
304 SS						
Tensile	593	676	780	897	1007	1090
Yield	235	476	738	828	932	1001
316L SS						
Tensile	587	656	759	897	980	1035
Yield	262	483	676	814	883	945
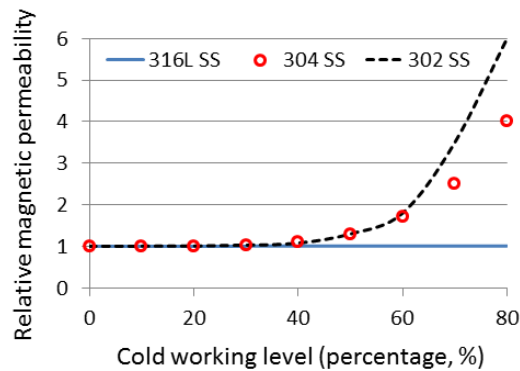
Figure 5-4: Change of magnetic permeability vs. work hardening [112].

5.3.2 Magnetic Analysis

To assess the effect of rotor support magnetic property on the motor performance, the maximum torque at base and top speed, and assuming different magnetic permeability for the rotor support component, was calculated using 2D FE simulation, and shown in Figure 5-5. As illustrated in Figure 5-5, it can be realized that even for a small increase in magnetic permeability of the rotor support, the maximum torque capability of the motor might be significantly reduced, due to the excessive flux leakage through the rotor support. However, as explained in Chapter 5.3.1, due to the very low level of work-hardening required to achieve the requirements of the rotor design in Figure 3-13, most grades of the

austenitic steel are expected to fully retain their non-magnetic property, resulting in no degradation of the electromagnetic performance.
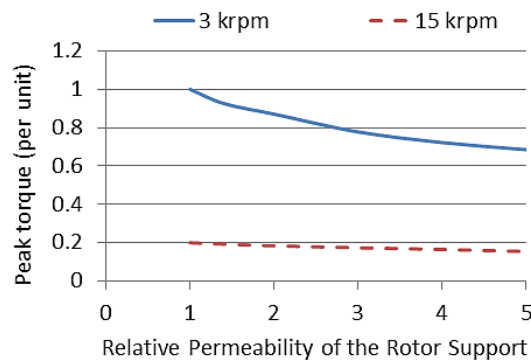
Figure 5-5: Peak torque capability at base and top speed vs. rotor support permeability.

5.3.3 Thermal Performance

5.3.3.1 Electromagnetic losses

The electromagnetic losses in the rotor of a PM machine are due to the magnetic field harmonics that rotate asynchronously to the rotor. As reported in [87], the designs with fractional slot windings are known to experience higher rotor losses compared to those with distributed windings, due to the rich Magneto Motive Force (MMF) harmonic and sub-harmonic contents inherent in this type of windings.

(a)   (b)
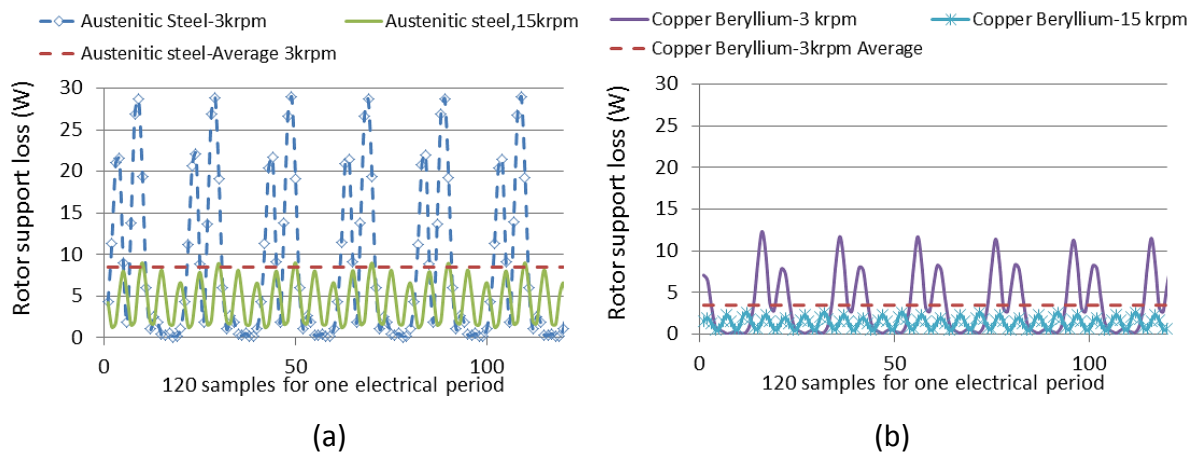
Figure 5-6: Rotor support losses for the peak power operating points at 3 krpm and 15 krpm rotor speeds. (a) Austenitic steel rotor support. (b) Copper beryllium rotor support.

The rotor support losses for both copper beryllium (conductivity of $1.16 * 10^7 \ S/m$), and austenitic steel (conductivity of $1.4 * 10^6 \ S/m$) have been calculated using FE 2D. In these calculations, the rotor support is assumed as a solid conductor piece, and only the z-axis

component of the eddy currents is taken into account. Based on the results in Figure 5-6, despite the higher conductivity of the copper beryllium, its associated average rotor support loss at both base and top speeds is about half the loss of the austenitic steel. The lower loss associated with the copper support can be attributed to the shielding effects as a result of the higher conductivity and smaller skin depth. Furthermore, for both materials the loss at the top speed is lower than that at the base speed, suggesting the loss is mainly driven by the armature MMF (rather than slotting effects). Despite the theoretical interests, for both materials the rotor support loss is quite negligible, i.e. 4-8 watts, suggesting that regardless of the material choice the rotor support loss has negligible electromagnetic or thermal implications.

An illustration of the loss in the austenitic steel rotor support (at a rotor position corresponding to the maximum loss) is given in Figure 5-7, from which it can be realized that the losses are largest in the regions beneath the magnets where the maximum variation of the flux occurs. Furthermore, an illustration of the mesh elements for the copper beryllium support, and considering the 12th harmonic component, from Figure 5-6, at 15 krpm, has been provided in Figure 5-7 (b). As shown in Figure 5-7, to improve the computation accuracy, the element dimensions are chosen to be less than one-fourth of the minimum skin depth.

| (a) | (b) |
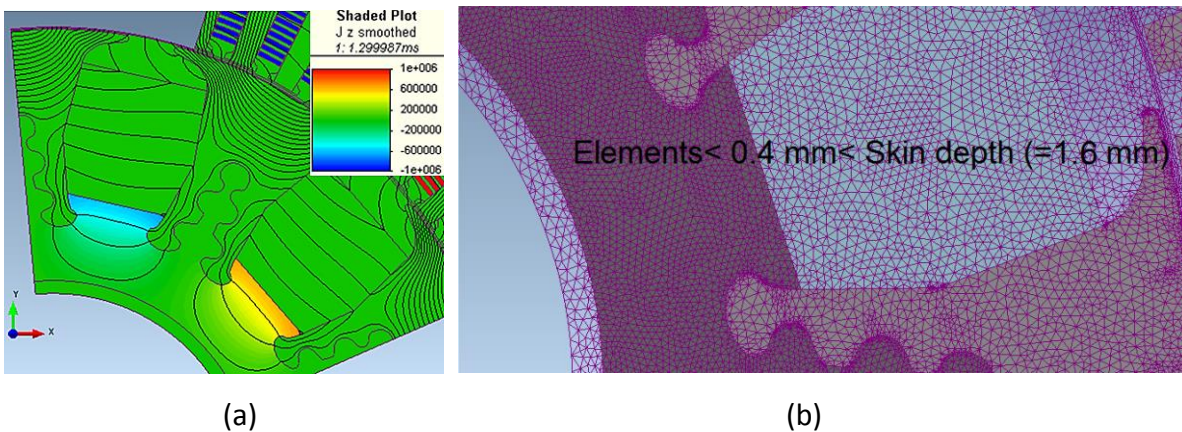
Figure 5-7: (a) Rotor support eddy current loss distribution (A/m^2) under peak load and 3 krpm operation, austenitic steel. (b) Illustration of mesh elements for Copper beryllium support at 15 krpm.

5.3.3.2 Cooling

Due to the higher thermal conductivity of the copper beryllium compared to the Austenitic steel (200 *W/m.K* vs. 15 *W/m.K*), the former might be a preferable option in designs where

liquid cooling via the shaft, such as in [46], is intended. However, in designs with other methods of cooling, such as the one in Chapter 3, where the source of heat exchange is located on the external stator frame, the thermal characteristics of the rotor support would have minimal influences on the general thermal performance. To demonstrate this, the stator winding and the magnet temperatures are simulated at two representative operating conditions, Figure 5-8: a) a continuous operation at 60 kW and 10 krpm (i.e. a relatively, high power and high speed) to represent a severe thermal loading, and b) a continuous operation at 10 kW and 6 krpm (a key operating point according to the vehicle drive cycle) to represent a thermal loading that determines the motor efficiency. The thermal analysis has been performed using a lumped circuit modelling method in the Motor Cad software, [113, 114]. As seen in Figure 5-8, the thermal behaviour is, almost, identical for the two rotor support materials. It should be noted that in [34], even though no direct shaft cooling is applied, the rotor support material is kept the same as in [46], i.e. copper beryllium; this choice would impose an unnecessary high cost penalty that will be discussed in Section 5.3.4.
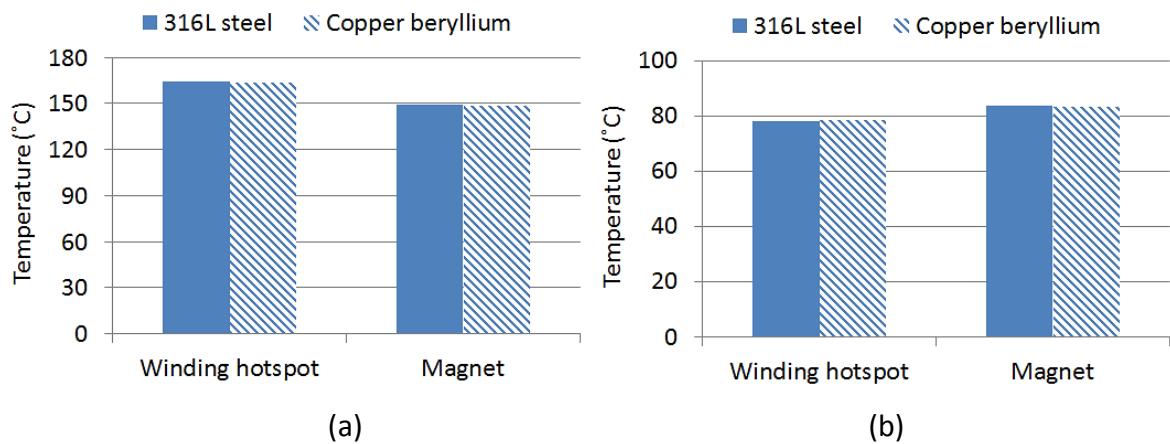
Figure 5-8: Effect of rotor support material on the winding and magnet temperature.
(a) Continuous operation at 60 kW, 10 krpm. (b) Continuous operation at 10 kW, 6 krpm.

5.3.4 Cost

A major motivation for ferrite based designs is to reduce the overall cost of the motor. Thereby, careful material selection must ensure that such designs do not lose their competitiveness against rare-earth magnet alternatives. The costs of the rotor support for different grades of steel and copper beryllium have been quoted and estimated based on several sources including [83], [115-117], assuming a volume production of 100,000 motors per year, and are normalized based on the cost of the ferrite magnets used per motor

volume; the results are shown in Figure 5-9. With regards to the copper beryllium, the price is based on ~2% contained beryllium, while the final product price (in contrast to the raw material price indicated in [20]) has been considered. Furthermore, based on the quotes from different sources a rather large variation of the price can be obtained.

Based on Figure 5-9, it is clear that, a) the cheapest option that fulfils the structural requirements in Section 4.3.1, is the 3% work hardened 316L austenitic steel, the cost of which is 120% of the cost of the ferrite magnets, b) work hardened steel is significantly cheaper than using a stronger grade of steel, such as Nitronic 50, and c) the copper beryllium can be 3-6 times more expensive than the proposed austenitic steel option (depending on the steel grade and subject to variation of quotes), and, can constitute a cost up to 600% of the total magnet costs, which might compromise the performance per cost competitiveness of the ferrite based designs.

Finally, it should be mentioned that along with the selection of the rotor support raw material, care must be taken to avoid costly manufacturing techniques. Due to the excellent forming quality of the copper beryllium, it can be extruded to the required shape. In case of the steel, due to the limitations of extrusion and high costs of machining, alternative manufacturing methods such as laminating and stacking should be sought.
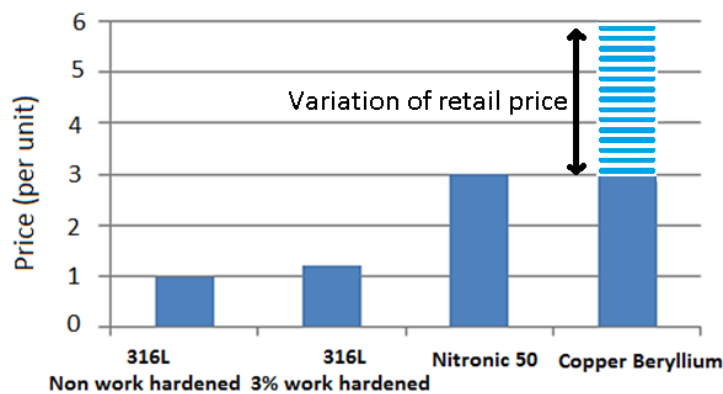
Figure 5-9: Price comparisons for the different rotor support materials.

5.4 Conclusion

In this chapter, a multi-disciplinary investigation of the rotor support material as part of a low cost high performance ferrite motor has been presented. The high-speed rotor structural performance was shown to benefit from the use of non-magnetic metals of higher Young's modulus and yield strength, especially austenitic stainless steels. A work-hardening

treatment to the rotor support material also proves to be desirable. It was shown that even a small degree of work hardening can strengthen most grades of stainless steel to fulfil the structural demands of the proposed motor design, without a noticeable change of the magnetic permeability and electromagnetic performance of the motor. Despite the higher thermal conductivity of the copper beryllium compared to austenitic steels, its thermal advantages are minimal when distributed windings are used, and/ or cooling means other than direct rotor shaft cooling are applied. In terms of cost for high volume production, it was shown that the austenitic steel can be 3~6 times cheaper than the state of the art, which may, significantly, boost the cost competitiveness of the low cost ferrite motors. The findings of this chapter are expected to provide a better insight for the designers on how the material characteristics of the rotor support component may influence the multi-physical performance and cost of a fir tree based ferrite traction motor, in particular, when designing for a high volume production.

5.5 Acknowledgement

Chapter 6 COMPARISON OF A SINGLE PIECE AND A FIR TREE BASED SPOKE TYPE ROTOR DESIGN FOR LOW COST ELECTRIC VEHICLE APPLICATION

6.1 INTRODUCTION

In this chapter, a high speed and high power density spoke type design based on a single piece rotor topology, and considering both the magnetic and structural requirements of a high performance low cost EV application is presented. The performance of this rotor topology is, for the first time, compared against a fir-tree based alternative solution targeting the same sets of design requirements and constraints, Chapter 3. Based on these comparisons, the pros and cons of the two design solutions, in terms of the power density, efficiency, demagnetization and cost is discussed.

The contents in this chapter have led to the following publications and patent application:

- "Single piece spoke type rotor for electric vehicle applications," by **M. Kimiabeigi**, R. Long, A. Michaelides, filed Jan 2016.

- **M. Kimiabeigi**, R. Long, J. D. Widmer, *et al.*, "Comparative Assessment of Single Piece and Fir Tree Based Spoke Type Rotor Designs for Low Cost Electric Vehicle Application," IEEE Trans. Energy. Convers, Feb 2017, DOI: 10.1109/TEC.2017.2662579.

- **M. Kimiabeigi**, J. Widmer, A. Michaelides, Low cost high performance ferrite motors with aluminium windings, Advanced E-Motor Technology-IQPC conference, Berlin 2016.

6.2 Background and Motivation for Study

In Chapter 3, a spoke type design with a distributed winding is proposed and shown to marginally meet the requirements in Table 3-1. Despite the high performance of this design, the proposed rotor is made of two parts including the magnetic rotor pole segments and the non-magnetic rotor support, which are coupled together via a so-called fir tree feature. Due to the additional costs associated with the extra rotor components, and corresponding manufacturing and assembly process, the two-part rotor design might lose some of its cost competitiveness. Therefore, in this chapter, a rather simpler rotor topology consisting of a single ferromagnetic piece has been investigated. In the following sections, the design and performance of the single piece rotor topology in terms of the electromagnetic and structural performance are addressed and evaluated against both the target requirements and the design with the fir-tree based rotor topology, and conclusions are drawn.

6.3 Design and Analysis

6.3.1 Power Density and Structural Performance

Due to the same packaging requirements as the fir-tree based design and to highlight the differences on the rotor part design only, the single piece rotor design is based on the same stator and rotor dimensions as have been provided in Table 3-2. To maximize the output torque of the motor, while maintaining the rotor stress below the limits chosen for the rotor strength, deformation and durability (based on M270-35A non-grain oriented electrical steel), a combined electromagnetic and structural optimization of the rotor was performed, as a result of which the rotor topology in Figure 6-1(a) was obtained.

With regards to the magneto-structural optimization, a linear-elastic, multi-objective optimization was performed, which targeted at achieving a minimum rotor pole mass, at a specified maximum stress and radial deflection limit, as well as a set minimum thickness of the rotor bridges to respect the manufacturing feasibility, Figure 6-1(b). This topological optimization is based on a so-called stress constrained mass minimization technique, which although known to the structural and civil engineering, is not commonly applied in the context of electrical machine design; a more detailed description of the technique has been provided in Appendix VI. The structural optimization was, further, guided with the electromagnetic simulations, based on which the flux barriers were concentrated in two proposed generic zones, namely the two main cavities beside and underneath the magnets, where particular attention was paid to maximize the reluctance of the magnetic leakage path, and leaving the q-axis flux path undisturbed (to maximize the saliency), Figure 6.1(c). The topology solution was, then, evaluated by a non-linear-plastic simulation, where finer design adjustments have been implemented. On this basis, the optimizations can be said to consist of two objectives, namely mass and torque/ power density. With regards to the torque/ power, only two corner points corresponding to the peak torque at base rotor speed, and peak power at top rotor speed have been considered, while for each calculation the current advance angles have been fine tuned to achieve a maximum/ optimal torque/ power value.

(a)

(b)

(c)
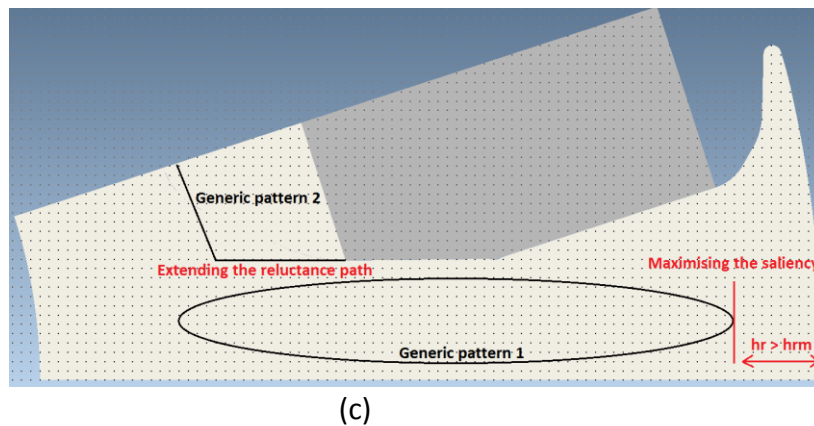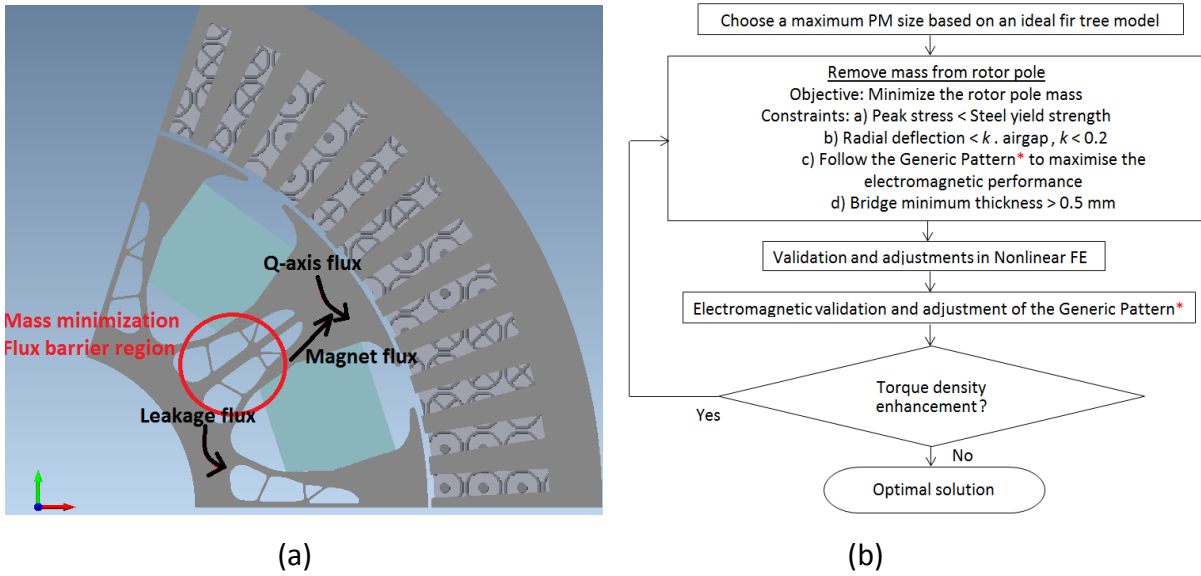
Figure 6-1: The proposed single piece rotor topology for high speed high torque density traction application. (a) Topology. (b) Optimization algorithm. (c) Illustration of rotor mass minimization.

The stress distribution in the rotor for the fir tree based design in Chapter 3 and the optimized single piece topology in Figure 6-1, have been compared in Figure 6-2, where it is realized that for a same rotor pole material, the fir tree design may outperform the single piece design by about 19% lower peak stress. Furthermore, the magnetic field distribution in the single piece rotor design and the peak torque at base and top speed have been assessed in 2D FE, Figures 6-3 and 6-4, based on which it is realized that due to a higher magnetic loading (lower magnet leakage) the fir tree design outperforms the single piece rotor by providing ~20% higher peak torque and power density at the base and top speed.

With regards to the magnet contribution to the BEMF under no-load conditions and the peak torque, it should be noted that due to the presence of the armature d-axis flux in the

bridges and the intensified magnetic saturation, Figures 6-3(a) and (b), the magnet leakage is lower under the loaded conditions; thereby a larger contribution of the magnets to the peak torque compared to the BEMF, and a larger deviation between the BEMF and the peak torque must be envisaged.

(a)   (b)
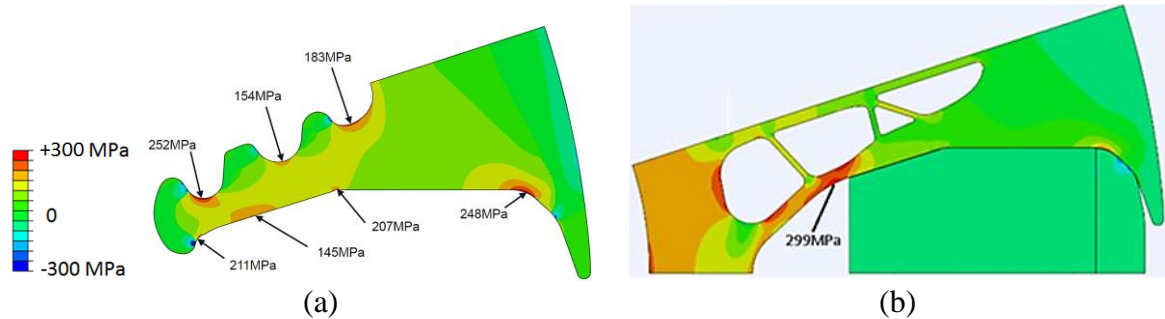
Figure 6-2: Stress distributions at 15 krpm for fir-tree and single piece rotor design. (a) Fir tree based rotor pole. (b) Single piece rotor.

(a)   (b)
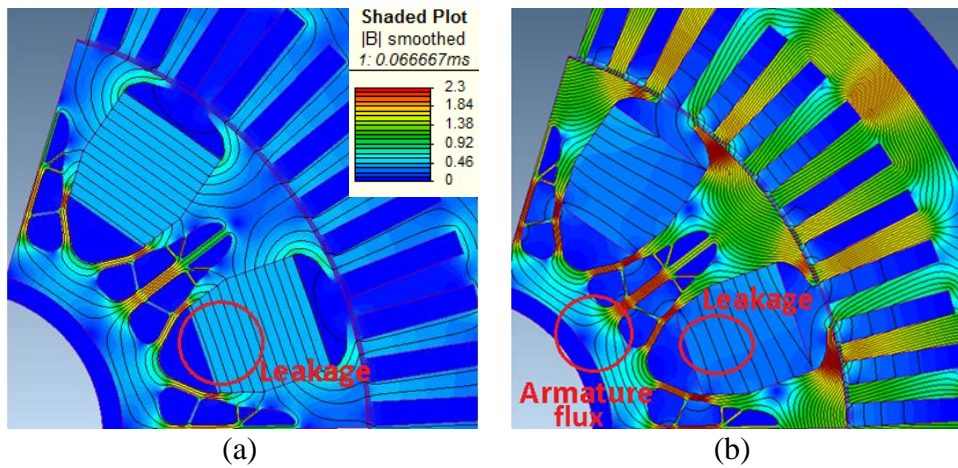
Figure 6-3 Flux lines and flux density in the single piece rotor design, and illustration of magnet leakage ratio. (a) No load. (b) Peak torque at 3 krpm.
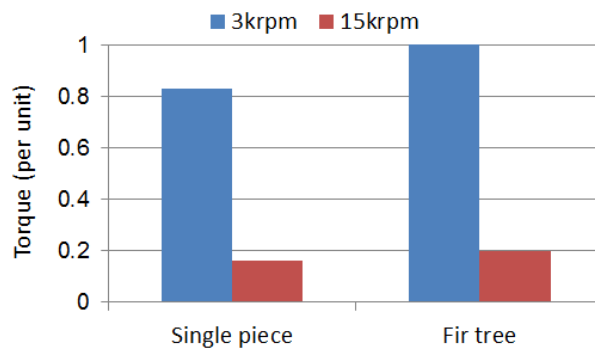
Figure 6-4: Comparison of the single piece and fir tree rotor in terms of peak torque at base and top speed.

6.3.2 Demagnetization

The demagnetization of the ferrite magnets during field weakening or, more critically, under short circuit faults is one of the major risks of the ferrite based traction motors. The currents of the single piece design under a 3-phase short circuit fault (occurring after one full electrical period of re-generative peak torque operation) have been simulated in 2D FE and shown in Figure 6-5. From Figure 6-5, it is realized that the peak short circuit current is about 160% of the I_{pk}, which is about the same amplitude for the fir-tree based design in Chapter 3.

The field strength, H, distribution in the rotor and under the worst instant during the 3-phase short circuit fault (i.e. when I_b reaches its peak value in Figure 6-5), has been simulated for both the single piece rotor and the fir tree design in 2D FE, and the results are shown in Figure 6-6. The red areas indicate the regions where the H field is greater than the intrinsic coercivity of the FB9B grade Ferrite magnet at 20˚C, and therefore complete demagnetization may be expected. From Figures 6-6 (a) and (b) , it can be realized that, even though due to the similar rotor topology near the airgap region, the demagnetization risk for the two designs is identical, for the inner parts of the rotor the location of the maximum field and thereby risk of demagnetization is different. In this regard, for the single piece rotor lamination the maximum demagnetization field occurs near the magnet bottom edge with highest flux concentration, whereas for the fir-tree based model the maximum field occurs further away from the magnet and in the pole shoe tips.

For a clearer comparison of the two designs and to assess the performance under more severe demagnetization conditions such as asymmetrical short circuits, [69], a higher demagnetization current, equal to 400% of the I_{pk}, has been applied, and the H distribution has been simulated and shown in Figures 6-7(a) and (b). From Figures 6-7(a) and (b), it can be realized that the demagnetization resistance of the single piece rotor model may, significantly, exceed that of the fir tree model, as the inner magnet regions are prone to lower demagnetization risk. This is mainly due to the ferromagnetic leakage flux path adjacent to the inner part of the magnets in the single piece rotor model in contrast to the air void leakage flux path in the fir tree based model; where as a result of the lower magnetic reluctance path in the single piece model, the demagnetization field is better bypassed and the magnets are less affected.
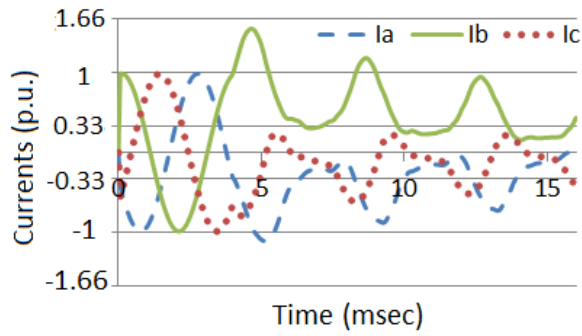
Figure 6-5: 3-phase short circuit currents for the single piece design.

(a) (b)
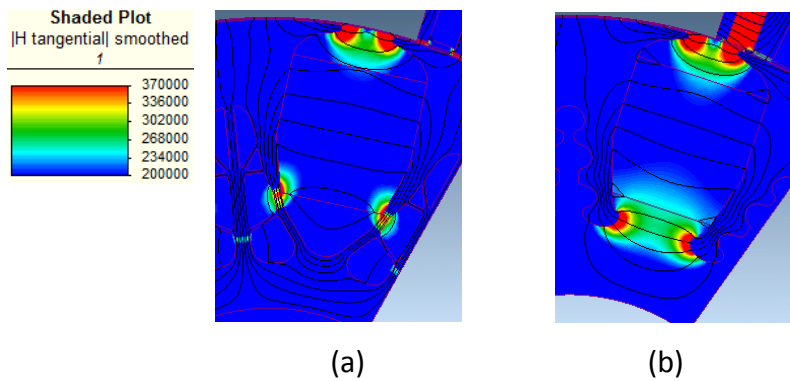
Figure 6-6: Demagnetization risk assessment (H distribution) under 160% Ipk in negative d-axis location and FB9B magnets. (a) Single piece trial design. (b) Fir-tree based design.

(a) (b)
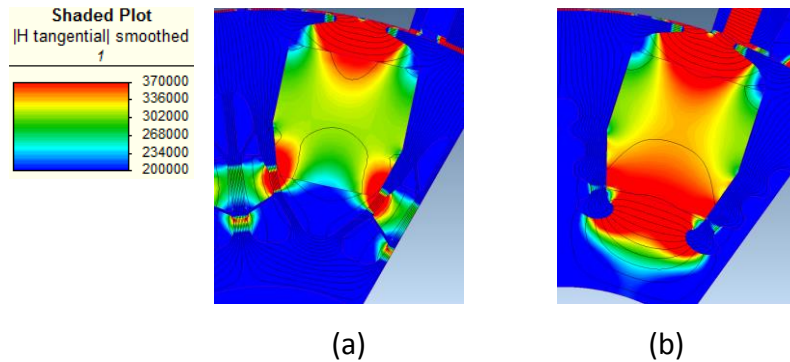
Figure 6-7: Demagnetization risk assessment (H distribution) under 400% Ipk in negative d-axis location and FB9B magnets. (a) Single piece trial design. (b) Fir-tree based design.

6.3.3 Losses and Efficiency

To compare the efficiency of the single piece rotor model against that of the fir tree model, the winding and iron losses under whole range of torque-speed operating points have been calculated. The iron loss calculation has been based on the open circuit and short circuit modelling in FE 2D and using the computationally efficient technique disclosed in [113] and [114]. With regards to the winding DC loss, a copper winding with slot fill factor of 45% and

at 120 ˚C has been considered. The windings AC loss was, also, calculated in FE 2D and the maximum AC+DC to DC loss ratio (at 15000 rpm) was obtained equal to 1.4 for both rotor designs. Due to the similar AC loss factor for the two rotor designs and its relatively small value for the most of the operating speed range (the AC loss is proportional to the inverse of the speed), only the DC part of the winding loss has been included in the efficiency map calculations, Figure 6-8.

Based on Figure 6-8, the peak efficiency of the fir tree model is about 3% higher than the single piece model. This efficiency superiority covers the majority of the torque-speed envelope, including the two key operating points at which the vehicle and the motor will most frequently operate (one corresponding to the urban driving, and one corresponding to the highway cruising). To explain the difference between the efficiency map of the two designs, the stator currents associated with the efficiency maps in Figure 6-8, have been calculated (based on maximum torque per ampere function and using an optimal advance angle at each operating point) and shown in Figure 6-9. Comparing Figure 6-9 to Figure 6-8, it can be realized that due to the lower magnetic loading in the single piece design (due to higher magnet leakage and lower magnet utilization), a higher current loading (resulting in higher winding loss) is required to achieve the same level of torque and power at each operating point. Furthermore, due to the lower BEMF levels in single piece model, lower field weakening and d-axis currents are required at higher speed range. As a result, the efficiency (comparing to the fir tree design) is slightly improved at the high speed corner of the torque-speed spectrum.


(a)   (b)
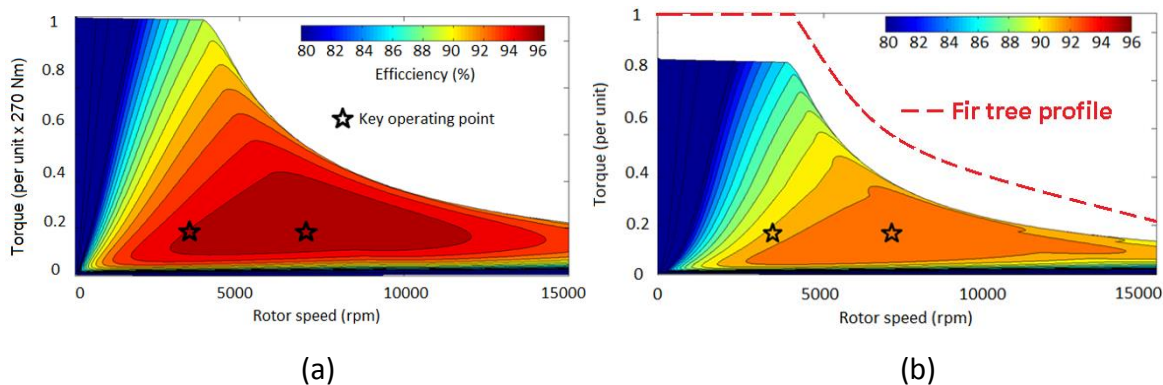
Figure 6-8: Efficiency map for complete torque-speed profile. (a) Fir tree based model. (b) Single piece model.

70
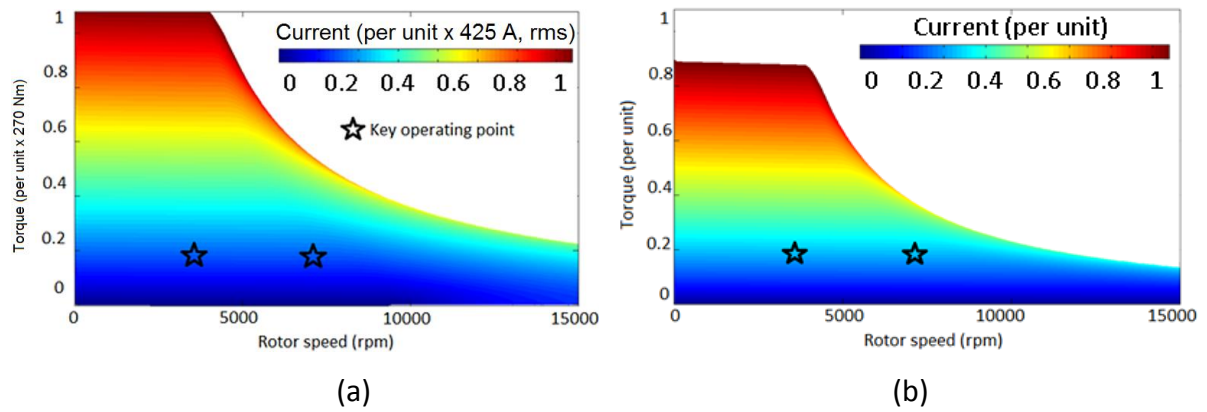
Figure 6-9 Distribution of current over torque-speed profile. (a) Fir tree based model.

(b) Single piece model.

Finally, with regards to the iron losses in the rotor, it is worth mentioning that the two rotor designs show only minor differences (up to maximum difference of 20%) at different operating points. However, the effect of manufacturing on the lamination B-H properties is expected to be more severe in case of the single piece rotor design (due to higher number of cavities and thinner bridges in the lamination), which requires a detailed prototype level investigation.

6.4 Discussions

Based on the analysis provided in the previous sections, the fir tree design may outperform the single piece design in terms of the power density and efficiency. However, the extra components in the fir tree alternative are likely to increase the manufacturing and material cost associated with this type of design, as a result of which, the single piece alternative might become more competitive in terms of the performance per unit cost.

This chapter has compared the performance of the two alternative topologies against the same and specific requirements for a high-speed, high-power traction motor. Considering a different set of requirements, which are more suited to the single piece design, the performance gap between the two topologies is likely to reduce, which would, further, improve the performance per cost index of the single piece design. It is estimated that a motor requiring a lower top speed would favour the single piece design due to smaller centrifugal forces, as a result of which narrower bridge, thereby, lower flux leakage and larger torque densities may become achievable.

With respect to the fine single piece rotor design features, namely the thin lateral branches in Fig. 1(a), it should be noted that whilst these features proved to enhance the single piece

71

rotor design performance, they may add to the manufacturing complexity and costs. Furthermore, the influence of the material deterioration due to the machining process has to be accounted for. In this regard, since the rotor losses are negligible, the manufacturing anomalies may result in lower magnetic permeability in the bridges, thereby reducing the leakage and enhancing the electromagnetic performance of the motor overall. For a high volume production the fine features might need to be, partially or fully, compromised, leading to a loss of the electromagnetic performance. Furthermore, with respect to the magnets volume, it should be noted that whilst increasing the magnet volume might increase the magnetic loading and better electromagnetic performance, it is limited by the peak stress in the rotor pole via the centrifugal force proportionality, (6.1), m corresponding to the magnet and rotor mass per pole, r the radius of the center of gravity, and ω the angular velocity of rotor. As a result, whilst for the given design constraints in this chapter, namely the rotor top speed and radius, the allocated magnet volume cannot be further increased (as the stress levels are, already, higher than the fir tree equivalent design and close to the steel maximum limit), it is envisaged that designs with a lower top speed might be favourable, as a radially longer magnet and a higher magnetic loading might be achievable.

$$\sigma \propto m.r.\omega^2 \qquad\qquad (6.1)$$

6.5 Conclusion

In this chapter, a high speed and high power density traction motor using ferrite magnets and following a single piece rotor topology has been disclosed, and was compared against an alternative design based on a fir tree rotor topology. Based on the analyses, the fir tree rotor outperforms the single piece option in terms of the power density and the efficiency due to a better utilization of the magnets, while, the latter demonstrates better demagnetization performance due to a higher leakage in the direct axis (d-axis) region. It should be noted that the addressed single piece design has been pushed to its ultimate magneto-structural limits to assess the maximal potential of such a design vs. a fir tree alternative; therefore, in practice, a larger performance gap between the two designs can be envisaged. Due to the fewer components involved with the single piece design, this option may match the fir tree version in terms of the cost per output power, when design for high volume is considered. Furthermore, reducing the top speed requirement may improve the single piece design

competitiveness, as larger magnets and, therefore, higher torque densities may become achievable.

Finally, it should be noted that whilst in this thesis only one grade of lamination, i.e. M270-35A has been studied, applying a stronger grade in the rotor can assist to obtain a higher structural performance, which may, in turn, result in higher power density and higher efficiencies.

6.6 Acknowledgement

The structural design and analysis in Section 6.3.1 has been performed in collaboration with Raymond Long and Yi Gao from Tata Steel, UK.

Chapter 7 : ON THE WINDING DESIGN OF A HIGH PERFORMANCE FERRITE MOTOR FOR TRACTION APPLICATION

7.1 INTRODUCTION

In this chapter, the performance of the ferrite motor design in Chapter 3, with regards to the stator windings will be assessed. In this regard, the distributed wound stator is compared against a concentrated wound alternative, while the rotor in both cases is kept identical to the base line rotor design in Chapter 3. First, the torque-speed characteristic of the motor, using the two alternative windings, is compared. Then, the AC winding losses for different scenarios including concentrated vs. distributed topology, different slot fill factor, random vs. organized wire lay-out, copper vs. aluminium, and star vs. delta connection have been evaluated. As a novel contribution of this chapter, the significance of an organized wire layout vs. a random layout in terms of the impact on the AC losses is highlighted, while it is shown how maximizing the slot fill factor might, adversely, raise the AC losses in a winding. Furthermore, the advantage of using aluminium wires in terms of a more balanced current distribution and a lower risk of hot spot formation is, for the first time, demonstrated.

The contents in this chapter have led to the following publications:

- **M. Kimiabeigi**, J. Widmer, R.S. Sheridan, R. Harris, A. Walton "Design of high performance traction motors using cheaper grade of materials", IET International Conference on Power Electronics, Machines and Drives (PEMD), 2016.

- **M. Kimiabeigi** and J. Widmer, "On the Winding Design of a High Performance Ferrite Motor for Traction Application", International Conference on Electrical Machines (ICEM), 2016.

- **M. Kimiabeigi**, J. Widmer, A. Michaelides, Low cost high performance ferrite motors with aluminium windings, Advanced E-Motor Technology-IQPC conference, Berlin 2016.

7.2 Torque and Power Performance

The key requirements and geometrical data of the high speed ferrite motor analysed in this chapter have been provided in Chapter 3, Table 3-1. Furthermore, a schematic of the stator and rotor geometry for both a distributed winding (with 2 slots per pole and phase) and a concentrated winding (with 0.5 slot per pole and phase) as well as some major dimensions are included in Figure 7-1 and Table 3-2. With regards to the design methodology, the following comments should be noted: a) the rotor geometry is a result of a coupled electromagnetic-structural optimization process which has been explained in Chapters 3, 4, and 5, b) the stator topology with the distributed winding is the result of an optimization to achieve maximum torque, and a minimum ripple torque, while the open rectangular slots were chosen to maximize the flux linkage and simplify coil insertions, c) the stator topology with the concentrated winding is the result of an optimization, to achieve a maximum torque while the outer and inner bore diameters were kept fixed and identical to the design with the distributed winding (to apply the same rotor and the same packaging constraints for a better comparison). Furthermore, the stack length of the design with the concentrated wound stator was increased from 195 mm to 255 mm to utilize the additional space due to the shorter end windings (15 mm concentrated vs. 45 mm distributed on each end).

To evaluate the performance of the motor at the base and top speed, a 2-dimensional Finite Element (2D FE) was used, where the drive was modelled using a sinusoidal current source with the maximum line to line voltage fixed to 400 V. The voltage and current waveforms for the two alternative windings at 3000 rpm and 15000 rpm, as well as the peak torque and power vs. speed curves for the entire speed range are shown in Figures 7-2, 7-3 and 7-4, where U_{aN} and U_{ab} correspond to line to neutral and line to line voltages, respectively. To explain the findings, the direct (L_d), quadrature (L_q) axis inductances and saliency ratio (L_q/L_d) vs. the current have been calculated using FE 2D and the standard phasor diagram method, [118] (7.1) and (7.2), where v_d, i_d, v_q, and i_q are the d-axis and q-axis voltage and currents, λ_m is the magnet flux linkage, and r_s and ω_r are the winding resistance and rotor speed (*rad/ sec*), the results are shown in Figure 7-5.

$$v_q = r_s \cdot i_q + w_r \cdot (L_d \cdot i_d + \lambda_m)$$

(7.1)

$$v_d = r_s \cdot i_d - w_r \cdot L_q \cdot i_q$$

(7.2)
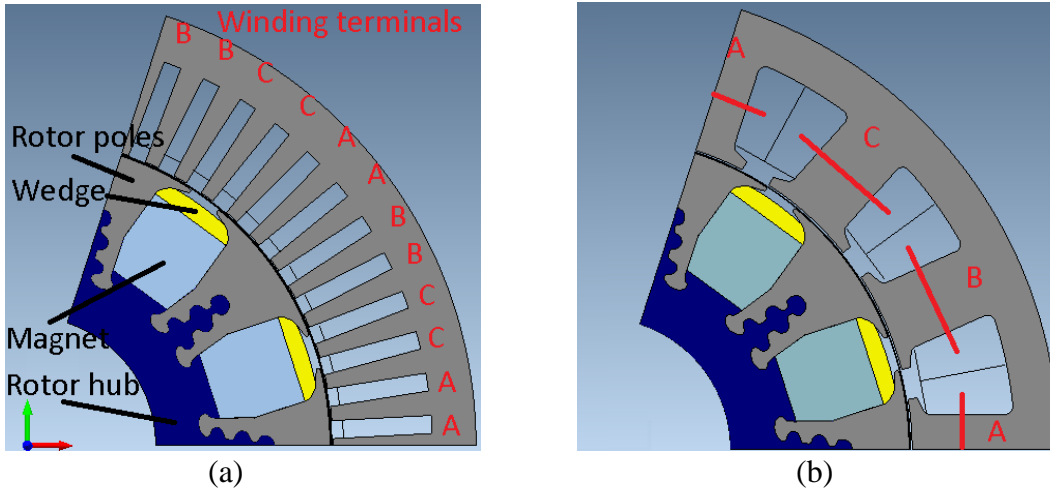
Figure 7-1: Schematics of high speed ferrite motor. (a) Distributed winding, Motor stack length=195 mm. (b) Concentrated winding, Motor stack length=255 mm.

From Figures 7-2 to 7-5, it can be realized that: a) due to the higher per unit inductance associated with the concentrated winding (due to the additional Magneto Motive Force, MMF, harmonics), for a voltage limited application such as traction, the base speed is lower compared to the distributed winding, while for the speeds above the base speed, lower currents and, thereby, lower torque compared to the distributed winding design, can be achieved, b) in the constant torque region, the concentrated winding design provides lower peak torque, due to the lower saliency ratio as well as lower winding factor, i.e. 86.6% vs. 96.6% for the distributed winding design, c) despite the lower peak power, the concentrated winding design may provide a competitive or, even, higher constant power speed ratio (*CPSR*) compared to the distributed winding design; this is due to the larger per unit L_d (which enables the field weakening with lower available per unit current), as well as improvement of the concentrated winding design saliency by approaching the high speed- low current operating range, Figure 7-5(b), due to the lower magnetic saturation.
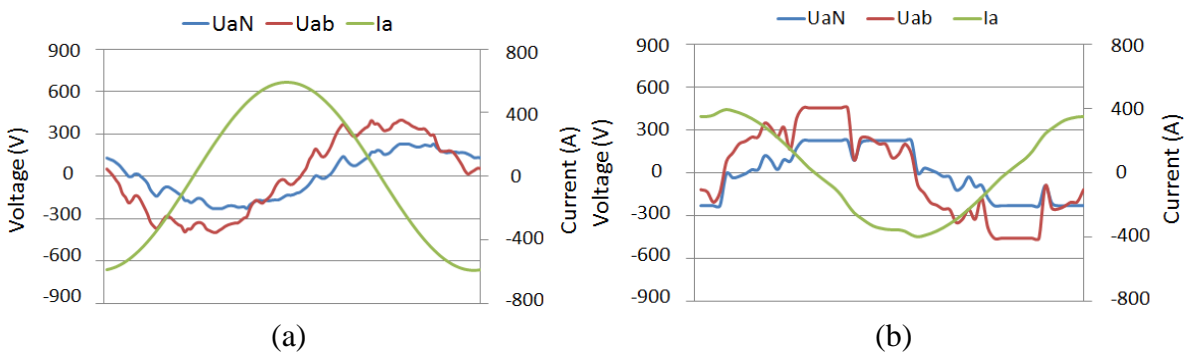

Figure 7-2: Voltage and current waveforms at 3 krpm rotor speed. (a) Distributed winding. (b) Concenrated winding.

76

(a)   (b)
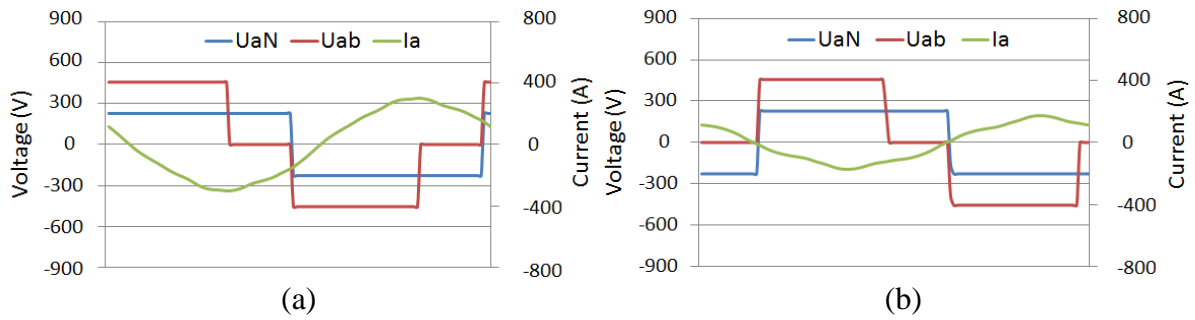
Figure 7-3: Voltage and current waveforms at 15 krotor speed. (a) Distributed winding. (b) Concenrated winding.
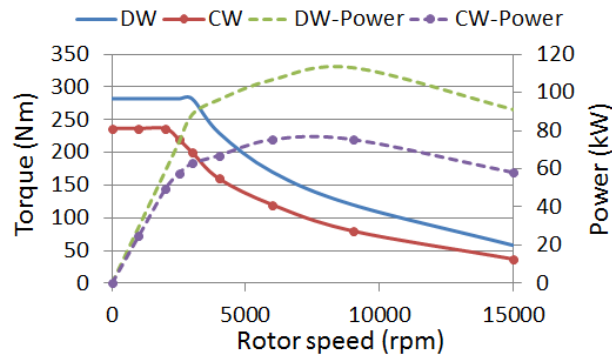
Figure 7-4: Torque vs. speed for distributed against concentrated winding.

(a)   (b)
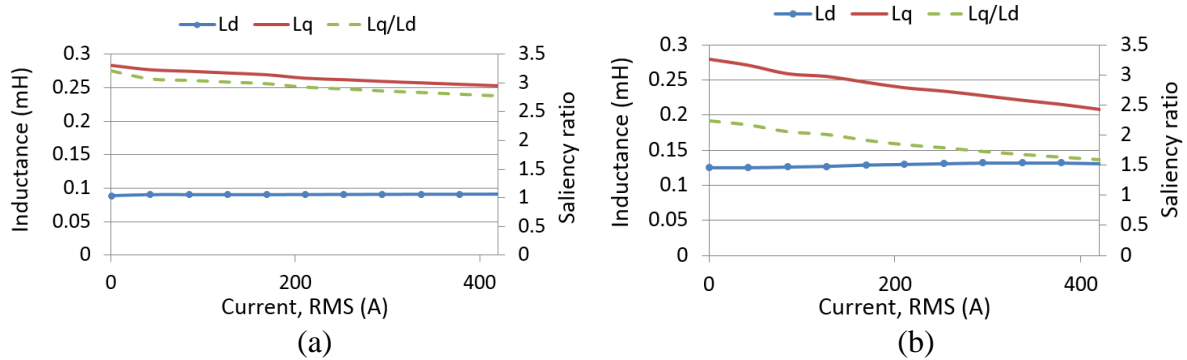
Figure 7-5: D and Q-inductance and saliency ratio vs. current. (a) Distributed winding. (b) Concenrated winding.

7.3 Winding Losses

The winding losses, in a traction motor, form the majority of the total losses during the high torque low speed region, while they still may be comparable or larger than the iron losses during the low torque high speed region due to the losses associated with the field weakening current. Due to the high power density and large CPSR requirement of the traction motors, these motors are usually designed with a high top speed rating, such as the HSFM in this report, as a result of which, care must be taken to avoid excessive AC losses in the windings.

By increasing the slot fill factor, defined as the conductor area to the total slot area, the DC

winding losses can be reduced proportionally. On this basis, the concentrated winding with a modular stator is, usually, regarded as a higher efficiency option, due to the higher achievable fill factor compared to the distributed winding design. However, through the studies of the AC losses by the authors, it has been realized that if the additional fill factor results in a random lay out of the parallel wires, the AC losses might be pronounced to such an extent that lower fill factor options with an organized wire layout might be preferred. To demonstrate this effect in the current chapter, the concentrated winding design in Chapter 7.2 is fitted with 16 turns and 6 wires in parallel per turn for a low fill factor option with an organized wire layout, Figure 7-6(a), and with one additional wire per turn for a high fill factor option, where due to the additional wire, the disposition of the wires in the preferred layout becomes more complex to achieve, thereby a random layout has to be assumed, Figures 7-6(b) and (c). It should be noted that by the organized layout, it is meant to maintain all or maximum number of the parallel wires within one turn in the same radial location; this is to minimize the dominant part of the proximity effects due to the dominant variation of the slot leakage flux in the radial direction compared to the circumferential direction. With regards to the random layout, two scenarios were assumed where the wires were disposed once in the optimistic configuration, Figure 7-6(b), i.e. most of the wires were accommodated in the same radial location to experience the least proximity effects, and once in the pessimistic configuration, Figure 7-6(c), where most of the wires were disposed in different radial locations, to experience the largest proximity effects.

The external circuit driving the 3-phase coils and a mesh view have been illustrated in Figures 7-6(d) and (e). With regards to the circuit, it should be noted that all the 16 turns follow the configuration of the 3 turns demonstrated in the Figure. Furthermore, since the overall ampere-turn is unaffected by the AC effects, and to reduce the simulation bulk, only the parallel strands in one of the phases have been modelled. With regards to the mesh quality, the elements size has been defined to be 5 times smaller than the minimum skin depth in the copper windings, calculated for the 12th harmonic component at 1.25 kHz fundamental frequency, Figure 7-6 (e).
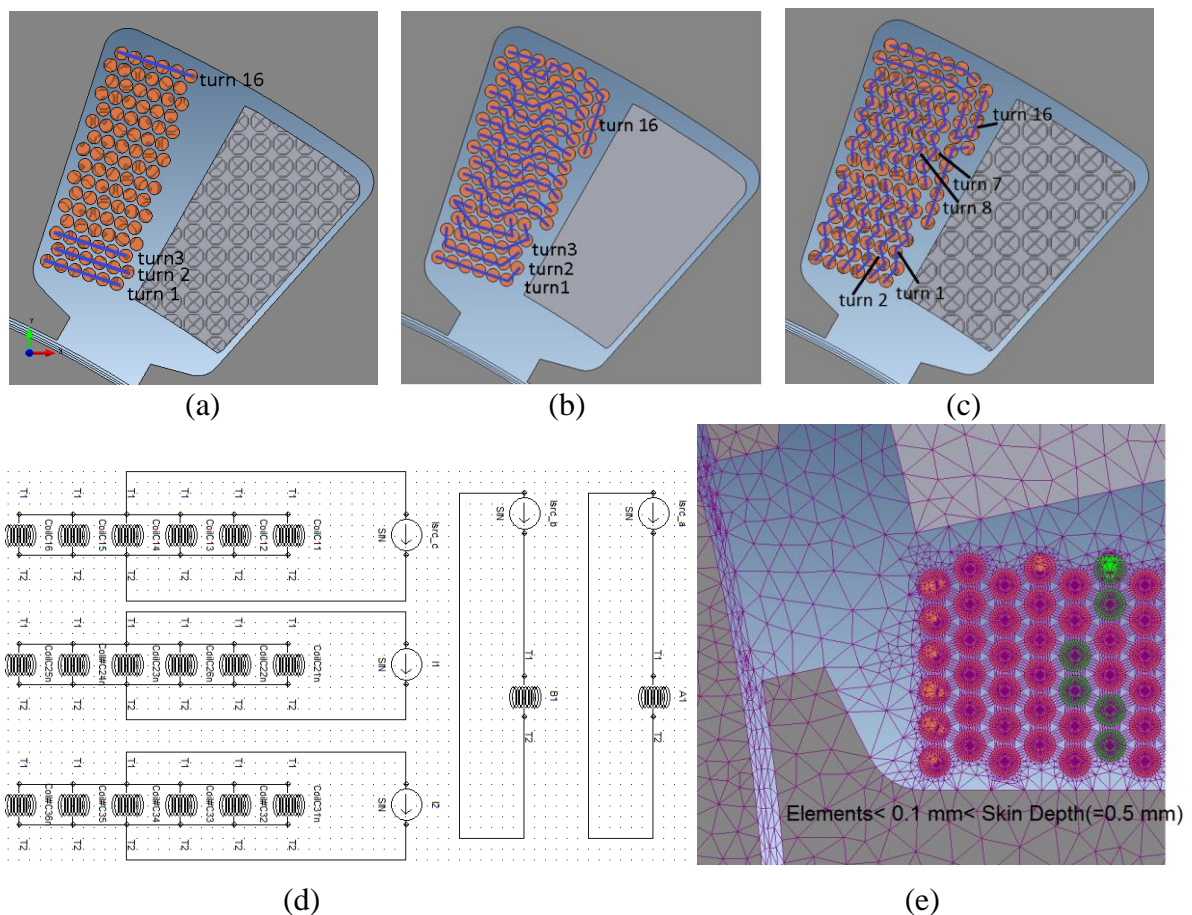
Figure 7-6: The layout of turns and parallel wires in the concentrated winding design, circuit and mesh view. (a) Organized layout with low fill factor. (b) Random layout with high fill factor, optimistic. (c) Random layout with high fill factor, pessmistic.(d) External circuit driving the 3-phase coils, and parallel strands.(e) Mesh view.

The time average winding loss distribution in the wires from the AC loss analysis in 2D FE (a transient motion analysis with the effects of the magnets included) have been shown in Figure 7-7, and the total loss over DC loss factor in average and for the conductor with the largest losses have been summarized in Table 7-1. With regards to these losses and as explained in Figure 7-6, it should be noted that only the skin and proximity losses due to the slot leakage have been accounted for, i.e. the global circulating currents due to the asymmetry between the coils have been neglected assuming a perfectly symmetrical model. Based on Figure 7-7 and Table 7-1 the following comments can be made: a) when the parallel wires belonging to each turn are organized circumferentially, the losses are more uniformly distributed, thereby the AC loss factor is minimum, b) however, when the parallel wires are randomly distributed, the current density and losses tend to concentrate in the conductors which are located in the more inward radial locations, i.e. the locations with higher slot leakage ratio and, relatively, closer to the field variation from the magnets; this

can be better visible from the loss waveforms for each individual strand that are plotted in Figures 7-7 (e) and (f); c) as a result, and as indicated in Table 7-1, not only may the quality of the wires disposition influence the average total winding losses (influencing the efficiency of the motor), but also it may result in severe formation of local hot spots in the winding. On this basis, in a pessimistic scenario the hot spot conductor may experience up to 64.2 times the average per wire DC loss.

(a)

(b)

(c)

(d)

(e)

(f)
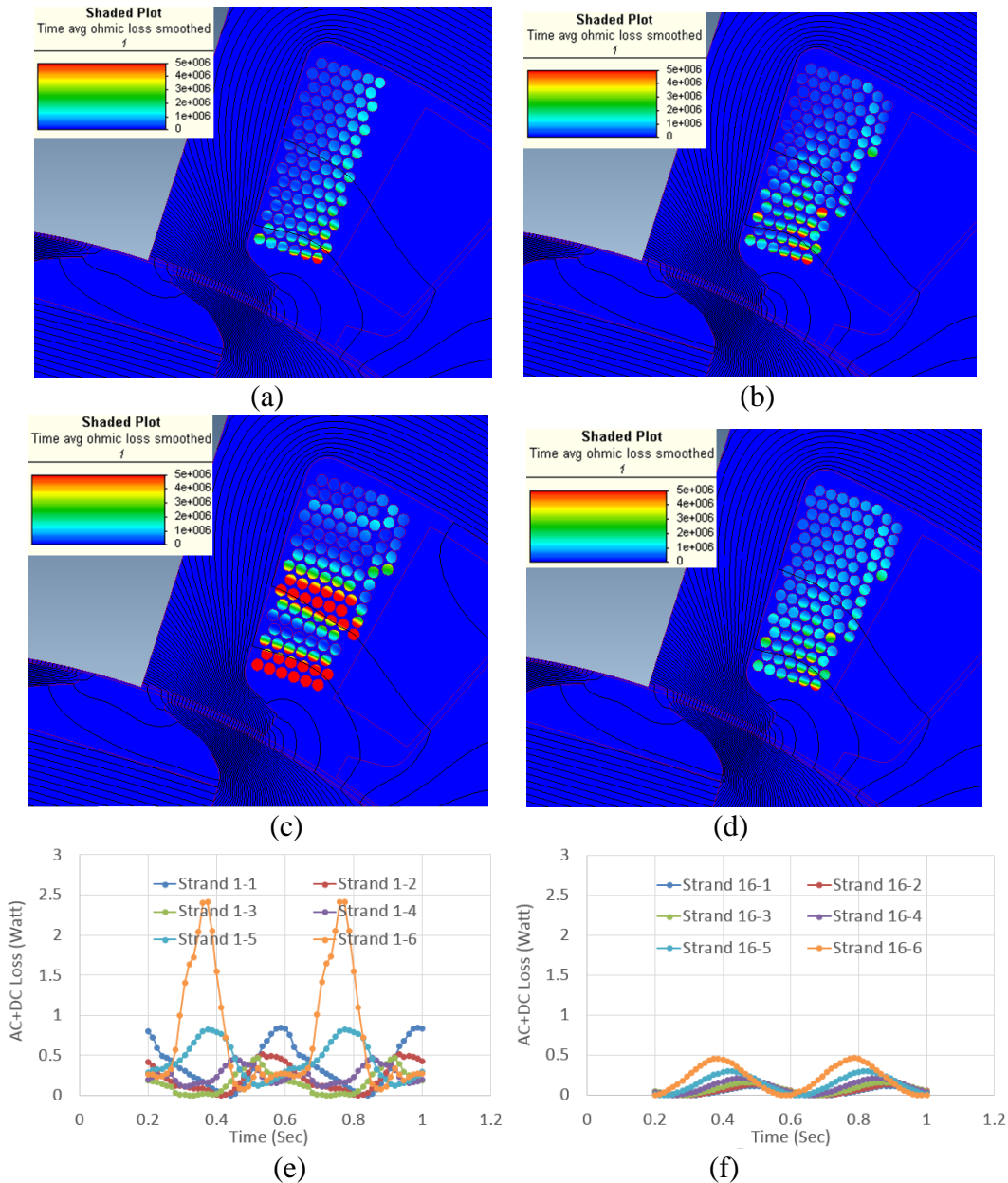
Figure 7-7 Winding AC + DC loss distribution, 2D FE. (a) Organized layout. (b) Random layout, optimistic. (d) Random layout, Pessimistic. (d) Random layout, optimistic, Aluminium wires.(e) Loss per strand in turn 1, organized lay-out, Copper. (f) Loss per strand in turn 16, organized lay-out, Copper.

With regards to the aluminium wires, from Figure 7-7 (d) and Table 7-1, it can be realized

that even though using aluminium instead of copper wires will raise the DC losses, it may, significantly, mitigate the AC loss effects. To explain the impact further, a summary of the DC and total loss values at base and top speed peak power operating points have been reported in Table 7-2, where cells indicating the maximum losses have been highlighted. From Table 7-2 it is realized that, with regards to the maximum total loss, the copper winding results in 30% lower combined DC and AC losses compared to aluminium, which is less significant than 75% ratio when only DC losses are compared (due to 75% lower resistivity of copper). However, the main advantage of using aluminium is revealed when the local effects, i.e. the losses in the individual conductors are comparted. In this respect, the maximum loss per aluminium conductor (indicated as worst conductor), is about, only, 68% of the design with copper windings. Accounting for the non-ideal transfer heat coefficient between the wires (due to the insulations and air voids between the wires), the lower power losses in the individual conductors may result in lower risk of local hot spot formations, which may ultimately result in higher power capability and reliability of the designs based on the aluminium windings.

TABLE 7-1

Average and worst conductor AC Loss factor for CW and DW designs with different wire layouts and materials.

	AC+DC/DC, total	AC+DC/DC, worst conductor
CW, Copper, Random-Pessimistic lay-out	7.9	64.2
CW, Copper, Random-Optimistic lay-out	2.3	11.7
CW, Aluminium, Random-Optimistic lay-out	1.5	4.6
CW, Copper, Organized lay-out	1.6	8.1
DW, Copper, Organized lay-out	1.4	5.8
DW, Aluminium, Organized lay-out	1.1	3.0
DW, Aluminium, Organized lay-out, DELTA	1.02	1.3

TABLE 7-2

Comparison of aluminium and copper winding loss, CW random-optimistic lay-out, at 2 krpm and 15 krpm.

	Copper, total (W)	Aluminium, total (W)	Copper, worst conductor (W)	Aluminium, worst conductor (W)
2 krpm, DC loss	3800	6500	33.9	58
2 krpm, AC+DC loss	4500	6900	82.3	85.8
15 krpm, DC loss	2060	3600	18.4	32.1
15 krpm, AC+DC loss	4800	5300	215.3	146.7

To assess the AC loss effect in a distributed winding design, the stator in Figure 7-1(a) has been fitted with a 16 turn winding, with each turn composed of 3 parallel wires, Figure 7-8(a). Providing a suitable fit of the slot aspect ratio to the specified number of turns and wires, it was intended, and later confirmed by the manufacturers, that a wire layout close to an ideal pattern was, mostly, achieved, Figure 7-8(b). From Table 7-1, it can be realized that the proposed organized layout has resulted in a very low AC loss factor, which has been, further, enhanced by changing the wires from copper to aluminium. Furthermore, a comparison of the distributed against concentrated winding option reveals that the distributed design may result in lower AC loss effects, which can be attributed to the lower per unit slot leakage flux in the case of distributed winding design. Finally, a comparison of the Star and Delta connection has been made, where a delta connected 28 turn distributed winding with 6 parallel wires per turn organized in a preferred layout has been analysed, Figure 7-8(c) and Table 7-1. The voltage and current drive of the Delta connected design has, furthermore, been adjusted so that a similar torque and power performance as that with the Star winding could be achieved. Based on the results in Table 7-1, it was realized that due to the smaller wire size (as a result of the higher number of turns) in a Delta connected design, lower AC losses can be achieved. However, this conclusion is, only, valid, when assuming that the parallel wires can, still, be disposed in a preferred lay-out, since a random lay-out of the wires may negate the effect of the smaller wires and raise the AC losses significantly. Finally, it is worth noting that for a randomly wound motor design, an average value

between the pessimistic and optimistic layout may be considered for general AC loss and efficiency map calculations.
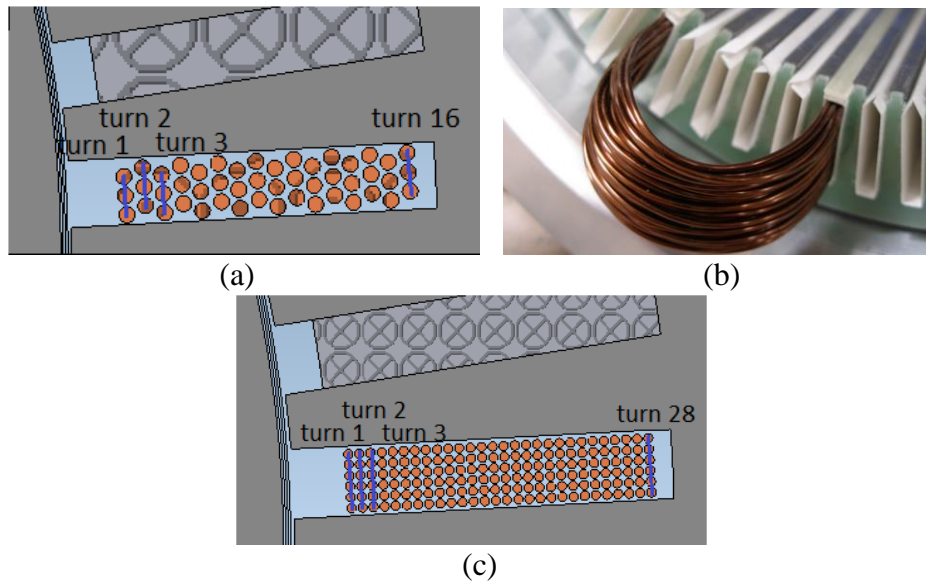

Figure 7-8 The layout of turns and parallel wires in the distributed winding design. (a) Organized layout, STAR. (b) A sample of manufactured coil. (c) Organized layout, DELTA.

7.4 Conclusion

In this chapter, the superiority of a distributed wound stator to a concentrated alternative in terms of a higher torque and power density performance, and based on theoretical analyses, was demonstrated. It was shown that a distributed winding may benefit from a higher achievable current per unit DC link available voltage compared to a concentrated winding, due to the lower per unit inductance, while higher winding factor and saliency ratio in the former may result in a larger torque and power density of the motor. With regards to the AC loss effects, it was shown that the layout of the parallel wires within a turn can have a significant influence on the proximity losses. Furthermore, it was proposed and demonstrated that a suitable choice of the winding turns and parallel wires per turn may enable the designers to mitigate the AC losses via an organized disposition of the parallel wires in an ideal circumferential arrangement. Based on a comparison of aluminium against copper windings, the important benefit of using aluminium wires in mitigating the total losses in the individual conductors, thereby, reducing the risk of thermal failure due to the local hot spot formation was, for the first time, reported.

In this chapter, the theoretical findings in the previous chapters are compared and validated against a series of electromagnetic, structural and thermal testing. To address the objective of each individual study and to simplify the manufacturing needs, a range of simplified custom built prototypes as well as full scale prototype designs have been manufactured and tested.

8.1 Custom built scaled prototype and test set-up

The testing described in this section is intended to assess the electromagnetic torque and demagnetization withstand capability of the proposed ferrite magnet motor design in Chapter 3. On this basis, the prototype machine is simplified in several areas: a) The stack length is reduced to one fifth, to include only one of the five rotor sections as shown in Figure 8-1(a), i.e. skewing is neglected, b) To measure the static torque only two coils of a single phase have been wound in the stator, as shown in Figure 8-1(b), c) Due to the procurement challenges at the time, FB9B magnets were replaced by weaker but more readily available grade of ferrites, i.e. Ceramic 8, with B_r equal to 0.37 T and H_{cj} equal to 260 kA/m both at 20˚C, d) No cooling arrangements have been made for this prototype; thus to avoid temperature rise and/or overheating, each current injection was limited in duration to last no more than 2 seconds. Time taken to adjust and fix the rotor position between each injection meant that all results correspond to a winding temperature of ~20˚C. The test bed is shown in Figure 8-2.

(a)   (b)
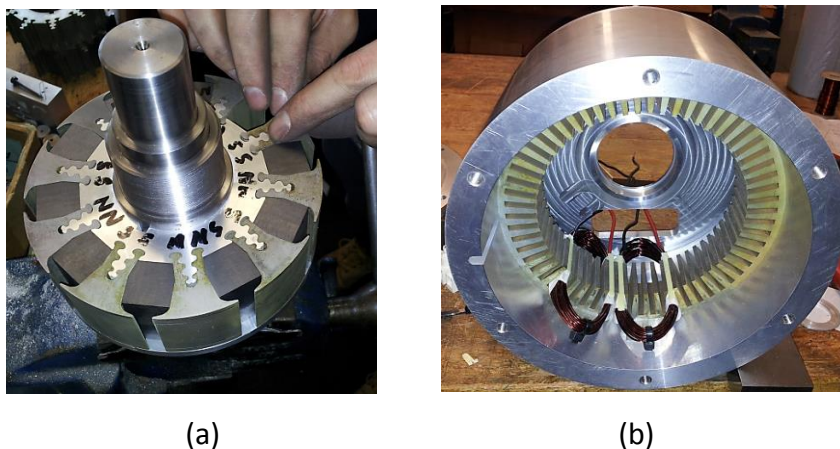
Figure 8-1: Simplified prototype motor. (a) Rotor and magnets, (b) Stator, coils and custom built housing without cooling.
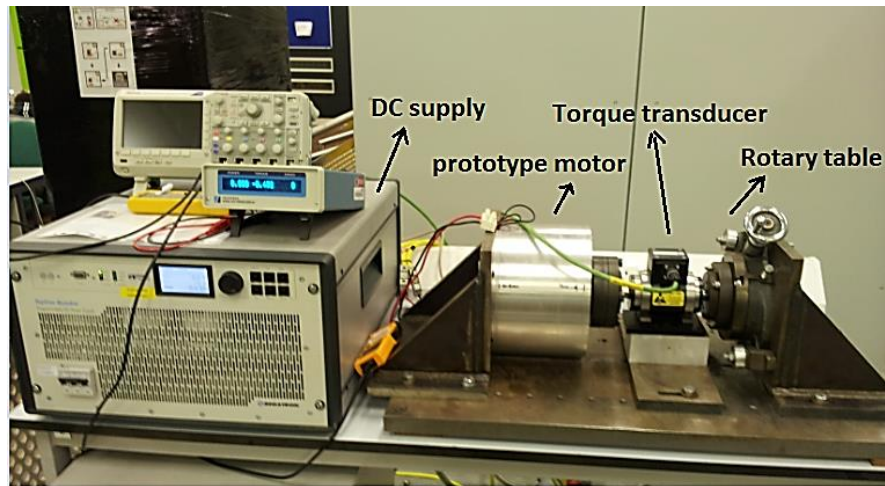
Figure 8-2: Prototype test set-up.

8.1.1 Back-EMF (BEMF) and Static Torque Tests

The BEMF induced in one of the two coils of the prototype motor is measured at a fixed speed and compared to the 2D FE model which was set-up for the same conditions and the magnet grade explained in Chapter 3. To simplify the comparisons, the peak value of the FE predicted BEMF in Figure 8-3(a) is defined as 1 per unit throughout this chapter. As shown in Figure 8-3(a), the measured BEMF is about 7% lower (fundamental component calculated from FFT) compared to the 2D FE prediction, which may be largely attributed to the leakage of magnet flux in the end regions. However, it should be noted that since the stack and magnets axial length in the actual design are 5 times longer than the test prototype, the end leakage ratio in the full size machine will be lower.

The static torque for different magnet / armature alignments is measured with a torque transducer, with rotor angle fixed through the use of a rotary table, Figure 8-2. An identical model was set-up and simulated in 2D FE, and the results of the simulation and measurement are compared in Figure 8-3(b). The two curves show very close agreement in terms of torque variation against the rotor position which can be looked upon as the advance angle. However, the peak torque from the prototype is about 9% smaller than the 2D FE prediction, which is due to the end leakage from the magnets and the armature windings, as well as the discrepancies between the actual material characteristics, such as the laminations BH curve, and the simulation data. Similar to the comments on the BEMF, the relative loss of torque is expected to be lower for a full size machine.

By scaling the results in Figure 8-3(b) to the full motor size and assuming the actual grade of magnet (a total scaling factor of 29 may be used), it can be concluded that the proposed

design can deliver a peak torque and power density of up to 19 Nm/liter and 6 kW/ liter (based on a 14 liter gross volume including the cooling housing and end windings, and a base speed assumption of 3000 rpm) which fulfil the requirements in Table 3-1.


(a) (b)
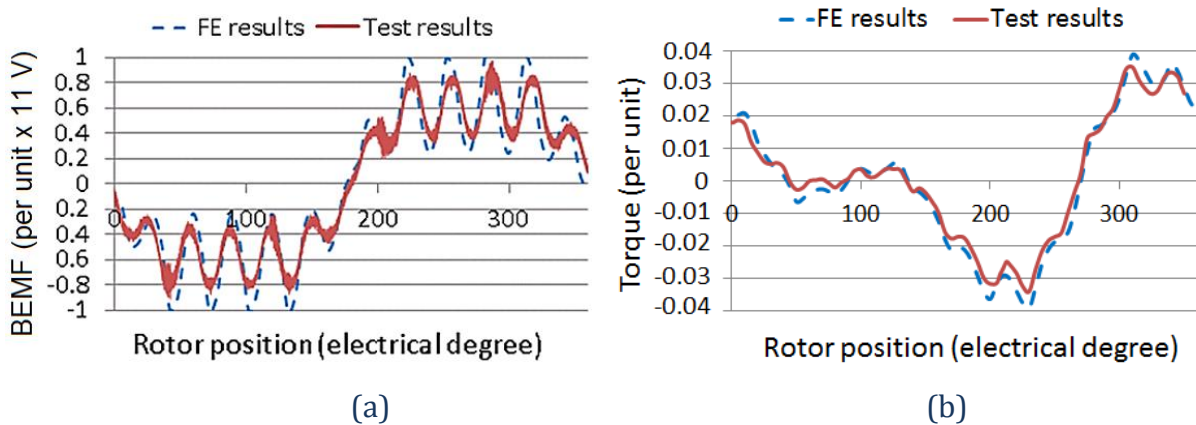
Figure 8-3: Motorette performance, comparison between measured and FE calculations. (a) BEMF at 33 Hz electrical frequency. (b) Static torque vs. different rotor angles.

8.1.2 Demagnetization Test

To assess the demagnetization withstand capability of the design, currents with 160%, 200% and 240% of the peak current amplitude, i.e. 1 per unit x 425 A, rms, are injected in the negative d-axis. To accommodate all three current injections in a single test and provide a clear comparison, three magnets were subjected to different demagnetization fields, as shown in Figure 8-4. Once the demagnetization fields have been applied, the BEMF for one mechanical revolution of the rotor is then measured at the same speed as for the previous BEMF tests. The result is shown and compared against the BEMF prior to demagnetization test, Figure 8-5. As shown, neither the magnet experiencing 160% of the peak current (resembling the peak short circuit current), nor the one exposed to 200% of the peak current is demagnetized, and the associated BEMF waveforms, therefore, are unchanged. On the other hand, the magnet associated with 240% of the peak current is partially demagnetized and the relevant BEMF is reduced by 12%, Figure 8-7.

To better understand the results, a similar demagnetization scenario was modelled in 2D FE. The predicted demagnetization is illustrated in Figure 8-6, the red areas indicating the field strength greater than or equal to 260 kA/m and the magnet regions that will be demagnetized. In a further assessment, the demagnetized areas were replaced by air and the modified FE models were run at the same RPM as that of the measurement. The simulated BEMF values (fundamental components) are compared against those from

86

measurement in Figure 8-7. It is interesting to note that the 2D FE model prediction is significantly more pessimistic than the measurement. This can mostly be attributed to the relatively short length of the prototype which allows for higher end leakage from the coils as well as the magnets. This phenomenon is expected to lower the magnetic coupling between the armature and the magnets, leading to a better demagnetization withstand capability in total. On this basis, it is expected that for the actual model with five times larger stack length the demagnetization behaviour will be worse than the measured values and closer to 2D FE predictions. A detailed 3D FE analysis of this phenomenon has been addressed in Chapter 4.
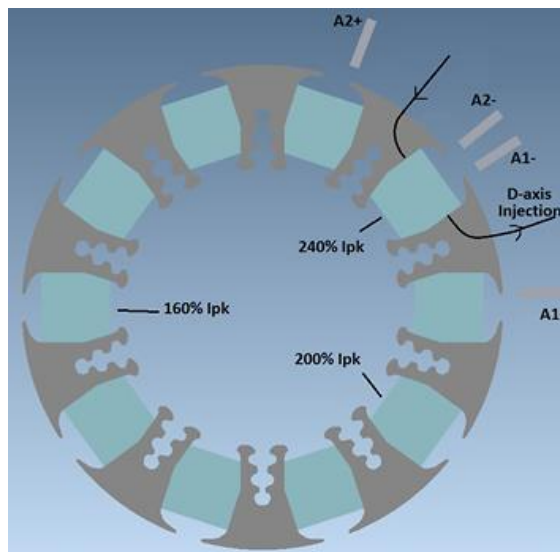

Figure 8-4: Demagnetization test configuration.
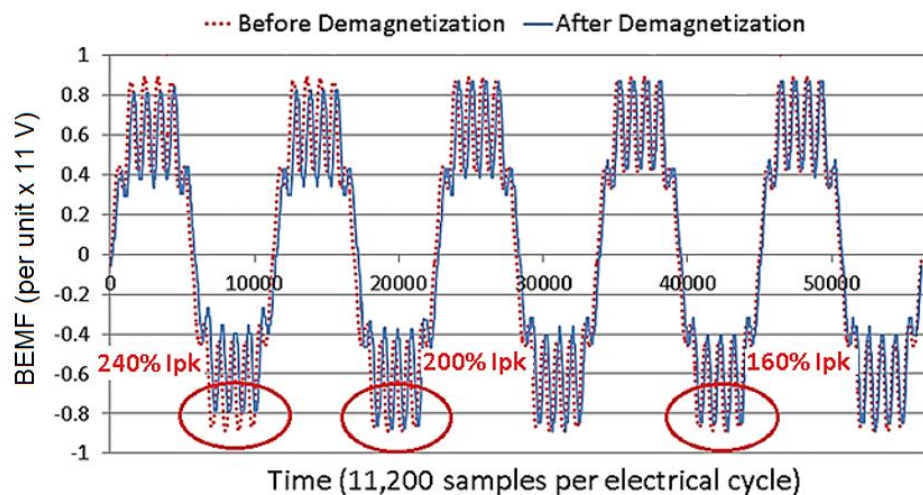
Figure 8-5: BEMF before and after negative d-axis current injections, at 33 Hz electrical frequency.

| (a) | (b) | (c) |
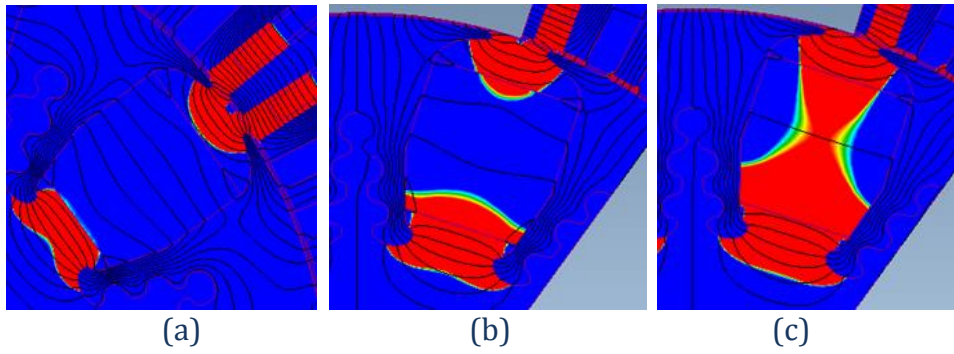
Figure 8-6: 2D FE predicted demagnetization (H) with different current amplitudes applied in negative d-axis. (a) 160% Ipk. (b) 200% Ipk. (c) 240% Ipk.
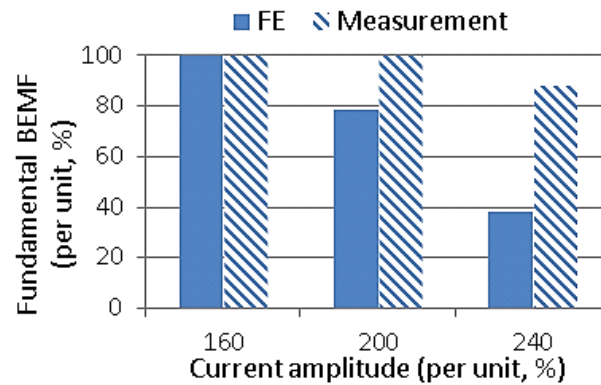

Figure 8-7: Loss of BEMF fundamental component due to demagnetization; prototype measurement compared against 2D FE.

It should be noted that the testing at the lower than room temperatures has not been conducted due to the prototype testing results outperforming those of the FE predictions, according to which the design is robust down to -40 ˚C temperature, Figure 3-10.

8.2 Effect of stack length on demagnetization and evaluation of designs with low grade of ferrite magnets

To support the 3D FE tool and simulations in Chapter 4, a prototype with 39 mm stack length corresponding to Figure 8-1 and using both Ceramic 8 and FB9B Ferrite grades has been built and tested, Figure 8-2. The rotor is once supplied by FB9B grade and once by Ceramic 8 grade magnets, and all tests are assured to be at the room temperature of 20 ˚C, which is identical to the assumed conditions in Chapter 4. To simplify the manufacturing, only two coils belonging to one of the phases have been wound, while the single phase current was adjusted to correspond to the 3-phase system, see Appendix V.

8.2.1 Demagnetization

To assess the demagnetization performance of the designs, currents with amplitudes of 160%, 240%, and 400% of the I_{pk} are injected in the negative d-axis position relative to the magnets. To achieve a better resolution, each of the three current injections was targeted at only one magnet pole out of the ten, while it was assured that the three affected poles are distant from one another by, at least, one unaffected pole in between, Figure 8-4.

After the current injections, the BEMF of the prototype has been measured for one full mechanical revolution, as shown in Figure 8-8. In Figure 8-8, only the distorted waveforms and the associated current levels are highlighted (160% I_{pk} for both magnet grades, and 240% I_{pk} in case of FB9B grade have not affected the BEMF waveforms).

To compare the results against the 3D FE findings in Chapter 4, the demagnetized regions in the FE models were replaced by air, and the BEMF of the modified models were re-calculated; the fundamental BEMF components from FE modelling and the prototype testing are compared in Figures 8-9(a) and (b). From Figures 8-9 (a) and (b) it can be realized that: a) For both FB9B and Ceramic 8 magnets the prototype test results match closely with the 3D FE findings (compare the results for 39 mm stack length), confirming the validity of the FE tool and the modelling applied in Chapter 4; b) The largest variation of demagnetization performance due to change of stack length (indicated as margin of improvement in Figure 8-9) has been obtained for the Ceramic 8 magnets, and for the case with 240% I_{pk} current. In this scenario, the stack length shortening mitigates the risk of demagnetization by 65%, which implies that the rather poor Ceramic 8 magnets may not only withstand the 3-phase short circuit currents (160% I_{pk}) with a good safety margin, but they can, also, retain much of their magnetic properties in case of more severe faults.

(a)   (b)
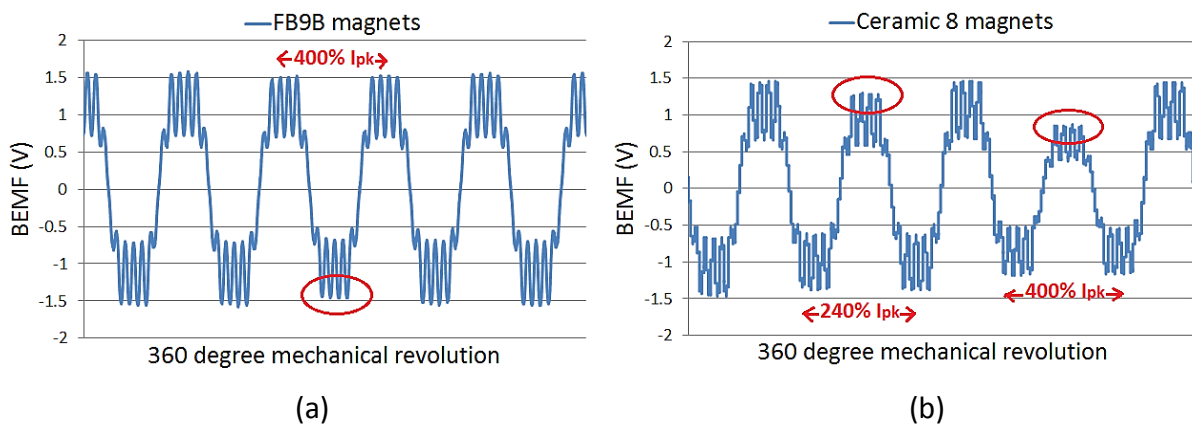
Figure 8-8: BEMF waveforms after the demagnetization test. (a) FB9B. (b) Ceramic 8.
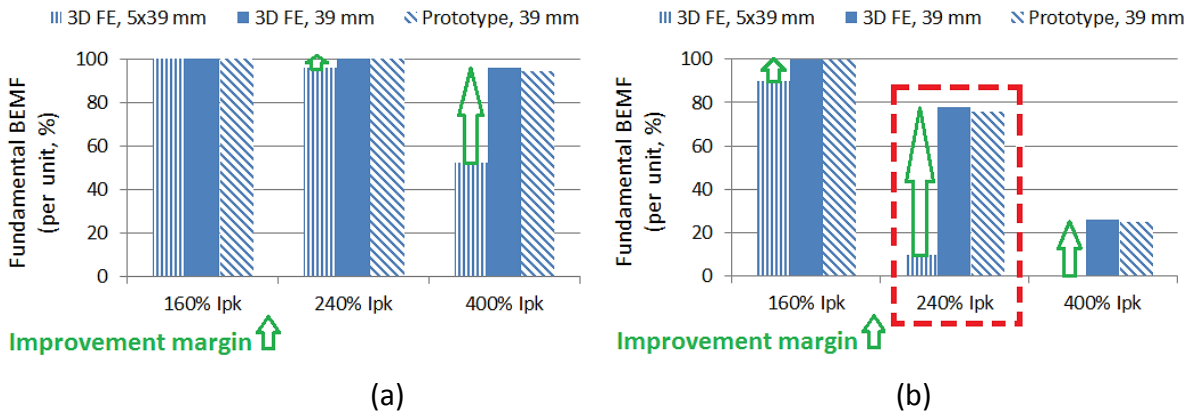
Figure 8-9: Loss of BEMF fundamental component due to demagnetization. (a) FB9B magnets. (b) Ceramic 8 magnets.

8.2.2 Static Torque

The static torque (measured at 100% I_{pk}) of the prototype with FB9B and Ceramic 8 magnets is measured and compared in Figure 8-10 (only two coils out of the ten coils have been excited, Figure 8-1 and Appendix II). Based on Figure 8-10, the difference between the two magnet grades is about only 3% in peak torque, which matches well with the findings and explanation in Chapter 4.4.2. The ~9% deviation between the simulation and the test results (Figure 4-10 and Figure 8-10) is partially due to the end leakage effects, and partially due to the deviation of the actual materials characteristics, such as the laminations B-H data, from the data assumed in the simulations.
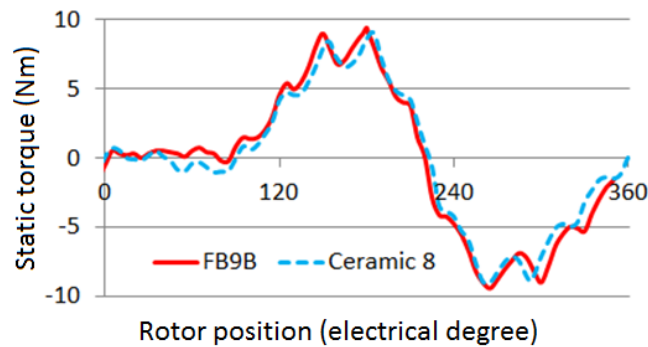
Figure 8-10: Comparison of static torque test results for 39 mm stack length design using Ceramic 8 and FB9B magnets.

8.3 Full scale prototype BEMF and static testing

Due to the difficulties in procuring low volumes of work hardened stainless steel, the more readily available Nitronic 50 (with similar magnetic and structural properties as 3% work hardened steel) was used in a full scale prototype motor. The full size prototype set is shown

and compared against the Nissan Leaf motor in Figure 8-11. As discussed in Chapter 3, the prototype ferrite motor has a similar envelope as the rare earth magnet design in Leaf, which allows for a better evaluation of the ferrite based design.

The Back-EMF (BEMF) of the prototype motor is measured at the 20 ˚C room temperature and a fixed rotor speed, corresponding to 33 Hz electrical frequency, and shown in Figure 8-12(a). Furthermore, the fundamental component is linearly scaled against the rotor speed and compared against the FE 3D simulations, Figure 8-12(b). From Figures 8-12(a) and (b), it can be realized that the BEMF is close to sinusoidal, due to the rotor skew, while there is a 4% difference between the measurement and the 3D FE predictions, which can be mainly attributed to the manufacturing tolerances such as the small and random gaps between the magnets and the rotor pole, which were neglected in the FE modelling, Figure 8-12(c). It should be noted that the aforementioned gaps can be treated either directly in a FE simulation, or alternatively modelled as an adjustment factor raising the effective airgap length.

The static torque of the prototype motor has been measured using a test set up shown in Figure 8-13 and the peak values are shown against the stator current in Figure 8-14. It should be noted that a water cooling system was applied to maintain a constant rotor temperature of ~65 ˚C throughout the test. Based on Figure 8-14, the torque follows a quasi-square function at lower current levels (due to the high reluctance torque contribution) while at larger currents the rate of increase is diminished due to the magnetic saturation. Furthermore, there is a 4-6% difference between the measurement and the FE 3D results, which can be attributed to the magnet-rotor pole gaps, Figure 8-12(c), as well as heavier saturation effects in the prototype compared to the simulation assumption.

Based on the results obtained from the BEMF and static torque testing, and considering a 9.5 liter volume for the ferrite design vs. 8.5 liter of the Leaf design (including the end winding, but excluding the housing), the prototype in Figure 8-11 may deliver a peak torque and power density of up to 27 Nm/ liter (about 82% of the Leaf motor rating) and estimated 11.7 kW/ liter at 3000 rpm base speed (about 125% of the Leaf motor rating).

Finally, it should be noted that to demonstrate the non-magnetic properties of the austenitic steel applied in the prototype motor, the scaled motorette in Figure 8-1, has been fitted with aluminium rotor support, for which the BEMF and torque measurements were found to be identical to the ones fitted with the austenitic steel rotor support.
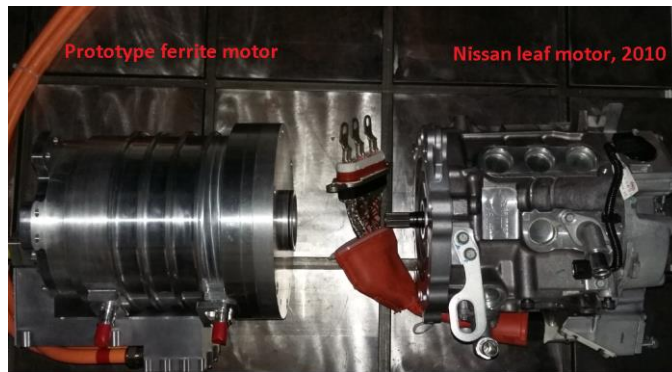
Figure 8-11: Comparison of the full size prototype ferrite motor with Nissan leaf motor.


(a)

(b)
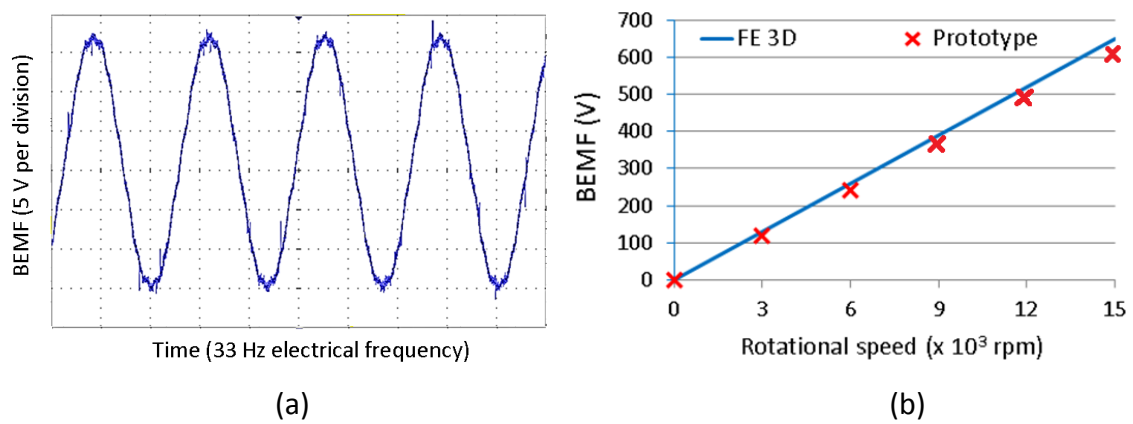
Figure 8-12: BEMF testing. (a) Prototype BEMF measurement at 33 Hz electrical frequency.

(b) BEMF vs. rotor speed. (c) Random gaps between magnets and rotor pole.
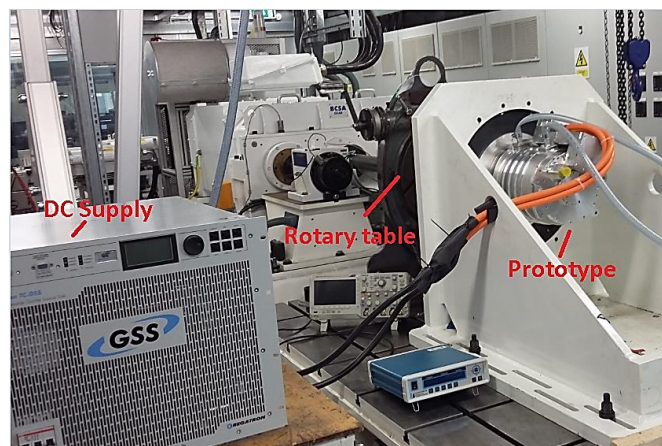
Figure 8-13: Static torque testing set up for the ferrite prototype motor.
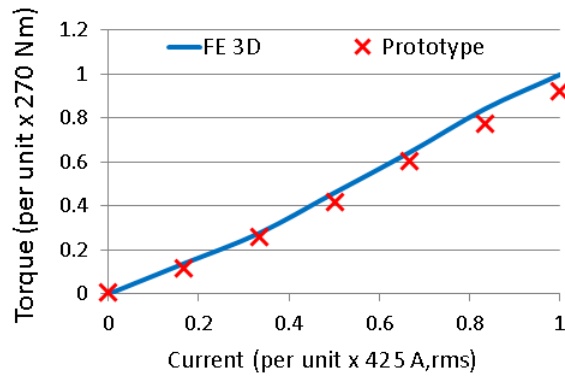
Figure 8-14: Static peak torque against current; prototype testing vs. 3D FE simulation.

8.4 Rotor over speed and fatigue testing

To validate the structural integrity of the rotor and safety of the operation at high speeds, another customized prototype has been built, Figure 8-15(a). As shown in Figure 8-15(a), this prototype comprises of two out of the five rotor axial segments (each of which has one fifth of the reference design stack length), which are skewed according to $\alpha/(m-1)$, α being the total angle of skew equal to 4.8 degree, and m equal to total number of rotor axial segments, i.e. 5. The rotor is further completed with the high speed bearing, and embedded within two sets of protective housing which were securely bolted to the test bed plate and into the concrete ground, Figure 8-15(b). Based on the results from the high speed testing, the prototype rotor proved to be capable of safely operating at 120% of the top speed, with no sign of plastic deformation (based on an accurate measurement and comparison of the rotor diameter before and after the test) or loosening in the fasteners being recorded.

To validate the rotor durability against the risk of premature fatigue failure, a separate test facility was set up, Figure 8-16. The cyclic rotor centrifugal loading during the life time of the motor were simulated by applying equivalent cyclic forces in the rotor radial direction. Each load cycle is representative of the rotor load variation as the rotor is accelerated from a low/idle speed to its rated maximum working speed, i.e. 15 krpm, and decelerated back to the low/idle speed. The aim of the test was to verify the rotor fatigue life, particularly that of the fir-tree-root connection between the electrical-steel pole segments and the stainless-steel support hub.

The fatigue test results suggest that the rotor pole segments and the support hub will survive more than 8 times the rotor fatigue life design target. Such a rotor durability target was selected and agreed with the vehicle manufacturer, and is a conservative estimation of

the rotor "low/idle to maximum working speed" excursions likely to be experienced by the rotor during the life time of the vehicle.
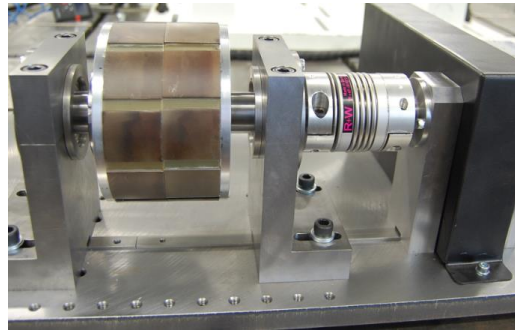
(a)
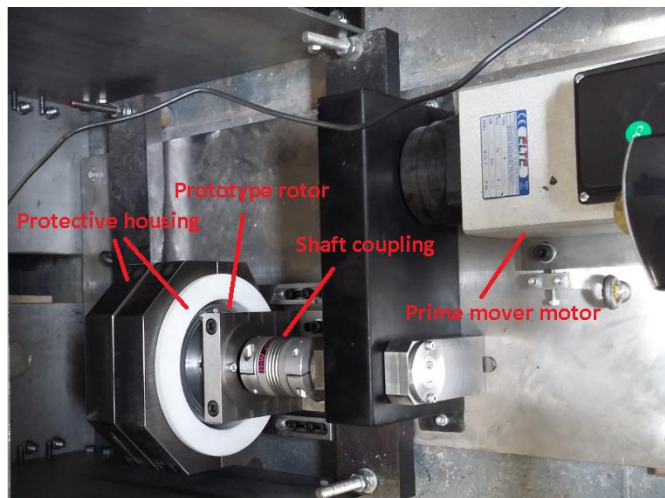
(b)

Figure 8-15: Test set up for the rotor over speed evaluation. (a) Rotor comprised of 2 axial sections, and shaft coupling. (b) Complete set up, including the prime mover and protective housing.
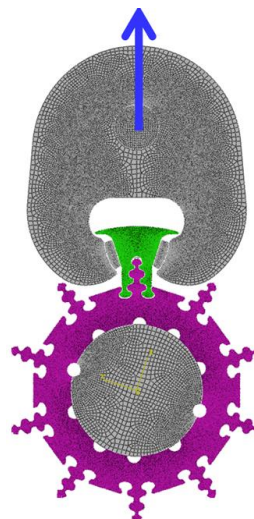
Figure 8-16: Rotor fatigue testing under cyclic loading.

8.5 Single piece spoke type rotor

To validate the theoretical findings in Chapter 6, a scaled prototype of the disclosed single piece rotor topology has been manufactured, Figure 8-17. To allow for a one to one comparison to the fir tree design in Figure 8-1(a), a similar lamination material, as well as stator and winding lay-out has been used. With regards to the magnet, the Ceramic 8 type in Chapter 8.1 was replaced by stronger FB9B grade, Table 3-1, while the performance of the fir tree design was, also, re-calculated by replacing and employing the FB9B magnet type.

8.5.1 BEMF and static torque

The BEMF test results for the two rotor designs have been compared together and to the FE 2D simulations, Figure 8-18. From Figure 8-18, it is realized that the magnetic loading of the single piece design is lower than that of the fir-tree based design, which confirms the difference between the efficiency maps of the two, based on the required current loading explanation given in Chapter 6.

Figure 8-17 Simplified single piece rotor prototype.
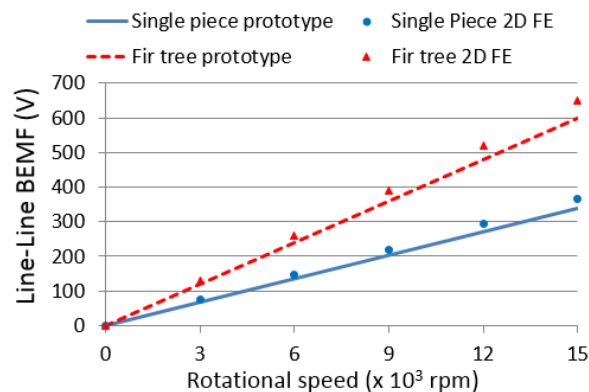
Figure 8-18: BEMF vs. rotor speed; comparison of the single piece and fir-tree based rotor designs.

The static torque of the two designs against zero to maximum current was measured using a rotary table and a torque transducer set up shown in Figure 8-2. Based on the test and FE 2D results in Figure 8-19, it is realized that for both designs the prototype torque is lower than FE 2D predictions. This can be attributed to the 3D effects as well as the deviation of the material data from the modelling assumptions. Furthermore, the test results confirm the FE predicted difference between the two designs in terms of the torque density, indicating a peak torque gap of less than 20%. Comparing the peak torque values of the two rotor designs against the BEMF, and confirming the explanation in Chapter 6, it can, also, be noted that the performance gap between the two designs under the loaded conditions is smaller than that under the no-load, this being due to the higher magnetic saturation under the loaded conditions, resulting in lower magnet leakage and higher actual magnetic loading compared to the no-load conditions. Finally, it should be addressed that due to the additional d-axis leakage inductance in the single piece design compared to the fir tree, the former possesses a lower saliency and reluctance torque contribution; this additional d-axis flux leakage in the single piece design, also, leads to an increased and similar voltage rating as the fir tree design (despite the lower BEMF in the former) which rules out the possibility of a further torque enhancement via a turn increase.
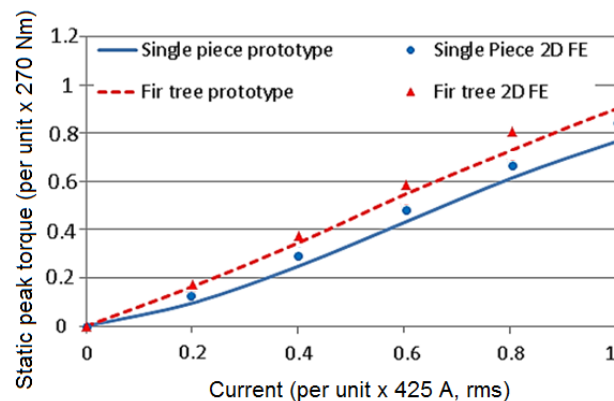
Figure 8-19: Static torque vs. current; comparison of single piece and fir-tree based rotor designs.

8.5.2 Demagnetization

The demagnetization resistance capability of the single piece rotor design has been tested (at 20˚C room temperature) by injecting 160% and 400% of the peak rated current in the negative d-axis position, while the targeted magnets were chosen to be distant by at least one unaffected pole in between, Fig 8-4. The BEMF prior to and after the demagnetization

test has been measured and compared in Figure 8-20, where no sign of demagnetization is observed. For a more detailed evaluation of the demagnetization performance of the single piece and the fir tree based rotor designs, the loss of BEMF (as a result of demagnetization) has been calculated by FE 3D (the demagnetized regions in the magnets were defined as air), and the results are reported together with those from the prototype measurements in Figure 8-21. From Figure 8-21 and confirming the findings in Chapter 4, it is realized that due to the 3D effects (for both rotor designs) the demagnetization performance of the 39 mm stack model is, significantly, superior to that of the nominal design with 195 mm stack length. Furthermore and confirming the predictions in Chapter 6, it can be realized that, except for the local and rather negligible demagnetization risk at light faults, the demagnetization resistance of the single piece design may outperform that of the fir tree design option.
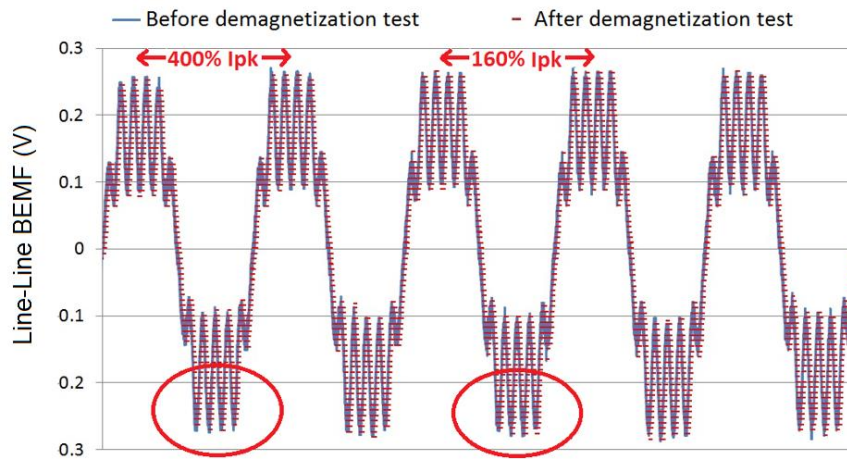
Figure 8-20: BEMF prior and after the demagnetization test, single piece design, at 10 rpm.
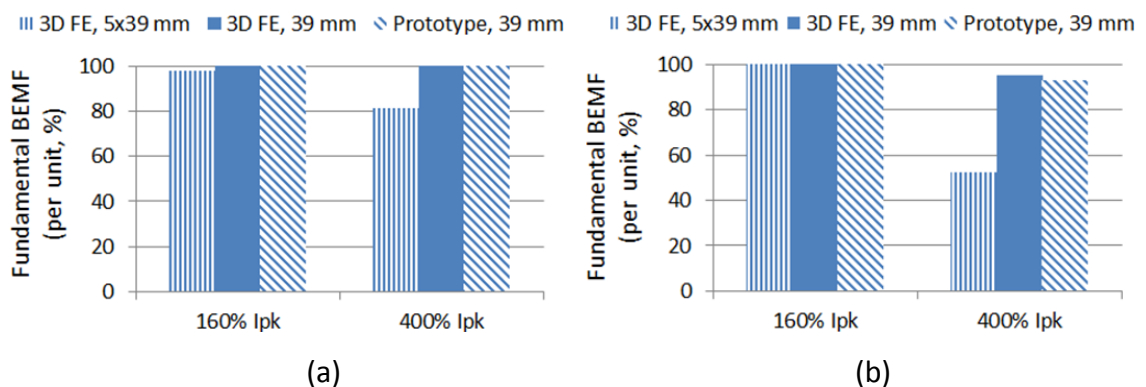
Figure 8-21: Loss of BEMF fundamental component due to demagnetization. (a) Single piece rotor model. (b) Fir tree based rotor model

8.6 Peak thermal loading and windings reliability testing

To assess the thermal performance under the peak torque operation, as well as the reliability of the aluminium to copper terminations, a full size stator including the windings has been prototyped and equipped with thermocouples in three phases and the star point, Figure 8-22. Using a DC current supply, a line current equal to the maximum continuous current and peak transient current has been supplied, and the rise and fall of the temperature has been monitored as shown in Figure 8-23. From Figure 8-23 a maximum temperature rise of ~2 deg per second has been recorded which corresponds to thermal capability of up to 30 seconds operation under peak transient current. It is worth mentioning that the tested prototype is different from the EV product motor in situ, in two ways: a) no water cooling has been fitted onto the tested prototype, b) due to the absence of the rotor and stator housing in the tested prototype, there is a higher level of convection passive cooling, transferring the heat from the windings and the stator into the surrounding air. On this basis, it should be noted that although the temperature rise during the continuous performance is expected to be less severe for the actual prototype (due to the stronger cooling in the latter), the transient performance is expected to be similar; this being due to the short time of the transient operation relative to the thermal time constant.

The stability of the aluminium to copper terminations against the physical expansion-contraction due to the temperature variations has been assessed by supplying a cyclic load creating a 30 ˚C temperature variation between 145 ˚C to 175 ˚C, which was repeated for 200 cycles, Figure 8-24. The choice of the peak to peak temperature variation and the maximum temperature has been based on an assumption of a 15 second transient peak current operation, while the maximum allowable limit of 180 ˚C was lowered by a 5 ˚C safety margin. As a result of the testing, no sign of degradation in the electrical signals or in the windings and terminations have been recorded. The successful testing confirms a mitigated risk of aluminium oxidation, which according to [106, 108], would manifest itself after few initial cycles (the grounds for choosing 200 cycles of testing) of the current and heat exposure.
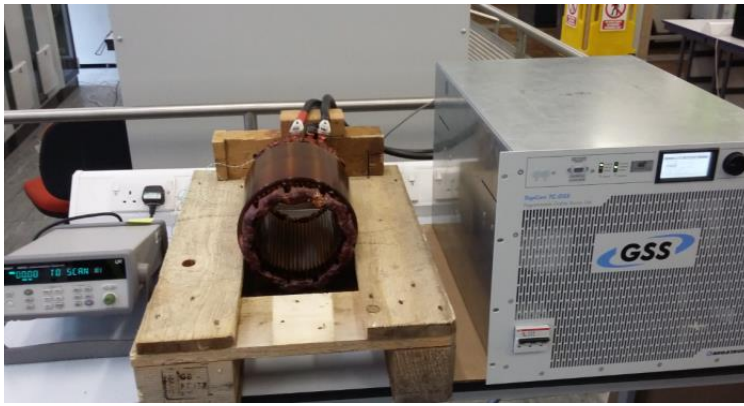
(a)   (b)

Figure 8-22: (a) Thermal test set up for the full size stator with aluminium windings. (b) Close up of the end windings.
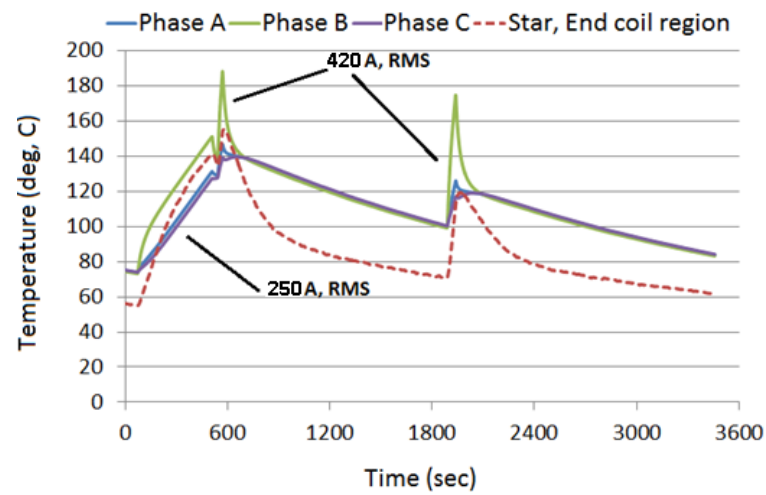

Figure 8-23: Temperature rise vs. continuous and peak current.
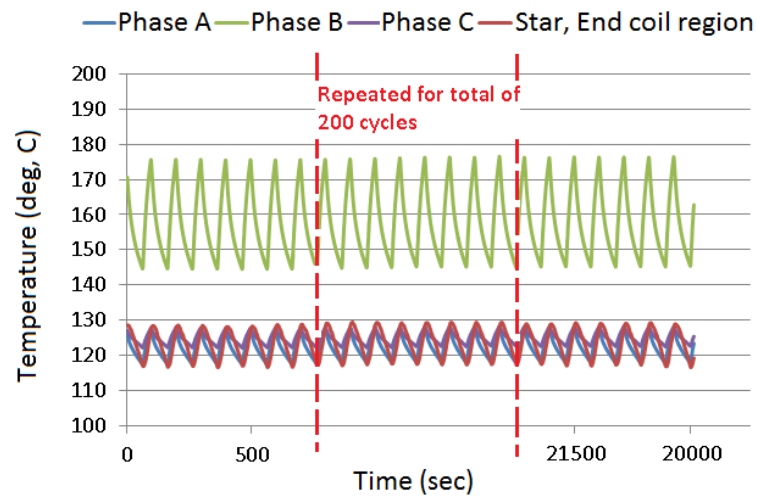
Figure 8-24: Evaluation of thermo-mechanical stability under cyclic loading.

8.7 Continuous and intermittent full scale prototype functional testing

The high speed ferrite motor (HSFM) design with the aluminium distributed winding according to Figures 7-1(a) and 7-8(a) in Chapter 7 (a disposition of the parallel wires close to the ideal pattern in Figure 7-8(a) was achieved during the manufacturing) was manufactured and subjected to a dynamic performance testing, Figure 8-25. The intermittent and continuous performance from an initial rotor temperature of 65 ˚C was measured at different rotor speeds, and under 400 V DC link voltage. The temperature rise as well as current and torque response for the 3 krpm are shown in Figure 8-26(a), and the torque-power performance for the entire speed range and the comparison against the requirements are shown in Figure 8-26(b). The preference of the aluminium wires over the copper for the prototype motor, despite its higher total losses in Table 7-2, is, primarily, to assess the reliability of this rather uncommon concept in a high power density traction application. Furthermore, the choice of aluminium wires resulted in a ~70% winding mass saving (~ 5 kg), as well as a ~90% reduction of the windings cost, both due to the lower mass density, as well as the lower price of the aluminium compared to the copper, [119].

From Figure 8-26(a), it can be realized that the HSFM design with the aluminium windings is capable of providing the maximum torque and power for a duration of about 30 seconds, which exceeds the requirement of 10 seconds and matches well with the initial thermal assessments of the dummy stator set up, Figure 8-23. From Figure 8-26(b), it is realized that even though the HSFM design provides about 9% lower peak torque compared to the requirement, it, notably, achieves a 32% higher peak power at a higher base speed. Furthermore, in terms of the continuous performance, even though the HSFM lags behind the required continuous power at lower speeds (due to the lower than required continuous torque at low speeds), it exceeds the continuous power requirement at the speeds above 6.5 krpm, and provides a maximum continuous power of 60 kW, exceeding the requirement by 28%. Based on the results from the dynamic performance testing, it can be realized that the proposed HSFM design with a distributed aluminium winding (with 9.5 liter volume compared to 8.5 liter volume for the Leaf design), may provide a competitive maximum torque and power density of 25.8 Nm/ liter (about 78% of the Leaf motor rating) and 11.2 kW/ liter (about 120% of the Leaf motor rating), and a maximum continuous power density of 6.3 kW/ liter (about 72% of the Leaf motor actual capability tested in [120]).
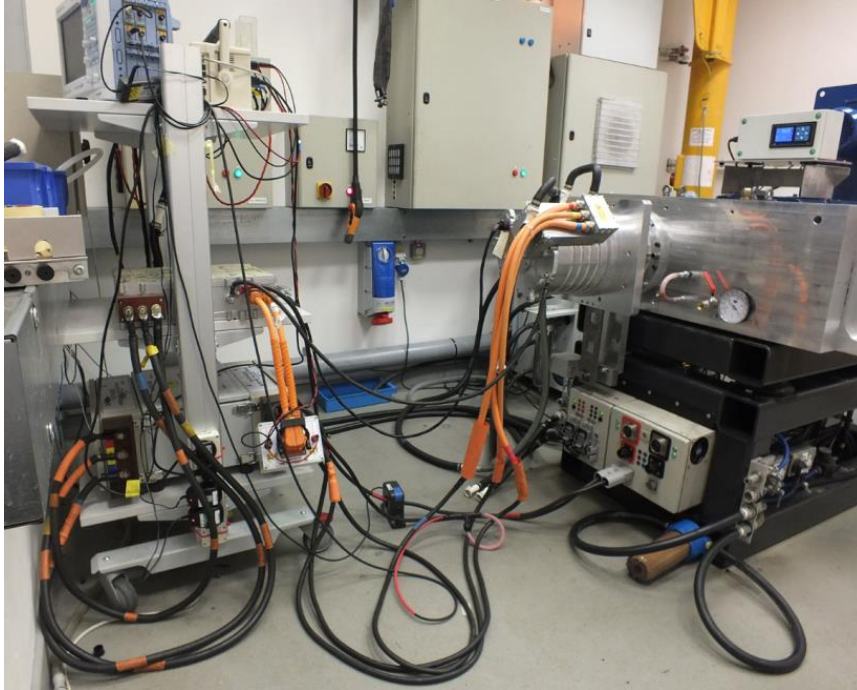
Figure 8-25: Dynamic testing set up of the HSFM prototype.

(a)

(b)
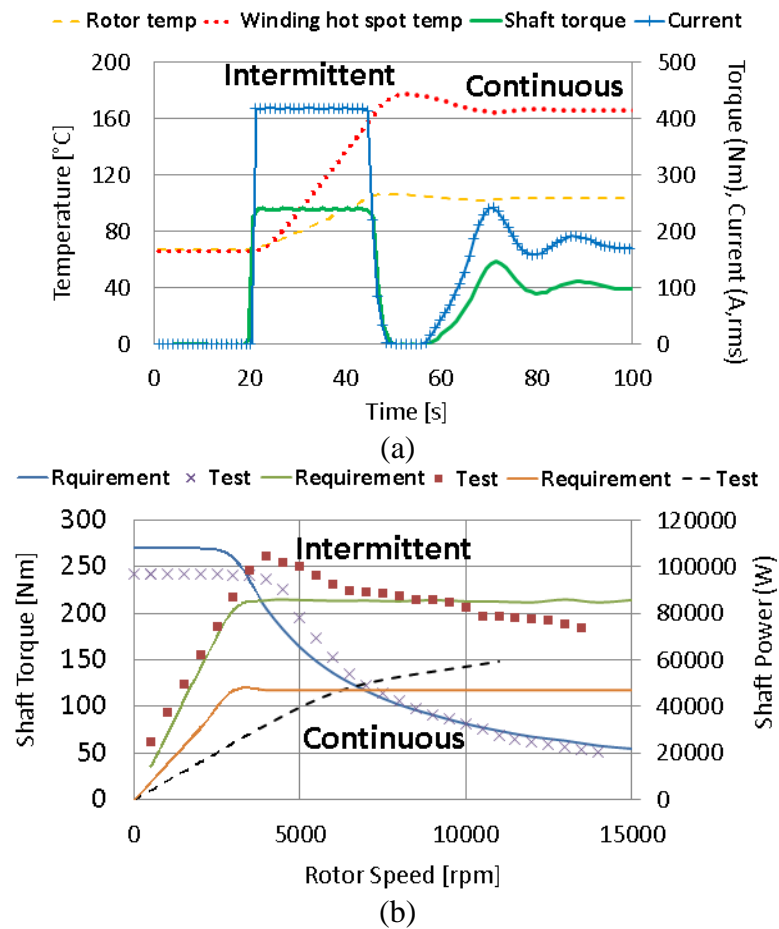
Figure 8-26: Intermittent and continuous performance of the HSFM prototype under 400 V
DC link voltage. (a) At 3000 rpm. (b) Test vs. requirement performance for the entire speed
range.

8.8 Conclusion

Based on the a series of electromagnetic, structural and thermal testing of several custom built and full scale prototypes in this chapter, the theoretical findings in the previous chapters were addressed and validated. It was shown that the proposed fir tree rotor design with the distributed winding may fulfil most of the demanding traction application requirements provided in Chapter 3, including the high power density, demagnetization withstand capability, rotor robustness against fatigue and failure at high speed, and windings reliability during heavy thermal cycles. Despite the excellent achievements in thermal and continuous power performance, a detailed efficiency map validation remains as a future task.

8.9 Acknowledgement

Chapter 9 : CONCLUSIONS AND FUTURE WORK

In this PhD report, the design approach and several critical design details of a low cost high performance traction motor with ferrite magnets and aluminium windings have been reported. Through series of electromagnetic, thermal and structural simulations and prototype testing, the following conclusions can be drawn:

- The spoke type rotor design with a distributed winding is amongst the most suitable candidates to exploit the poor grade magnet materials such as ferrites. This is due to the topological capacity that allows to bypass the armature demagnetization field, while obtaining a combination of flux concentration and reluctance torque in a, relatively, small volume.

- The stack length together with the magnetic saturation level can have a significant influence on the demagnetization. The findings in this thesis, provides further understanding of this effect, which helps to better exploit the magnet materials with low coercivity.

- Two viable configurations of a spoke type rotor, namely the fir tree based and the single piece rotor design have been analysed. Based on the studies, the fir tree option may, better, suit the high speed applications, while special attention must be paid to avoid excessive material and manufacturing costs in the rotor support. Furthermore, the single piece rotor design can be best exploited for a low to medium speed range, since due to the lower centrifugal loading, larger magnets and thinner bridges can be adopted to achieve a higher performance.

- The use of aluminium windings in place of copper can result in significant mass and cost savings. In terms of the performance, despite the higher Ohmic losses in aluminium, it may result in a more uniform loss distribution amongst the conductors, which may result in lower risk of hot spot formations, therefore, a higher motor reliability.

A comparison of the disclosed motor (HSFM) design and some leading state of the art ferrite and NdFeB designs have been summarized in Table 9-1. It can be noticed that, while

the proposed ferrite design may underperform a rare earth magnet based design, the cost savings in terms of £/kW can be as high as staggering 300%. Furthermore, the proposed ferrite motor design, significantly, outperforms other state of the art ferrite magnet based designs, in terms of both performance and cost savings, this being due to the more suitable balance of power and volume, as well as unique design features such as choice of a low cost rotor support component, Chapter 5.

In general and for the first time, this thesis report concludes that the traction motor designs based on ferrite magnets and aluminium windings can be a cheap and reliable substitute for conventional traction motors using rare-earth magnets and copper windings. On this basis, even though the latter approach may, still, result in superior designs in terms of power density (making this a preferred option for the end of the spectrum applications such as racing cars) the former may deliver, significantly, lower cost per *kW* suited to traction applications with moderate to high power density requirements, such as urban and road vehicles.

Table 9-1: Comparison of the Evoque-E HSFM design against the leading state of the art.

	GE Ferrite Motor [34]	Motor brain Ferrite Motor [35]	Nissan Leaf NdFeB Motor [38]	Evoque-E HSFM
Volume (including end winding; excluding housing)	8.6 l	6.9 l	8.5 l	9.5 l
Peak torque (10~30 secs)	190 Nm	170 Nm	280 Nm	245 Nm
Peak power	55 kW	55 kW	80 kW	106 kW
Continuous power	30 kW	30 kW	75 kW	60 kW
Torque Density	22.1 Nm/l	24.6 Nm/l	32.9 Nm/l	25.8 Nm/l
Peak power density	6.4 kW/l	8.0 kW/l	9.4 kW/l	11.2 kW/l
Continuous power density	3.5 kW/l	4.3 KW/l	8.8 kW/l	6.3 kW/l
Motor efficiency @ key operating points	> 95%	> 95%	> 95%	> 95%
Active Material Cost per peak kW	3.55 £/kW	2.59 £/kW	3.13 £/kW	1.01 £/kW
Max Speed	14 krpm	11 krpm	10.4 krpm	15 krpm
Magnet material	Ferrite	Ferrite	NdFeB	Ferrite
Winding material	Copper	Copper	Copper	Aluminium

Based on the theoretical findings and the prototype testing results, it is envisaged that the proposed low cost high power density ferrite traction motor may benefit from the following future work investigations:

1. The top speed requirement may result in reducing the rotor and magnet dimensions to cope with the associated centrifugal forces during high speed rotation. As a result, whilst in this thesis project the motor top speed was fixed and imposed by the top speed rating of the vehicle and the available gearbox ratio, it is envisaged that reducing and optimizing the rotor top speed with respect to the electromagnetic performance (particularly, the continuous torque and power density) may result in higher performing motors at the cost of some added material cost due to the increased rotor and magnet volume.

2. Due to the high speed operation, and high power density nature of the disclosed ferrite traction motor, a highly accelerated life test (HALT) is beneficial to assess the design reliability, in particular, with regards to the critical components such as windings, magnets and high speed bearings.

3. A sensitivity analysis of the design with respect to manufacturing anomalies, addressing effects such as rotor and stator shaft misalignment and eccentricity, should be performed.

4. As an ongoing work, and as a substitute to ferrite magnets, the exploitation of recycled NdFeB magnets is, currently, under investigation. On this basis, a joint project with Birmingham university is, currently, being pursued which addresses the use of recycled bonded and sintered magnets applying the hydrogenation disproportionation desorption recombination (HDDR) process, [121, 122]. Based on the studies in [122], the recycled bonded magnets may provide comparable performance as the ferrite magnets, and depending on the cost associated to their initial scrap material, they can be considered as both a technical and economical alternative to the primary rare earth magnets.

5. Based on the findings in Chapter 4, a detailed optimization of the large diameter to stack length ratio designs with weaker grade of magnets can be pursued. In this respect, a full comparative assessment of the demagnetization, power density and cost needs to be addressed.

6. Following the findings in Chapter 5, the construction and testing of a fir tree rotor support based on a work hardened low grade austenitic steel and using an approach alternative to solid piece segments, should be pursued as part of a future project.

7. The exploitation of the single piece rotor design, disclosed in chapter 5, in a medium speed range Hybrid Electric Vehicle (HEV) is the scope of an ongoing project. Within this project a more detailed cost comparison of this rotor solution against that of the fir tree option will be addressed.

References

[1] A. Izadian et al, ''Renewable Energy policies, A Brief Review of the Latest U.S. and E.U. Policies'', IEEE Industrial Elect Magazine, Sep 2013, pp 21-34

[2] C. C. CHAN, IEEE Power Electronics and Motion Control, IPEMC Conf, Vol.1, Aug 2004, pp 46 – 57

[3] A. E. Jones, M. Irwin, and A. Izadian, "Incentives for microgeneration development in the U.S. and Europe," in Proc. IEEE Industrial Electronics Conf., IECON, 2010, pp. 3018–3021.

[4] M. Felicianoa and D. C. Prosperib, "Planning for low carbon cities: Reflection on the case of Broward County, Florida, USA," 45th ISOCARP World Congress on low carbon cities Portugal, vol. 28, no. 6, Dec. 2011, pp. 505–516.

[5] J. Muth and E. Smith, "45% by 2030, towards a truly sustainable energy system in the EU," EREC Report, [Online], May 2011. Available: http://egec.info/wp-content/uploads/2011/03/45_2030_EREC_2011.pdf

[6] M. Zeraoulia et all,"Electric Motor Drive Selection Issues for HEV Propulsion Systems: A Comparative Study'', IEEE Trans. On. Vehicular. Tech., vol. 55, no. 6, Nov 2006.

[7] M. Barcaro, ''PM Motors for Hybrid Electric Vehicles'', The Open Fuels & Energy Science Journal, Vol. 2, 2009, pp 135-141

[8] T. Wang et al., "Design characteristics of the induction motor used for hybrid electric vehicle," IEEE Trans. Magn., vol. 41, no. 1, Jan. 2005, pp. 505–508.

[9] J. Malan et al., "Performance of a hybrid electric vehicle using reluctance synchronous machine technology," IEEE Trans. Ind. Appl., vol. 37, no. 5, Sep./Oct. 2001, pp. 1319–1324.

[10] K. M. Rahman et al., "Advantages of switched reluctance motor applications to EV and HEV: Design and control issues," IEEE Trans. Ind. Appl., vol. 36, no. 1, pp. 111–121, Jan./Feb. 2000.

[11] A. Emadi et al, ''Power Electronics and Motor Drives in Electric, Hybrid Electric, and Plug-In Hybrid Electric Vehicles'', IEEE Trans.Ind. Elecron., vol. 55, no. 6, June 2008, pp 2237-2245

[12] S. S.Williamson et al , "Comprehensive drive train efficiency analysis of hybrid electric and fuel cell vehicles based on motor controller efficiency modelling," IEEE Trans. Power Electron., vol. 21, no. 3, May 2006, pp. 730–740.

[13] G. Brusaglino et al., "Advanced drives for electrically propelled vehicles," in Proc. IEE Colloquium—Elect. Mach. Design All-Electric Hybrid-Elect. Veh., pp. 4/1–4/12.

[14] J. Chatzakis, K. Kalaitzakis, N. C. Voulgaris, and S. N. Manias, "Designing a new generalized battery management system," IEEE Trans. Ind. Electron., vol. 50, no. 5, Oct. 2003, pp. 990–999

[15] L. Chang, "Comparison of ac drives for electric vehicles—A report on expert's opinion survey," IEEE Aerosp. Electron. Syst. Mag., vol. 9, no. 8, Aug. 1994, pp. 7–11.

[16] T. Burress, ''Benchmarking of Competitive Technologies'', Oak Ridge National Laboratory, May 2011.

[17] S. A. Rogers, "c Motors Program," US department of energy report, Jan 2013. [Online], Available: http://energy.gov/sites/prod/files/2014/04/f15/2013_apeem_report.pdf

[18] J. D. Santiago et al, "Electrical Motor Drivelines in Commercial All Electric Vehicles: a Review'', IEEE Trans. Vehicular. Tech., 2012, pp 475-484

[19] R.M. Cuenca et al, ''Evaluation of Electric Vehicle Production and Operating Costs'', Centre for Transportation Research at Argonne National Laboratory, Nov 1999

[20] T. Murata et al, "Technologies to reduce heavy rare earth for NdFeB sintered magnet'', Magnetic Materials Research Lab, NEOMA at Hitachi Metals, 2012.

[21] D. Brown, ''The comparison of Anisotropic (and Isotropic) Powders for polymer Rare Earth Permanent Magnets'' , Magnequench Technology Centre, 2003, Available: www.molycorp.com/wp-content/uploads/REPM_Aniso.

[22] M. Sanada, Y. Inoue, and S. Morimoto, "Rotor Structure for Reducing Demagnetization of Magnet in a PMASynRM with Ferrite Permanent Magnet and its Characteristics'', IEEE ECCE, Sep 2011, pp 4189 – 4194

[23] M. Paradka, Boecker, J., "Design of a High Performance Ferrite Magnet Assisted Synchronous Reluctance Motor for an Electric Vehicle'', 38th Annual Conference on IEEE Indust Electro SocietyOct 2012, pp 4099 – 4103

[24] K. I. Laskaris, "Internal Permanent Magnet Motor Design for Electric Vehicle Drive'', IEEE TRANSACTIONS ON INDUS ELECTS, VOL. 57, NO. 1, JAN 2010, pp 138-145

[25] A. Malikopoulos, "Autonomous Intelligent Plug-In Hybrid Electric Vehicles (PHEVs)'', Oak Ridge National Laboratory, May 2012.

[26] R. Kisner et al, "Embedded Sensors and Controls to Improve Component Performance and Reliability Conceptual Design Report'', Oak Ridge National Lab, Sep 2012.

[27] S. Constantinides, "Rare Earth Materials, How scarce are they?'', Arnold Magnetic Technologies, 2010

[28] S. Chu. (2011, Dec). Critical Materials Strategy. US Department of Energy (DOE). [Online]. Available: http://energy.gov/

[29] A. Fasolo et al, "Performance Comparison between Switching-Flux and IPM Machine with Rare Earth and Ferrite PMs'', International Conference on Electrical Machines (ICEM), Sep 2012

[30] M. Kimiabeigi, "Stator arrangement and electrical generator'', EP 2685616 A1, Jul 2012

[31] N. Uzhegov, E. Kurvinen, J. Nerg, J. Pyrhönen, J. T. Sopanen, and S. Shirinskii, "Multidisciplinary Design Process of a 6-Slot 2-Pole High-Speed Permanent-Magnet Synchronous Machine," IEEE Trans. Ind. Elec., vol. 63, no. 2, pp. 784 - 795, Feb. 2016.

[32] J. S. Hsu, S. C. Nelson, and P. A. Jallouk. "Report on Toyota Prius Motor Thermal Management." Oak Ridge National Laboratory, 2005.

[33] F. Demmelmayr, B. Weiss, M. Troyer and M. Schroedl, "Comparison of PM-machines With Ferrite and NdFeB Magnets in Terms of Machine Performance and Sensorless Start-up Control'', IEEE International Conf on Indust Technology (ICIT), Feb 2013, pp 272 – 277

[34] J. Galioto, P. B. Reddy, A. M. EL-Refaie, "Effect of Magnet Types on Performance of High Speed Spoke Interior Permanent Magnet Machines Designed for Traction Applications," in Proc. Energy Conversion Congress and Exposition (ECCE), Sep 2014, pp. 4513 - 4522.

[35] Y. Burkhardt, A. Spagnolo, P. Lucas, et al., "Design and analysis of a highly integrated 9-phase drivetrain for EV applications," International Conference on Electrical Machines (ICEM), Sep 2014, pp. 450 – 456.

[36] T. A. Burress, S. L. Campbell, C. L. Coomer, et al., "Evaluation of the 2010 Toyota Prius Hybrid Synergy Drive System,'' Oak Ridge Nat. Lab., Oak Ridge, TN, USA, ORNL/TM-2010/253, Mar. 2011.

[37] R. H. Staunton, T.A. Burress, and L.D. Marlino, "Evaluation of 2005 Honda Accord Hybrid Electric Drive System,'', Oak Ridge Nat. Lab., Oak Ridge, TN, USA, ORNL/TM-2006/535, Sep. 2006.

[38] Y. Sato, S. Ishikawa, T. Okubo, M. Abe, and K. Tamai, "Development of high response motor and inverter system for the Nissan LEAF electric vehicle," presented at the SAE World Congr. Exhibit., 2011, Tech. Paper 2011-01-0350.

[39] G. Pellegrino, A. Vagati, P. Guglielmi, et al., "Performance comparison between Surface Mounted and Interior PM motor drives for Electric Vehicle application," IEEE Trans. Ind. Electron., vol 59, pp 803 – 811, Feb. 2012.

[40] S. Morimoto, S. Ooi, Y. Inoue, and M. Sanada, "Experimental Evaluation of a Rare-Earth-Free PMASynRM With Ferrite Magnets for Automotive Applications," IEEE Trans. Ind. Electron., vol. 61, no. 10, Oct. 2014.

[41] T. Jahns, "Flux-weakening regime operation of an interior permanent magnet synchronous motor drive, " IEEE Trans. Ind. Appl., vol. 23, no. 4, pp. 681-689, July. 1987.

[42] M. A. Rahman et al, "Advances on IPM Technology for Hybrid Electric Vehicles", IEEE, Vehicle Power and Propulsion Conference, 2009 (VPPC), Sep 2009, pp 92-97.

[43] Electric Motors 101: Understanding the Basics of Electric Motor Technology, pp 1-5. General Motors. [Online]. Available: www.gmgoelectric.com

[44] T. A. Burress, C. L. Coomer, S. L. Campbell, A. A. Wereszczak, J. P. Cunningham, L. D. Marlino, L. E. Seiber, and H. T. Lin, "Evaluation of the 2008 Lexus LS 600H Hybrid Synergy Drive System," Oak Ridge National Laboratories, Oak Ridge, TN, ORNL/TM-2008/185.

[45] Electrical drive motor for a vehicle, by J. Merwerth, J.Halbedel, and G. Schlangen. (2012, Oct). Patent US 2012/0267977.

[46] A.M. EL-Refaie, J. P. Alexander, S. Galioto, et al., "Advanced High Power-Density Interior Permanent Magnet Motor for Traction Applications", IEEE Trans. Ind. Appl., vol. 50, no. 5, pp. 3235-3248, Sep/ Oct. 2014.

[47] J. S. Hsu, C. W. Ayers, and C. L. Coomer, "Report on Toyota Prius Motor Design and Manufacturing Assessment", Oak Ridge National Laboratory, 2004.

[48] R. H. Staunton, C. W. Ayers, J. N. Chiasson, B. A. Burress, and L. D. Marlino, "Evaluation of 2004 Toyota Prius hybrid electric drive system," Oak Ridge Nat. Lab., Oak Ridge, TN, Tech. Rep. ORNL/TM- 2006/423, 2006.

[49] R. Kaczmarek, "Simulating the Toyota Prius Electric Motor'', Cobham Technical Services – Vector Fields Software, Mar 2013.

[50] "Technical Insights on Remy's Off-the-Shelf Hybrid Motor Solutions,'' Remi international: Inside the HVH™ Hybrid Motor, Oct 2009.

[51] Humphries, "M. Rare earth elements: The global supply chain," CRS Report for Congress,R41347 (Congressional Research Service, Library of Congress, 2010).

[52] I. Boldea, L. N. Tutelea, L. Parsa, and D. Dorrell, "Automotive electric propulsion systems with reduced or no permanent magnets: An overview," IEEE Trans. Ind. Electron., vol. 61, no. 10, pp. 5696–5711, Oct. 2014.

[53] S. Eriksson et al, "Alternative permanent magnet materials for renewable energy applications - the possibility of substituting NdFeB with Ferrites", Uppsala Univ., 2011.

[54] R. Vartanian et al, "Performance Analysis of a Rare Earth Magnet Based NEMA Frame PMa-SynRM with Different Magnet Type and Quantity'', IEEE, Electric Machines & Drives Conference (IEMDC), May 2013, pp 476 – 483.

[55] H. Cai, B. Guan, and L. Xu, "Low-cost ferrite PM-assisted synchronous reluctance machine for electric vehicles," IEEE Trans. Ind. Electron., vol. 61, no.10, pp.5741-5748, Oct. 2014.

[56] H. J. Kim, D. Y. Kim, and J. P. Hong, "Structure of Concentrated-Flux-Type Interior Permanent-Magnet Synchronous Motors Using Ferrite Permanent Magnets," IEEE Trans. Magn., vol. 50, no. 11, pp.113-122, Nov 2014, Art. ID 8206704.

[57] S. I. Kim, J. Cho, S. Park, T. Park, and S. Lim, "Characteristics comparison of a conventional and modified spoke-type ferrite magnet motor for traction drives of low-speed electric vehicles," IEEE Trans. Ind. Appl., vol. 49, no. 6, pp. 2516-2523, Dec. 2013.

[58] W. Fei, W. Liang, and P. C. K. Luk, "Influence of magnet layer number on electromagnetic performance of ferrite interior permanent magnet synchronous machine", International Conference on Electrical Machines and Systems (ICEMS), Oct 2014, pp. 1 – 7.

[59] "Permanent Magnet Rotor for High Speed Motors and Generators," by Carl J. Heyne, Granted on May 1986, US4588914 A, Available: http://www.google.com.ar/patents/US4588914.

[60] M . M. Rahman, K. T. Kim, and J. Hur, "Design and Analychisis of Neodymium Free SPOKE-type Motor with Segmented Wing Shape Permanent-Magnet for concentrating flux density," Energy Conversion Congress and Exposition (ECCE), Sep 2013, pp. 4991-4997.

[61] Y. Deshpande and A Toliyat,"Design of an Outer Rotor Ferrite Assisted Synchronous Reluctance machine (Fa-SynRM) for Electric Two Wheeler Application," IEEE Energy Conversion Congress and Exposition (ECCE), Sep. 2014, pp. 3147 - 3154.

[62] W. Zhao, T. A. Lipo, and B. I. Kwon, "Comparative Study on Novel Dual Stator Radial Flux and Axial Flux Permanent Magnet Motors With Ferrite Magnets for Traction Application," IEEE Trans. Magn., vol. 50, no. 11, pp. 1–4, Nov. 2014.

[63] K. Chiba, S. Chino, M. Takemoto, and S. Ogasawara, "Fundamental analysis for a ferrite permanent magnet axial gap motor with coreless rotor structure," in Electrical Machines and Systems (ICEMS), 2012 15th International Conference on, Oct., pp. 1–6.

[64] "Ferrite magnets, FB series", TDK magnetics, [Online], Available: https://product.tdk.com/info/en/products/magnet/index.html June 2011.

[65] M. Fasil, N. Mijatovic, B. B. Jensen, and J. Holboll, "Performance variation of ferrite magnet PMBLDC motor with temperature," IEEE Trans. on Magn., Vol. 51, No. 12, Dec 2015.

[66] D. G. Dorrell, M. F. Hsieh, and A. M. Knight, "Alternative rotor designs for high performance brushless permanent magnet machines for hybrid electric vehicles," IEEE Trans. Magn., vol. 48, no. 2, pp. 835–838, Feb. 2012.

[67] I. Petrov, M. Polikarpova, and J. Pyrhonen, "Rotor surface ferrite magnet synchronous machine for generator use in a hybrid application: electromagnetic and thermal analysis," in Industrial Electronics Society, IECON 2013 - 39th Annual Conference of the IEEE, Nov 2013, pp. 3090–3095.

[68] A. Sarikhani, and O. A. Mohammed, "Demagnetization Control for Reliable Flux Weakening Control in PM Synchronous Machine," IEEE Trans. Energy. Convers., vol. 27, no. 4, pp. 1046-1055, Dec. 2012.

[69] B. A. Welchko, T. M. Jahns, W. L. Soong, and J. M. Nagashima, "IPM Synchronous Machine Drive Response to Symmetrical and Asymmetrical Short Circuit Faults, " IEEE Trans. Energy. Convers., vol. 18, no. 2, pp. 291-298, June. 2003.

[70] J. A. Farooq, A. Djerdir, and A. Miraoui, "Analytical Modeling Approach to Detect Magnet Defects in Permanent-Magnet Brushless Motors," IEEE Trans. Magn., vol. 44, no. 12, pp.4599–4604, Dec. 2008.

[71] K. C. Kim, K. Kim, H. J. Kim, and J. Lee, "Demagnetization analysis of permanent magnets according to rotor types of interior permanent magnet synchronous motor," IEEE Trans. Magn., vol. 45, no. 6, pp. 2799–2802, Jun. 2009.

[72] Li, Y. Li, and B. Sarlioglu, "Partial irreversible demagnetization assessment of flux-switching permanent magnet machine using ferrite permanent magnet material" IEEE Trans. Magn., vol. 51, no. 7, pp. 1–9, July. 2015.

[73] B. N. Cassimere, S. D. Sudhoff, and D. H. Sudhoff, "Analytical Design Model for Surface-Mounted Permanent-Magnet Synchronous Machines," IEEE Trans. Energy. Convers., vol. 24, no. 2, pp. 347-357, June. 2009.

[74] J. J. Potgieter, and M. J. Kamper, "Calculation Methods and Effects of End-Winding Inductance and Permanent-Magnet End Flux on Performance Prediction of Nonoverlap Winding Permanent-Magnet Machines," IEEE Trans. Ind. Appl., vol. 50, no. 4, pp. 2458-2466, July/Aug. 2014.

[75] A. Youmssi, "A three-dimensional semi-analytical study of the magnetic field excitation in a radial surface permanent-magnet synchronous motor," IEEE Trans. Magn., vol. 42, no. 12, pp. 3832–3841, Dec. 2006.

[76] Z. Q. Zhu, Y. Pang, D. Howe, *et al.*,"Analysis of Electromagnetic Performance of Flux-Switching Permanent-Magnet Machines by Nonlinear Adaptive Lumped Parameter Magnetic Circuit Model," IEEE Trans. Magn., vol. 41, no. 11, pp. 4277–4287, Nov. 2005.

[77] J. Pyrhönen, V. Ruuskanen, J. Nerg, J. Puranen, and H. Jussila, "Permanent-Magnet Length Effects in AC Machines," IEEE Trans. Magn., vol. 46, no. 10, pp.3783–3789, Oct. 2010

[78] H. D. Swardt, "Critical Speed on an electric motor explained'', Marthinusen & Coutts, Mar 2007, [Online], www.mandc.co.za/pdfs/Critical_Speed.pdf.

[79] C. W. Ayers, "Electric motor Architecture R&D'', Oak Ridge National Laboratory, DOE Hydrogen and Fuel Cells Program and Vehicle Technologies Program Annual Merit Review and Peer Evaluation Meeting, 2013.

[80] E. Lovelace, T. Jahns, T. Keim, and J. Lang, "Mechanical design considerations for conventionally laminated, high-speed, interior PM synchronous machine rotors," IEEE Trans. Ind. Appl., vol. 40, no. 3, pp. 806–812, May/Jun. 2004.

[81] Y. Gao, R. Long, Y. Pang, and M. Lindenmo, "Fatigue properties of an electrical steel and design of EV/HEV IPM motor rotors for durability and efficiency," presented at the SAE, Tech. Paper 2010-01-1308.

115

[82] L. Cunningham, "Beryllium Recycling in the United States in 2000,"
U.S. Department of the Interior, U.S. Geological Survey (USGS), pp. 6–13, 2004, Available: http://pubs.usgs.gov/circ/c1196p/c1196p.pdf

[83] S. Jewell and S. M. Kimball, "Mineral commodity summaries," U.S. Department of the Interior, U.S. Geological Survey (USGS), 196 p., 2015, Available: http://dx.doi.org/10.3133/70140094

[84] A. Darby and D. Fishwick, "A review of the health effects and the evidence for screening or surveillance in workers exposed to beryllium," Health and Safety Laboratory, Health and Safety Executive (HSE), 2011, Available:
http://www.hse.gov.uk/research/rrpdf/rr873.pdf

[85] T.P. Taylor, M. Ding, D.S. Ehler, T.M. Foreman, J.P. Kaszuba, N.N. Sauer, "Beryllium in the environment: a review", Journal of Environmental Science and Health , pp. 439–469, 2003.

[86] B. Boazzo, A. Vagati, G. Pellegrino, E. Armando, and P. Guglielmi, "Multipolar Ferrite-Assisted Synchronous Reluctance Machines: A general design approach," IEEE Trans. Ind. Electron., vol. 62, no. 2, pp. 832-845, Feb. 2015.

[87] A.M. EL-Refaie, "Fractional-Slot Concentrated Windings Synchronous Permanent Magnet Machines: Opportunities and Challenges," IEEE Trans. Ind. Electron., vol. 57, no. 1, pp. 107–121, Jan. 2010.

[88] J. Widmer, R. Martin, B. Mecrow, "Pre-compressed and stranded aluminum motor windings for traction motors", IEEE Trans. Ind. Appl, Feb 2016.

[89] F. Magnussen and H. Lendenmann, "Parasitic effects in PM machines with concentrated windings," IEEE Trans. Ind. Appl., vol. 43, no. 5, pp. 1223–1232, Sep./Oct. 2007.

[90] O. Bottauscio, G. Pellegrino, P. Guglielmi, M. Chiampi, and A. Vagati "Rotor loss estimation in permanent magnet machines with concentrated windings," IEEE Trans. Magn, vol. 41, no. 10, pp. 3913-3915, Oct. 2005.

[91] Y.Honda, T.Nakamura, T.Higaki, Y.Takeda, "Motor design considerations and test results of an interior permanent magnet synchronous motor for electric vehicles", hirty-second IAS Annual Meeting, 1997,Vol. 1, pp.75-82.

[92] 1. 1. Lee, W. H. Kim, 1. S. Yu, S. Y. Yun, S. M. Kim, and 1. Lee, "Comparison between concentrated and distributed winding in IPMSM for traction application," the international conference on electrical machines and systems (ICEMS), 2010, pp. 1172-1174.

[93] L. Chong , R. Dutta, N. Q. Dai, M. F. Rahman, H. Lovatt, "Comparison of Concentrated and Distributed Windings in an IPM Machine for Field Weakening Applications," Australasian universities Power Engineering Conference (AUPEC), Dec 2010, pp 1-5.

[94] S.-O. Kwon, S.-I. Kim, P. Zhang, and J.-P. Hong, "Performance comparison of IPMSM with distributed and concentrated windings," in 41st Conf. Rec. IEEE IAS Annu. Meeting, Oct. 8–12, 2006, vol. 4, pp. 1984–1988.

[95] H. Hamalainen, J. Pyrhonen, and J. Nerg, "AC Resistance factor in one layer form-wound winding used in rotating electrical machines," IEEE Trans. Magn., vol. 49, no. 6, pp. 2967–2973, Jun. 2013.

[96] M. Popescu and D. G. Dorrell, "Proximity losses in the windings of high speed brushless permanent magnet AC motors with single tooth windings and parallel paths," IEEE Trans. Magn., vol. 49, no. 7, pp. 3913–3916, Jul. 2013.

[97] P. B. Reddy, T. M. Jahns, and T. P. Bohn, "Transposition effects on bundle proximity losses in high-speed PM machines," in IEEE Energy Conversion Congress and Exposition (ECCE2009), 2009, pp.1919–1926.

[98] S. Iwasaki, R. Deodhar, Y. Liu, A. Pride, Z.Q. Zhu, and J. Bremner, "Influence of PWM on the proximity loss in permanent magnet brushless AC machines," IEEE Trans. Industry Applications, vol.45, no.4, pp.1359-1367, 2009.

[99] P. Mellor, R. Wrobel, and N. Simpson, "AC losses in high frequency electrical machine windings formed from large section conductors," in Proc. IEEE Energy Convers. Congr. Expo. (ECCE), 2014, pp. 5563–5570.

[100] J.S. Hsu, H.P. Liou, B.T. Lin, W.F. Weldon, "losses influenced by third-harmonic flux in induction motors," vol. 6, no. 3, pp. 461- 468, Sep 1991.

[101] M. M. Swamy, T. Kume, A. Maemura, and S. Morimoto, "Extended high speed operation via electronic winding change method for AC motors," IEEE Trans. Ind. Appl., vol. 42, no. 3, pp. 742–752, May/Jun. 2006.

[102] S. Sadeghi, L. Guo, H. Toliyat, and L. Parsa, "Wide operational speed range of five-phase permanent magnet machines by using different stator winding configurations," IEEE Trans. Ind. Electron., vol. 59, no. 6, pp. 2621–2631, Jun. 2012.

[103] C. R. Sullivan, "Aluminium winding and other strategies for high-frequency magnetics design in an era of high copper and energy costs", IEEE Trans. Power Electron, vol. 23, no. 4, July 2008.

[104] J. D. Widmer, "Segmental rotor switched reluctance machines for use in automotive traction", PhD Thesis, 2014.

[105] Cogent power, https://cogent-power.com/cms-data/downloads/m270-35a_1.pdf, [Online]

[106] Zytek Automotive (Continental Engineering), http://www.zytekautomotive.co.uk/products/electric-engines/170kW/, [Online]

[107] University of Newcastle, Centre for Advanced Drives, http://www.ncl.ac.uk/eee/industry/caed/.

[108] Range Rover Evoque-E, file://campus/home/home33/nmk62/Downloads/Evoque%20Brochure-min%20(1).pdf, [Online]

[109] K. Mumtaz, S. Takahashi, J. Echigoya, et al, "Magnetic measurements of martensitic transformation in austenitic stainless steel after room temperature rolling," Journal of Materials Science, Vol. 39, 2004, pp. 85– 97.

[110] C. B. Post and W. S. Eberly, "Stability of Austenite in Stainless Steel," Trans. American. Society. Metals., vol. 39, pp. 868- 890, 1947.

[111] The Hendrix group, [Online], Available: http://hghouston.com/resources/material-property-data/stainless-steel-data/cold-working-properties.aspx.

[112] Carpenters stainless steel blue book, Selection Alloy Data Fabrication, 2012, page 21, [Online], Available: http://www.cartech.com/techarticles.aspx?id=1476.

[113] P. H. Mellor, R. Wrobel, and D. Holliday, "A computationally efficient iron loss model for brushless ac machines that caters for rated flux and field weakened operation. In Proc. IEEE Int. Electric Machines and Drives Conf. IEMDC '09, pages 490–494, 2009.

[114] J. Goss, P. H. Mellor, R. Wrobel, D. A. Staton, and M. Popescu, "The design of AC permanent magnet motors for electric vehicles: a computationally efficient model of the operational envelope," in 6th IET International Conference on Power Electronics, Machines and Drives (PEMD 2012), 2012, pp. B21–B21.

[115] Shanghai metals market, [online], Available: http://www.metal.com/metals/productinfo/201102250135

[116] MetalPrices.com, [online], Available: http://www.metalprices.com/metal/stainless-steel/stainless-steel-flat-rolled-coil-316

[117]AKSteel,[Online],Available:http://www.aksteel.com/pdf/markets_products/stainless/Stainless_Steel_Price_Book_20140902.pdf

[118] T. Sun, S.-O. Kwon, S.-H. Lee, and J.-P. Hong, "Investigation and comparison of inductance calculation methods in interior permanent magnet synchronous motors," in International Conference on Electrical Machines and Systems (ICEMS), 2008, pp. 3131–3136.

[119] London exchange market. [Online], Available: https://www.lme.com

[120] M. Olszewski, "FY2011 Oak Ridge National Laboratory annual progress report for the power electronics and electric machinery program," Oak Ridge Nat. Lab., Oak Ridge, TN, ORNL/TM-2005/264, Oct 2011.

[121] R.S. Sheridan, "Optimization of HDDR processing parameters of sintered NdFeB magnets," PhD thesis, University of Birmingham, Sep 2013.

[122] M. Kimiabeigi, J. Widmer, R.S. Sheridan, R. Harris, A. Walton "Design of high performance traction motors using cheaper grade of materials", IET International Conference on Power Electronics, Machines and Drives (PEMD), April 2016.

[123] Browne, Philip A. "Topology Optimization of Linear Elastic Structures." PhD Thesis. University of Bath, 2013, Available: http://www.met.reading.ac.uk/~vb904302/browne_phd.pdf.

[124] M.P. Bendsoe and O. Sigmund. Topology Optimization: Theory, Methods, and Applications, Springer, 2003.

[125] E. Lee, K.A. James, J.R.R.A. Martins, "Stress-constrained topology optimization with design-dependent loading," Struct Multidiscip Optim., 46 (2012), pp. 647–661, doi:10.1007/s00158-012-0780-x.

Appendix I

The variation of the flux density by shortening the stack length in Figures 4-4 and 4-5 can be explained based on (i), (ii), and (iii), where the $R_{lamination}$ and $R_{end,leak}$ are the magnetic reluctance associated with the stator laminations stack and the end windings, respectively, φ and φ_{end} are the flux originated from the winding parts associated with the stack length and the end winding, respectively, Figure I(a), and A_0 is the flux path surface area associated with the stack length, l_z, Figure I(a). By shortening the stack length, and during non-saturated conditions, the $R_{lamination}$ and φ vary with a rate, which is equal or, as will be identified below, greater than the rate of the A_0 variation. As a result, the increase of the flux density in Figures 4-4(a) and 4-5(a), may be attributed to the end winding flux flowing in the end regions of the laminations stack, φ_{end}, whose value is rather fixed and independent from the stack length variation, (iii). An illustration of the φ and φ_{end} and the end stack region which is commonly engaged by the two, indicated as $l_{z,end}$, is given in Figure I(a). During saturated conditions, the unchanged values of the flux density against stack length variation, suggests that either $R_{lamination}$ and φ vary with a greater proportion compared to the non-saturated conditions or φ_{end}, unlike the non-saturated conditions, is not fixed and decreases with shortening of the stack length.

Due to the linear and non-saturated conditions of the laminations material (in case of the low demagnetizing currents), and to improve the lumped circuit modelling in Chapter 4.3.2, the φ and φ_{end} , in Figure I(a), can be separated assuming each one occupies a distinct fraction of the laminations stack volume, as illustrated in Figure I(b), where $0 < \beta < 1$. As a result of this modelling, it can be realized that the $R_{lamination}$ experiences a smaller effective surface area than A_0 , and may be, more accurately, expressed as (iv). Following the explanation above and based on (iv), it can be realized that during non-saturated conditions, the $R_{lamination-modified}$ changes with a greater rate than the stack length variation.

<div align="center">(a)</div> <div align="center">(b)</div>
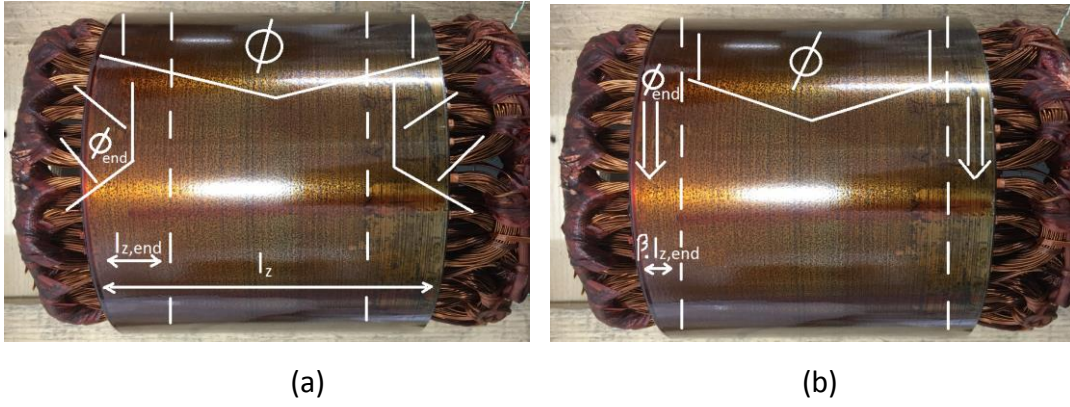
Figure I: Illustration of the reduced effective surface area for the demagnetizing field/ flux. (a) Actual model. (b) Equivalent model.

$$\varphi = 2Ni/R_{lamination} \qquad \text{(i)}$$

$$\varphi_{end} = 2Ni/R_{end,leak} \qquad \text{(ii)}$$

$$B = (\varphi + \varphi_{end})/A_0 \qquad \text{(iii)}$$

$$R_{lamination-modified} \propto 1/\left(l_z - \beta . l_{z,end}\right) \qquad \text{(iv)}$$

Appendix II

Decomposing the axial flux, due to the end windings effect, by implementing the equivalent model explained in Figure I(b), it can be realized that the flux associated with the stack length, φ, travels a radial path through the stator teeth and a circumferential path through the stator yoke region, as illustrated in Figure II (a 39 mm against a 2 x 39 m stack have been compared). Please note that in Figure II, φ, only, corresponds to the demagnetization flux (field is a better term to use, but flux is more illustrative), and the leakage flux which does not link the rotor magnets, and only contributes to the magnetic saturation in the $r - \emptyset$ plane (i.e. the plane perpendicular to the axis of rotation) has not been included.

From the illustration in Figure II, it can be realized that changing the stack length does not affect the length of the demagnetization flux path (illustrated as l1+l2+l3 in Figure II), whereas the cross section perpendicular to the flux path (illustrated as A_t for the cross section in the tooth, and A_y for the cross section in the yoke) changes linearly with the stack length variation. On this basis, and from (4.1), it is clear that the reluctance associated with the stator laminations, $R_{lamination}$ has a direct and reverse proportion to the stack length variation.
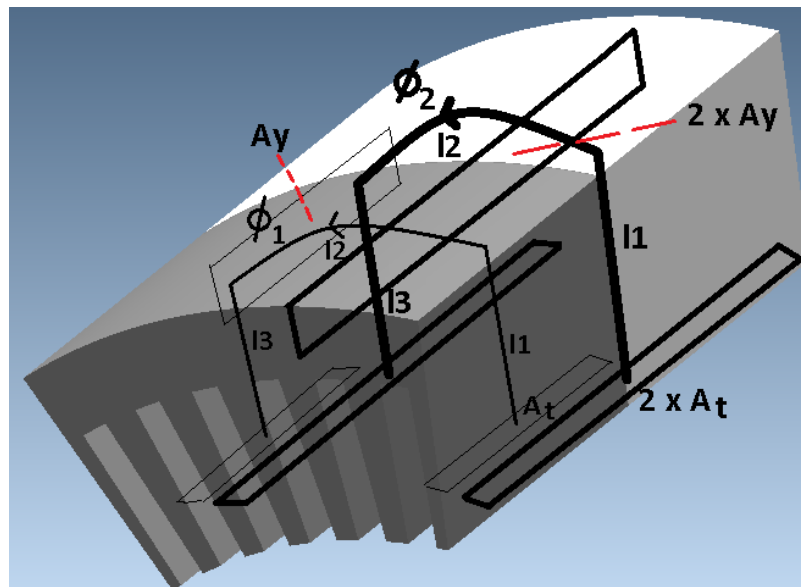

Figure II Illustration of the variation of stator laminations reluctance by varying (halving) the stack length.

Appendix III

To demonstrate the feasibility of a high power design using extra weak ferrite magnets (ceramic 8), a first principle design was made by, simply, scaling the dimeter and length of the original design. To assess the effect of shortening the length and decompose it from other parameters such as pole number, etc, same pole number, as well as electric and magnetic loading was maintained during the scaling. The design outcome is shown in Figure III(a), where the demagnetization capability under a 240% I_{pk} fault, and for two different stack lengths, has been simulated following a similar 3D FE set up in Chapter 4-3-1. As shown in Figures III(b) and (c), the design with short stack length demonstrates a, significantly, stronger demagnetization withstand capability, making the use of the extra weak ferrite magnets feasible for a demanding high power density application. Based on a basic comparison of the performance and cost of the high power ceramic 8 design and the FB9B ferrite design, Table I, it can be realized that following a simple size scaling, a reduction of magnet cost using an extra cheap grade magnet is feasible, but the cost advantage is partially negated due to the additional winding mass, as the length of the end windings was kept unchanged during the scaling. Finally, with regards to the exploitation of cheaper grade magnet materials the following comments should be noted:

a) While in the present analysis, the comparisons are, only, made between two different grades of ferrite magnets, the same principles are applicable and should be practiced for NdFeB grades with high and low contents of Dy. It is expected that due to the much higher price range of the NdFeB grades, the suitability of the concept in terms of reducing the demagnetization risk, and therefore enabling the, significantly, cheaper designs using low content dysprosium magnets will become more evident.

b) Based on the provided studies, reducing the stack length for a motor with distributed winding design is proved to be an effective parameter, which together with other approaches such as maximizing the number of poles, magnet burial in the rotor core, etc can contribute to enhancing the demagnetization performance of the weak and extra weak NdFeB or ferrite grade magnets, enabling such cheap material being used for low cost but high performance traction motor applications. The degree of merit of this exploitability might differ depending on the application and requirements. However, based on the information and guidelines provided, the designers may assess and, depending on the level of merit, utilize the concept for their specific design targets.

c) Finally, it should be noted that following the proposed approach, the substantial values of the end winding inductance may impose additional voltage, as well as reduction of the efficiency, both of which need to be considered as trade off factors during the design phase.
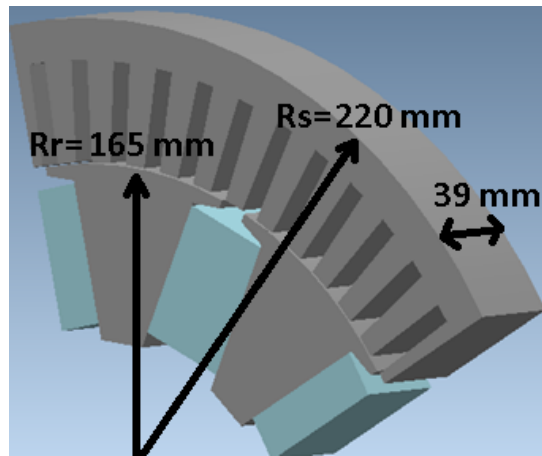
(a)
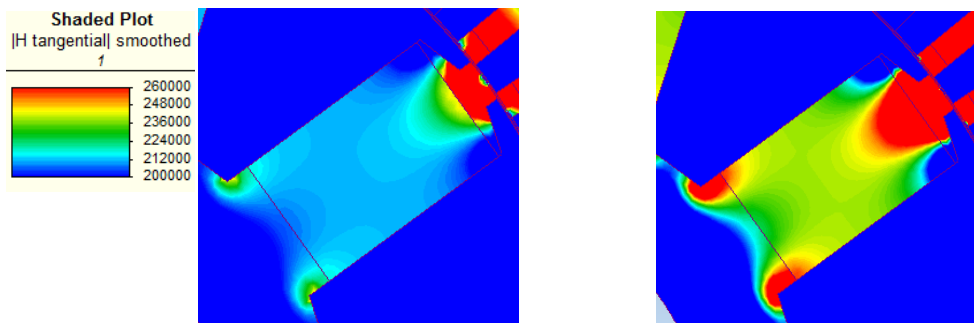
(b)   (c)

Figure III 80 kW first principle design using ceramic 8 magnets, and scaled diameter.

(a) Topology and geometry. (b) Demagnetization field for design with 39 mm stack, 240% $I_{pk.}$

(c) Demagnetization field for design with 2 x 39 mm stack, 240% $I_{pk.}$

TABLE I

First principle performance and cost assessment of the EV motor design using Ceramic 8 ferrite magnets.

|	FB9B magnets	Ceramic 8 magnets
Peak torque-Peak power	260 Nm-~80 kW	260 Nm-~80 kW
Motor volume (per unit)	1	1
Active material mass (per unit)	1	1.2
Magnets mass (kg)	4	4
Magnets cost (per unit)	1	0.7

Appendix IV

The efficiency map of the designs with 195 mm and 39 mm stack length, and FB9B magnets have been calculated using FE 2D, and accounting, only, for the winding (only DC loss) and iron loss parts, and shown in Figure IV. The 3D effect of stack length has been taken into account by including the end windings resistance and inductance, as well as reducing the available DC link voltage by the same factor as the stack length change, i.e. 5. From Figure IV, it is realized that by shortening the stack length the efficiency has dropped by about 1% in the key operating points (i.e. the points at which the vehicle runs most frequently) and more significantly in the high torque-low speed regions; the efficiency fall is, majorly, due to the increase of the per unit end winding resistance in the case of design with shorter stack length. Furthermore, based on Figure IV, by shortening the stack length the base speed of the design (thereby the power density) is reduced, this being, majorly, due to the larger per unit end winding inductance for a fixed available per unit DC link voltage.

Following a similar procedure, the effect of reducing the stack length on power factor was investigated in FE 2D and by including the end winding resistance and inductance. Based on the results, the influence of the stack length was realized to be negligible throughout the operating range.

Finally, it should be noted that as the shortening of the motor stack length (to improve demagnetization performance) may be followed by increasing the motor diameter (to enhance the torque and power output), a re-optimization of the motor design with respect to power density, efficiency, and power factor might become necessary, which is outside the scope of this work.
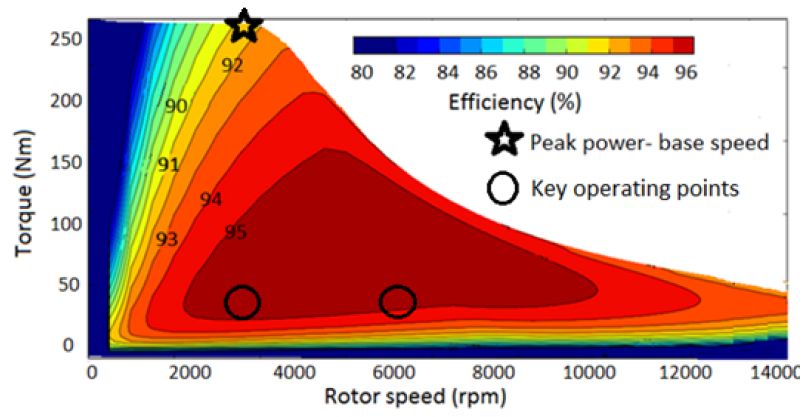
(a)
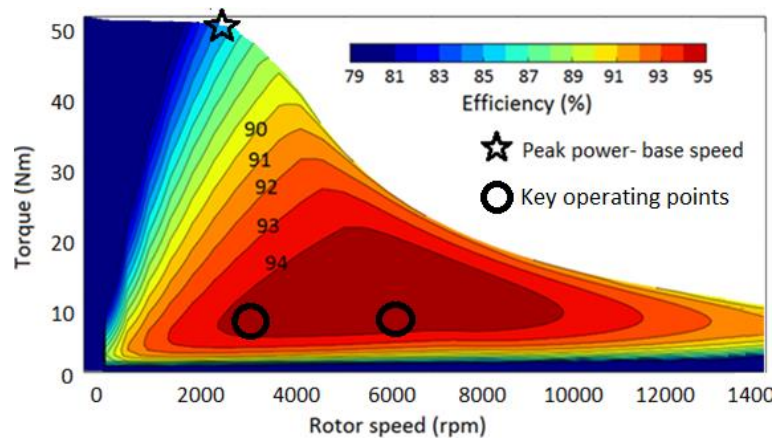
(b)

Figure IV Comparison of peak torque-speed performance and efficiency map for FB9B ferrite designs with different stack lengths. (a) 195 mm stack length. (b) 39 mm stack length.

Appendix V

It can be shown that for a balanced 3-phase system, with sinusoidal distribution of MMF in time and space, the 3-phase MMF is 1.5 times that of the associated 1-phase MMF. Using FE, and by taking the effects from the additional harmonics into account, it is realized that, for the present motor design with 2 slots per pole and phase and the given particular stator and rotor topology, the static torque and demagnetization performance of the 3-phase system can be approximated by a 1-phase system with 1.25 times the actual 3-phase current, Figures V and VI, and (v).

$$I_{pk-1\,phase} \approx 1.25 \cdot I_{pk-3\,phase} \qquad\qquad\qquad (v)$$

Based on the aforementioned transformation of 3-phase to 1-phase system, (v), and to simplify the prototype manufacturing, the full 3-phase overlapping windings have been reduced to only two non-overlapping coils belonging to one of the phases. As a result, to match the theoretical analysis to the prototype test set up, while obtaining an equivalent 3-phase system performance, throughout the analyses in Chapter 4 the I_{pk} refers to $I_{pk-1\,phase}$, (v).


(a)   (b)

(c)   (d)
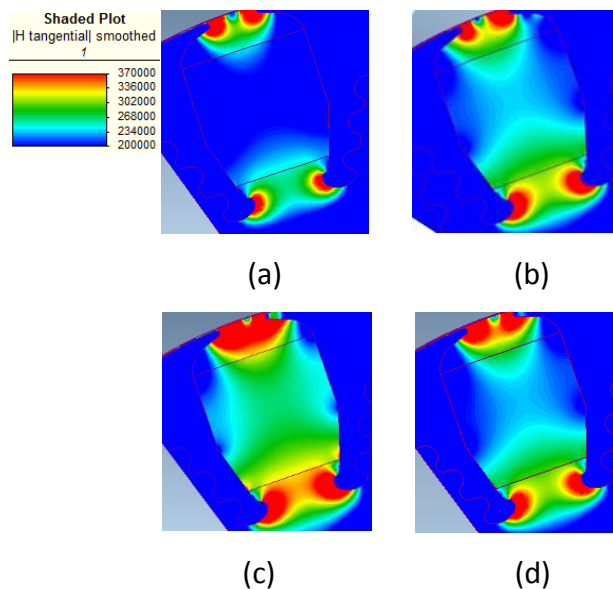
Figure V Comparison of the demagnetization behaviour under 1-phase and 3-phase system excitations, FE 2D, FB9B magnets. (a) 100% I_{pk} in 1-phase system. (b) 100% I_{pk} in 3- phase, $I_b=I_c$=-0.5 I_a. (c) 150% I_{pk} in 1-phase system. (d) 125% I_{pk} in 1-phase system.
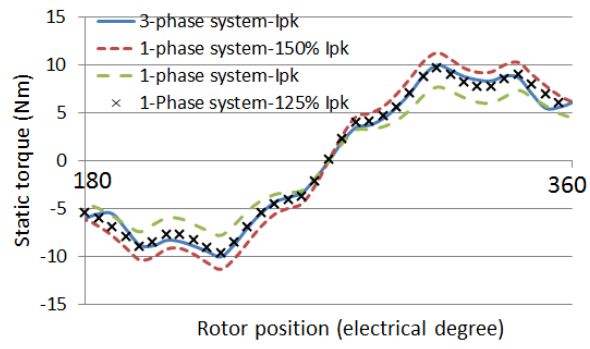
Figure VI Comparison of the static torque under 1-phase and 3-phase system excitations

Appendix VI

To optimize the single piece rotor structural design, a topology optimization technique based on a Solid Isotropic Material with Penalization (SIMP) method, [123, 124], has been applied. This technique is, widely, used in areas such as civil and structural engineering, and is based on an allocation of structural parameters (such as stiffness and mass) to each finite element domain, which are then governed by optimization functions, including the objectives and the constraints.

A practical approach to implement a topology optimization is the so called stress constrained mass minimization method, based on which the mass of the structure, i.e. rotor, is minimized such that the stress in any finite element domain does not exceed the yield stress of the corresponding material, [125]. On this basis, the objective function is defined as (vi), and it is constrained by the Hooke's law (vii.i). In (vii.i) the stress, σ_i, and strain, x, are related by the stiffness matrix, K, which itself is a function of the mass density, ρ, the Young's modulus, E_0, and the Poisson's ratio, ϑ, associated with each finite element domain, (vii.ii). Furthermore, assuming isotropic laminations, the stress, σ_i, can be represented by the Von Mises stress, as defined in (vii.iii), while x, y, z represent the Cartesian dimensions .

$$\text{Minimize } m(\rho) = \sum_1^N \rho_i, \quad \rho_i < 1 \tag{vi}$$
$$\text{Constraint: } f = K.x, \quad f(\sigma_i) < \sigma_{yield} \tag{vii.i}$$
$$K(\rho, E_0, \vartheta) = \sum_{i=1}^N \rho_i . k_i(E_0, \vartheta) \tag{vii.ii}$$
$$\sigma_i = \sqrt{\left\{\left(\sigma_x - \sigma_y\right)^2 + (\sigma_x - \sigma_z)^2 + \left(\sigma_y - \sigma_z\right)^2\right\}/2} \tag{vii.iii}$$

A solution from the rotor topology optimization, further constrained by the electromagnetically defined generic patterns in Section III.A, has been provided in Figure VII, where a sample of the finite element network and the local structural parameters has been illustrated.
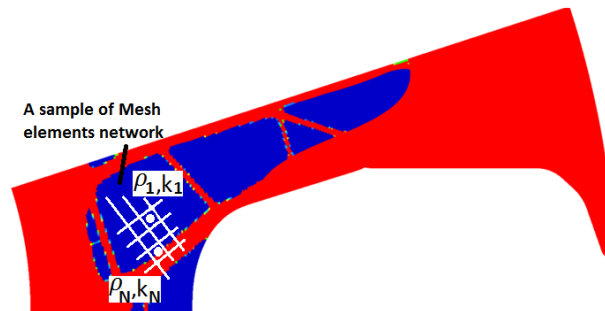

Figure VII Illustration of the stress-constrained mass minimization technique, employed for optimizing the single piece rotor design topology.